

AD-A113 807

OREGON GRADUATE CENTER BEAVERTON

F/6 20/2

RARE EARTH BORIDE ELECTRON EMITTER MATERIALS FABRICATION AND EV--ETC(U)

MAR 82 L W SWANSON, P R DAVIS, M A GESLEY

F19628-80-C-0117

UNCLASSIFIED

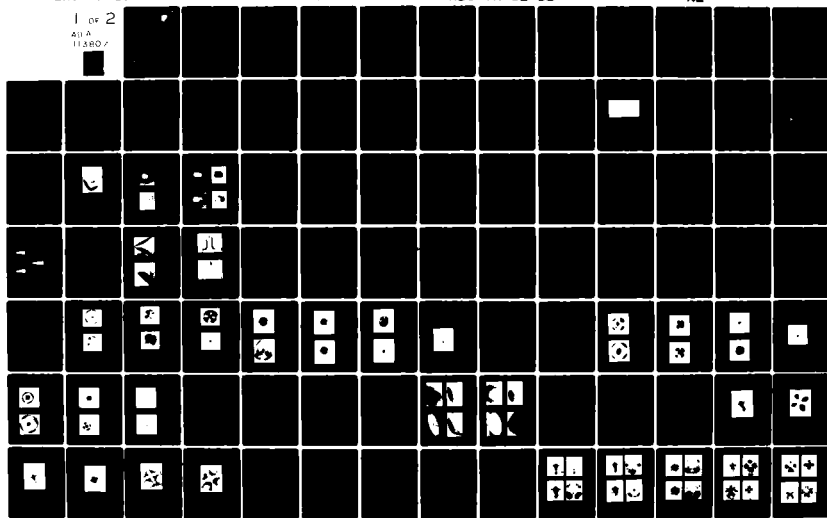
RADC-TR-82-12

NL

1 of 2

AD A

113807



12

RADC-TR-82-12
Final Technical Report
March 1982



RARE EARTH BORIDE ELECTRON EMITTER MATERIALS FABRICATION AND EVALUATION

Oregon Graduate Center

Lynwood W. Swanson
Paul R. Davis
Mark A. Gesley

AD A113807

APPROVED FOR PUBLIC RELEASE; DISTRIBUTION UNLIMITED

DTIC FILE COPY

ROME AIR DEVELOPMENT CENTER
Air Force Systems Command
Griffiss Air Force Base, New York 13441

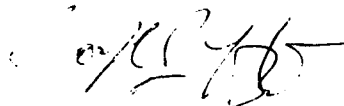
DTIC
ELECTE
S APR 26 1982 D
E

82 04 26 006

This report has been reviewed by the RADC Public Affairs Office (PA) and is releasable to the National Technical Information Service (NTIS). At NTIS it will be releasable to the general public, including foreign nations.

RADC-TR-82-12 has been reviewed and is approved for publication.

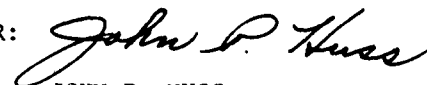
APPROVED:


JOSEPH J. HUTTA
Project Engineer

APPROVED:


HAROLD ROTH
Director, Solid State Sciences Division

FOR THE COMMANDER:


JOHN P. HUSS
Acting Chief, Plans Office

If your address has changed or if you wish to be removed from the RADC mailing list, or if the addressee is no longer employed by your organization, please notify RADC (ESM) Hanscom AFB MA 01731. This will assist us in maintaining a current mailing list.

Do not return copies of this report unless contractual obligations or notices on a specific document requires that it be returned.

UNCLASSIFIED

SECURITY CLASSIFICATION OF THIS PAGE (When Data Entered)

REPORT DOCUMENTATION PAGE		READ INSTRUCTIONS BEFORE COMPLETING FORM
1. REPORT NUMBER RADC-TR-82-12	2. GOVT ACCESSION NO. AD-A113 8011	3. RECIPIENT'S CATALOG NUMBER
4. TITLE (and Subtitle) RARE EARTH BORIDE ELECTRON EMITTER MATERIALS FABRICATION AND EVALUATION	5. TYPE OF REPORT & PERIOD COVERED Final Technical Report 10 Jul 80 - 9 Jul 81	
	6. PERFORMING ORG. REPORT NUMBER N/A	
7. AUTHOR(s) Lynwood W. Swanson Paul R. Davis Mark A. Gesley	8. CONTRACT OR GRANT NUMBER(s) F19628-80-C-0117	
	10. PROGRAM ELEMENT, PROJECT, TASK AREA & WORK UNIT NUMBERS 61102F 2306J136	
9. PERFORMING ORGANIZATION NAME AND ADDRESS Oregon Graduate Center 19600 N.W. Walker Road Beaverton OR 97006	12. REPORT DATE March 1982	
	13. NUMBER OF PAGES 119	
11. CONTROLLING OFFICE NAME AND ADDRESS Deputy for Electronic Technology (RADC/ESM) Hanscom AFB MA 01731	15. SECURITY CLASS. (of this report) UNCLASSIFIED	
	15a. DECLASSIFICATION/DOWNGRADING SCHEDULE N/A	
14. MONITORING AGENCY NAME & ADDRESS (if different from Controlling Office) Same		
16. DISTRIBUTION STATEMENT (of this Report) Approved for public release: distribution unlimited.		
17. DISTRIBUTION STATEMENT (of the abstract entered in Block 20, if different from Report) Same		
18. SUPPLEMENTARY NOTES RADC Project Engineer: Joseph J. Hutta (ESM)		
19. KEY WORDS (Continue on reverse side if necessary and identify by block number) Rare earth hexaborides; thermionic emission; cathode applications; zone refining; single crystals; surface analysis; life test; thermal stability; stoichiometry; lanthanum; cerium, praseodymium		
20. ABSTRACT (Continue on reverse side if necessary and identify by block number) Techniques were developed for routine preparation of single crystal rods of LaB ₆ , CeB ₆ and PrB ₆ by arc float zone refining. Single crystal, oriented samples were prepared from these rods and mounted as cathodes for testing. Several mounting systems were used, and flat, pointed cone and truncated cone thermionic cathodes were studied. Pointed field emitters of LaB ₆ (100) were also investigated. Variation of thermionic emitted current density and thermal stability of materials were studied as		

DD FORM 1 JAN 73 1473 EDITION OF 1 NOV 65 IS OBSOLETE

UNCLASSIFIED

SECURITY CLASSIFICATION OF THIS PAGE (When Data Entered)

UNCLASSIFIED

SECURITY CLASSIFICATION OF THIS PAGE (When Data Entered)

functions of rare earth element, bulk stoichiometry and crystal orientation. Life tests were performed on several different $\text{LaB}_6(100)$ cathodes. One such cathode operated for over 3000 hours at $\sim 10 \text{ A/cm}^2$ emitted current density with no serious physical degradation. Surface properties of the materials were investigated by various surface analysis techniques.

Accession For	
NTIS CRA&I	<input checked="" type="checkbox"/>
DTIC TAB	<input type="checkbox"/>
Unannounced	<input type="checkbox"/>
Justification	
By _____	
Distribution/	
Availability Codes	
Dist	Avail and/or Special
A	



UNCLASSIFIED

SECURITY CLASSIFICATION OF THIS PAGE (When Data Entered)

TABLE OF CONTENTS

	Page
List of Illustrations	ii
List of Tables	v
Preface	vii
Summary	viii
A. Introduction	1
B. Results of the Contract Period	6
1. Task I: Single Crystal Growth	6
(a) Review of Fabrication Methods	6
(b) Results Using the Arc Float Zone Refining Technique	8
2. Task II: Single Crystal Emitter Structure Fabrication	25
(a) Field Emitter Structures	25
(b) Thermionic Emitter Structures	26
3. Task III: Thermal and Field Emission Characterization	29
(a) Background	29
(b) Thermionic Work Functions	33
(c) Thermionic Emission Distributions	41
(d) Life Test Results	62
(e) Field Emission Characterization	67
4. Task IV: Surface and Bulk Properties Characterization	84
(a) Background	84
(b) Surface Composition and Geometry	86
(c) Volatility	90
(d) Retarding Work Functions	96
(e) Theoretical Model of Work Function Behavior	101
C. Discussion and Conclusions	109
1. Effect of Rare Earth Compound	109
2. Effect of Bulk Stoichiometry	109
3. Effect of Crystal Face	114
4. Surface Stoichiometry	114
5. Future Work	115
References	117

LIST OF ILLUSTRATIONS

	Page
Figure 1. Sample of <100> oriented LaB ₆ rod prepared by the arc float zone refining technique.	10
Figure 2. SEM photo (8900 X) of typical surface region of LaB ₆ (100) showing defect pits (average size ~ .2 μm).	13
Figure 3. SEM photo (15700 X) of LaB ₆ (100) surface feature with second phase inclusion. The feature is ~ 4.5 μm across.	15
Figure 4. Scanning Auger maps of inclusion in LaB ₆ (100) cleaved surface. a, SEM photo; b, La(NOO) map; c, La(MNN) map; d, boron map; e, oxygen map; f, carbon map.	16
Figure 5. Auger spectrum (typical) taken inside pit, second phase material (sputtered).	19
Figure 6. Auger spectrum of smooth LaB ₆ (100) fracture surface (sputtered).	20
Figure 7. Diagram of field emitter and resistively heatable filament support structure used for single crystal material of LaB ₆ .	27
Figure 8. Micrograph profiles of an LaB ₆ field emitter which has been operated in a TF mode.	28
Figure 9. Photos of (a) 90° cone angle pointed LaB ₆ emitter and (b) 60° cone angle emitter with a 40 μm flat on end.	30
Figure 10. Two methods of mounting LaB ₆ single crystal thermionic emitters. (a), Directly heated Vogel mount; (b), Re cup mount.	31
Figure 11. Emitter temperature vs heating current and power is given for an LaB ₆ thermionic emitter constructed according to Figure 10(b).	32
Figure 12. Zero field thermionic work function vs. temperature plots for LaB _{5.86} single crystals; ● initial and ○ final curves obtained from the indicated planes.	36
Figure 13. Comparison of emitted current density behavior of various LaB _{5.86} crystal faces.	37
Figure 14. Comparison of emitted current density behavior of (100) planes of RB ₆ compounds and the (210) LaB _{6.09} surface.	39
Figure 15. Schematic drawing of display system used for studies of thermionic emission distributions.	42
Figure 16. Thermionic emission patterns from a 90° pointed LaB ₆ (100) cathode, early in life, at the indicated Wehnelt bias voltages, V _W .	43

List of Illustrations (Cont.)

	Page
Figure 17. Thermionic emission patterns from LaB ₆ (100) pointed cathode, 90° cone angle, after 380 hours of life at 1700 K. Patterns were observed at the indicated Wehnelt bias voltages, V _W .	46
Figure 18. Total emission current I-V characteristic of 90° pointed LaB ₆ (100) cathode used in thermionic emission distribution studies. Patterns corresponding to indicated points A-F are shown in Figures 16 and 17.	50
Figure 19. Thermionic emission patterns from LaB ₆ (100) truncated cathode, 60° cone angle, after 5 hours of life at 1700 K. Patterns were observed at the indicated Wehnelt bias voltages, V _W .	52
Figure 20. Thermionic emission patterns from a LaB ₆ (100) truncated cathode, 60° cone angle, after ~ 570 hours life at 1700 K. Patterns were observed at the indicated Wehnelt bias voltages, V _W .	56
Figure 21. I-V characteristics of LaB ₆ (100) truncated cathode, 60° cone angle, after 5 hours of life at 1700 K.	59
Figure 22. J-V characteristics of a 60° truncated cathode at various temperatures.	60
Figure 23. Diagram of optical column designed for emission spatial distribution measurements. The emission pattern is rastered across the 10 μm aperture and displayed on an oscilloscope.	61
Figure 24. New truncated LaB ₆ (100) cathode used in Vogel mount assembly a, cathode in Wehnelt aperture; b, front view of cathode; c, d, side view of flat region, showing opposite sides. The flat end of the cathode is 40 μm across.	63
Figure 25. Truncated LaB ₆ (100) cathode after 3000 hours life at 1800 K. Views of a-d are the same magnification and approximately same orientations as in Figure 24.	64
Figure 26. (a) Hydrogen field ion image of a (100) oriented LaB ₆ emitter after field evaporation in H ₂ , BIV = 13 kV.	68
(b) Field electron image of H ₂ field evaporated end form.	69
(c) Helium field ion image of a (100) oriented LaB ₆ emitter after field evaporation in He, BIV = 24 kV.	70
(d) Field electron image of the He field evaporated end form.	71
(e) Hydrogen field ion image of a (100) oriented LaB ₆ emitter after annealing 15 min. at 1800 K.	72

List of Illustrations (Cont.)

	Page
(f) Field electron image of thermally annealed end form.	73
Figure 27. Plot shows the variation of FN slope of a LaB_6 emitter (after initially field evaporating in H_2 at 77 K) with heating at the indicated temperature for 2 minutes.	77
Figure 28. FIM (unprimed) and FEM (primed) patterns. The BIV = 13 kV for the hydrogen ion images. The patterns correspond to the indicated temperatures on the Figure 27 curve.	79
Figure 29. FIM (unprimed) and FEM (primed) patterns. The BIV = 13 kV for the hydrogen ion images. The patterns correspond to the indicated temperatures on the Figure 27 curve.	80
Figure 30. FIM (unprimed) and FEM (primed) patterns. The BIV = 13 kV for the hydrogen ion images. The patterns at each temperature correspond to a point on Figure 27.	81
Figure 31. FIM (unprimed) and FEM (primed) patterns. The BIV = 13 kV for the hydrogen ion images.	82
Figure 32. FIM (unprimed) and FEM (primed) patterns. The BIV = 13 kV for the hydrogen ion images.	83
Figure 33. Diagram of surface analysis probes available on the ultra-high vacuum chamber.	85
Figure 34. LEED patterns taken at $V_p = 100$ V of selected LaB_6 crystals used in this study: (a) (100); (b) (110); (c) (111).	91
Figure 35. FERP I(V) data for various $\text{LaB}_{5.86}$ crystal faces. The theoretical curve, drawn once for clarity purposes, represents the I(V) curve if all electrons were collected.	97
Figure 36. FERP I(V) data for various RB_6 crystal faces.	98
Figure 37. Derivative curves of the Figure 35 curves obtained from FERP analysis of the indicated single crystal planes.	99

LIST OF TABLES

		Page
Table I	Statement of Goals and Objectives	2
Table II	Summary of Proposed Tasks	3
Table III	Summary of Surface Analysis Instruments Utilized	5
Table IV	Summary of Single Crystal Growth Methods	7
Table V	Stoichiometries of Zone Refined RB_6 Materials Prepared in This Laboratory	12
Table VI	AES Data for Cleaved Surface Inclusion (Pit) Ar^+ Sputtered, $\sim 500 \text{ \AA}$	18
Table VII	Mass Spectrometry Analysis of $LaB_{6.2}$ Material Obtained from MRC (PPM by wt.)	22
Table VIII	Carbon and Oxygen Impurity Levels in PPM by Weight in Various RB_6 Materials	24
Table IX	Bulk Properties of LaB_6 and $LaBO_3$	24
Table X	Summary of Effective Thermionic Work Function Values of Various Crystal Planes of LaB_6	34
Table XI	Summary of Effective Thermionic Work Function Measurements on RB_6 Single Crystal Surfaces ($T = 1600-1700 \text{ K}$)	40
Table XII	Effects of Refractory Contaminants on LaB_6 Surfaces	66
Table XIII	Summary of Best Image Voltages (BIV) and FN Slopes for the Indicated Image Gas and End Form of the LaB_6 Emitter	75
Table XIV	Ratio of AES Peak Heights for Various Crystal Faces of RB_6 Compounds (Primary Beam Energy 5 kV)	87
Table XV	Auger Peak Height Ratios for In Situ Fractured and Ar^+ Sputtered $LaB_6(100)$ Surfaces Primary Beam Energy, 5.0 keV	89
Table XVI	Vaporization Energies of the Rare Earth Element (E_R) and Boron (E_B) from (100) Surfaces of RB_6 Compounds	90
Table XVII	Relative Values of Pre-Exponential Terms in Eq. 5	94
Table XVIII	Vaporization Data for LaB_6 Samples (Variation with Stoichiometry)	95
Table XIX	FERP Work Functions of RB_6 Single Crystal Surfaces	100
Table XX	Values of N_1 and N_2 for Eq. (13) Based on RB_6	105
Table XXI	Work Function of LaB_6	106

List of Tables (Cont.)

	Page
Table XXII Comparison of Calculated and Measured Work Functions	108
Table XXIII Work Function Summary for (100) Faces	110
Table XXIV Figure of Merit of (100) Faces of RB_6 Compounds	110
Table XXV LaB_6 (100) Work Function Summary	111
Table XXVI Relative Figures of Merit* of LaB_6 Surfaces at 1600 K	113
Table XXVII Normalized Auger Peak Height Ratios for In Situ Fractured, Ar^+ Sputtered and Heated $LaB_{6.09}$ (100) Surfaces Primary Beam Energy, 5.0 keV $T = 300$ K	115

PREFACE

Scientific and technical contributions to this report were made by A. E. Bell, A. Cossitt, P. R. Davis, M. A. Gesley, N. A. Martin, J. H. Orloff, J. Puretz and L. W. Swanson.

SUMMARY

Single crystal rods of LaB_6 , CeB_6 and PrB_6 have been prepared by a seeded, arc float-zone refining technique (Section B-1). Pointed and flat cathodes mechanically cut from these rods have been polished and mounted in various types of structures for evaluation as thermionic emitters. In addition, needles of LaB_6 , grown by the aluminum flux method, have been electrolytically pointed and studied in field emission and field ionization modes (Section B-2).

Thermionic cathodes have been evaluated with respect to R (R = La, Ce or Pr), crystal face and stoichiometry. Pointed and truncated cone LaB_6 cathodes of (100) orientation were subjected to life test studies, with a useful lifetime of over 3000 hours being recorded for a particular mounting system (Vogel mount) (Section B-3). Detailed surface studies were made of various crystal faces of LaB_6 , CeB_6 and PrB_6 samples as a function of bulk stoichiometry (Section B-4). Analysis techniques included Auger electron spectroscopy (both fixed point and scanning), low energy electron diffraction, emission and retarding potential work function measurement, desorption mass spectrometry and field emission and field ion microscopy. Surface morphologies at various stages of preparation and life were characterized by scanning electron microscopy.

Cathodes were evaluated with respect to the ratio of electron emission to material evaporation rate, a figure of merit of cathode performance (Section C). Of primary importance to the figure of merit is the rate of evaporation which varies considerably more with stoichiometry than does the emission current, all other things being equal. Since lowest evaporation rate and highest electron emission do not occur at the same stoichiometry, at thermionic emission temperatures, there is necessarily a trade off of lifetime and emitted current density. The figure of merit represents a measure of overall optimum performance as a cathode. On this basis, $\text{LaB}_{6.09}(100)$ proved superior to the other samples investigated.

The effect of cathode shape (pointed vs truncated cone) upon emission distribution was also studied, with promising results obtained for the

truncated cone (Section B-3). This cathode shape may yield improvement in performance of small spot size electron guns.

A theoretical model of the work function behavior of RB_6 single crystal faces has been applied to the data, with encouraging results. The only physical parameters used in this model are surface geometry and valence of surface atoms, yet the model is able to predict the order of increasing work function of major planes, $(100) < (110) < (111)$, for LaB_6 , and even yields correct work function values within 0.1 or 0.2 eV.

The experimental results are discussed from the point of practical applications. The use of $LaB_6(100)$ and perhaps $CeB_6(100)$ cathodes in demonstration projects is indicated. Only after such actual field trials will the merits of these high stability cathode materials be appreciated.

A. Introduction

The major goal of this program has been the fabrication and characterization of single crystal specimens of the rare earth hexaborides with respect to electron emission properties. During the latter half of the 1970's a great deal of interest in the electron emission properties of LaB_6 was stimulated by the need for higher brightness thermionic emitters and the advent of relatively easy methods of growing high purity single crystals. An expanded statement of the goals and objectives of this program is outlined in Table I. The research has been subdivided into four Tasks, as indicated in Table II.

The primary problems to be addressed in this work are twofold:

- (1) Materials problems associated with the fabrication of single crystal RB_6 type compounds; and
- (2) The identification of the RB_6 type material best suited to function as a high current density, long lived electron emitter.

The approach we used to solve problem 1 incorporated the following major considerations:

- (a) Control and minimization of bulk impurities (especially carbon)
- (b) Control and measurement of bulk RB_6 stoichiometry
- (c) Convenient control of crystallographic orientation
- (d) Selection of a fabrication technique applicable to several RB_6 type compounds
- (e) Determination of suitable mechanical and electrochemical techniques for fabricating planar and conical emitter shapes with minimum surface roughness.

As will be described in subsequent sections our past work allowed us to concentrate on a particular fabrication technique that appeared best suited in the light of the above issues. Thus, further effort was expended not on exploring the various fabrication methods currently available, but rather on perfecting the one in which we had prior experience and had good expectation of meeting the required objectives. This approach has proved to be successful. Results are given under Tasks I and II in Section B of this report.

The identification of the RB_6 material and crystal orientation best suited to perform as an electron emitter (problem 2) required several

TABLE I

Statement of Goals and Objectives

Goal I: Fabrication of Single Crystal RB_6 Emitter

Required Objectives:

1. Select single crystal fabrication method.
2. Select RB_6 materials (feedback from Goal II required).
3. Implement single crystal fabrication method.
4. Characterize single crystals with respect to:
(a) crystal orientation; (b) purity; (c) stoichiometry;
(d) point defect density; (e) homogeneity.
5. Fabricate proper shaped emitter and resistively heated emitter support structure.
6. Test emitter and support structure for mechanical durability at operating temperature.

Goal II: Characterization of Single Crystal RB_6 Emitter Performance

Required Objectives:

1. Determine lowest work function RB_6 material commensurate with low volatility.
2. Determine the crystal face of (1) above that possesses the lowest work function without undergoing geometric reconstruction during operation.
3. Measure emission characteristics in the thermal and field emission operating modes.

TABLE II

Summary of Proposed Tasks

<u>Major Tasks</u>	<u>Major Task Breakdown</u>
Task I Single Crystal Growth	<ul style="list-style-type: none"> ● Choose best method ● Establish orientation control ● Minimize impurity levels ● Determine and control stoichiometry
Task II Single Crystal Emitter Structure Fabrication	<ul style="list-style-type: none"> ● Determine optimum grinding and chemical polishing techniques ● Test durability of resistive heating structure ● Measure heating power requirements ● Fabricate pointed and flat single crystal emitters
Task III Thermal and Field Emission Characterization	<ul style="list-style-type: none"> ● Measure thermionic work functions and current density of flat cathodes ● Measure angular distribution of brightness of pointed cathodes ● Measure energy spread of pointed cathodes ● Measure noise spectrum of pointed cathodes ● Life test pointed cathode structure
Task IV Surface and Bulk Properties Characterization	<ul style="list-style-type: none"> ● Measure volatility of RB_6 materials ● Examine surface geometry and composition ● Measure retarding work functions vs temperature

physical properties of the emitter to be evaluated with concomitant control of the above mentioned material quality. In the case of thermionic emission the principal properties of interest are:

- (a) Material volatility
- (b) Emitter current density or surface work function
- (c) Surface geometric and compositional stability with operating time.

Thus, for a thermionic emitter the principal figure of merit for most applications is the temperature dependence of the absolute magnitudes and ratio of electron emission to evaporation rate. Results of thermionic emission and field emission characterization are given under Task III.

Lanthanum hexaboride has been studied more than any other rare earth boride. However, the chemical and physical properties of the rare earth lanthanides are quite similar, resulting in similar properties for their borides. In particular, the hexaborides of La, Ce, Pr and Nd have nearly identical lattice constants and phase diagrams. A further common and complicating set of properties are low bulk diffusion rates compared with evaporation and the occurrence of a congruent vaporizing composition (CVC) near the $B/R \approx 6$ stoichiometry. In certain temperature ranges this leads to a thin surface phase of differing B/R stoichiometry. The cubic structure of the lattice of boron octahedra surrounding the rare earth ions in a macroscopic crystal largely determines the chemical and physical properties of these hexaborides, but the electronic properties of the crystal depend strongly upon the rare earth metal.

It thus was imperative for careful and detailed surface analysis work to be carried out in conjunction with the electron emission studies. Table III lists the surface analysis facilities which were used for this work. Surface characterization results are discussed under Task IV.

TABLE III

Summary of Surface Analysis Instruments Utilized

<u>Item</u>	<u>Functions</u>
Quadrupole Mass Spectrometer	<ul style="list-style-type: none"> • Measure evaporation rates of volatile mass species and their temperature dependence
Auger Electron Spectrometer (AES)	<ul style="list-style-type: none"> • Measures surface composition over wide range of temperature
Guard Ring Collector	<ul style="list-style-type: none"> • Measures emitter thermionic current density and its temperature dependence
Field Emission Retarding Potential (FERP) Gun	<ul style="list-style-type: none"> • Measures absolute retarding potential surface work function and energy dependence of electron reflection coefficient
Low Energy Electron Diffraction (LEED) Optics	<ul style="list-style-type: none"> • Measures surface lattice periodicity from electron diffraction pattern • Also can be used as AES spectrometer
Field Electron Microscope	<ul style="list-style-type: none"> • Measures crystallographic dependence of work function
Field Ion Microscope	<ul style="list-style-type: none"> • Overall view of relative thermal stability of various crystal faces
Scanning Auger Microscope (SAM)	<ul style="list-style-type: none"> • Measures elemental distribution over the surface
Scanning Electron Microscope (SEM)	<ul style="list-style-type: none"> • Determines surface microstructure

B. Results of the Contract Period

1. Task I: Single Crystal Growth

(a) Review of Fabrication Methods

In early studies of the emission properties of RB_6 materials polycrystalline samples were used. Unusually high thermionic emission current densities (compared to pure refractory metals) and relatively low volatilities were obtained using LaB_6 powder which was either sintered or bonded to refractory metal surfaces. However, the emission characteristics of polycrystalline samples are difficult to characterize with respect to crystal face dependent surface properties. Thus, recent effort has been devoted to the study and use of single crystal materials prepared by several different methods.

The primary methods of growing rare earth hexaboride single crystals suitable for thermionic emission, field emission and surface characterization studies have been the molten aluminum flux¹ and zone refinement techniques.²⁻⁴ Other methods, which are summarized in Table IV, such as vapor phase⁵ and electrolytic crystallization,⁶ produce crystals whose orientation and shape are more difficult to control. Of all the techniques, float zone refinement has been developed most extensively. It is ideally suited to the growth of high purity, long crystals which may either be oriented as desired with a seed crystal during the zone pass, or cut into samples of the desired orientations. Seeded growth allows an arbitrary axial orientation to be achieved and is thus the more flexible technique for producing long crystals suitable for field and thermionic emission cathodes. To date, (100), (110), (111), (210), (211), (346) and (321) oriented crystals have been grown by the float zone seeding technique.

The zone refinement or float zone method requires that a zone of the starting material, usually in the form of a hot pressed (sintered) rod, be melted. The molten zone is then swept up the rod, carrying soluble impurities with it. Solidification behind the zone causes single crystal growth and, if a single crystal seed is used at the initiation of the zone, the solidified region will have the axial orientation of the seed. Usually two or three passes are required to achieve maximum purity of the sample.

TABLE IV

Summary of Single Crystal Growth Methods

<u>Method</u>	<u>Crystal Size and Shape</u>	<u>Orientation</u>	<u>Minimum Impurity (P.P.M.)</u>	<u>Ref.</u>
1. Molten Al Flux	Needles (2-7 mm long) Plates (2 x 2 mm)	(110) & (100)	1000 [*]	1
2. Electrolytic Crystallization	Cubic (6 x 6 x 5 mm)	?	?	6
3. Float Zone				
(a) RF Heating	Rod (7 x 60 mm)	Random ^{**}	< 400	2
(b) Laser Heating	Rod (1.1 x 60 mm)	Selected	< 400	3
(c) Arc Heating	Rod (3.0 x 30 mm)	Selected	45	4
4. Chemical Vapor Decomposition	Needles (2-5 mm long)	?	?	5

* Mostly clusters of Al rich phase

** Contained 1 mm³ subgrain regions

Several float zone melting methods have been used as outlined in Table IV, including RF heating,² laser melting³ and arc melting.⁴ The melting process must take place in an inert gas pressure in order to reduce evaporation. Arc melting in argon is capable of producing high quality LaB₆ crystals of 1-3 mm diameter and 2 to 3 cm lengths on a routine basis, if starting materials of sufficient purity (low carbon) are used.⁴ From the standpoint of simplicity and low cost and achieving high purity, oriented single crystal rods from which both float and pointed emitter shapes can be fabricated, the arc melted float zone method is preferable. The only advantage of the much more costly laser and RF melt methods is the possibility of fabricating larger rod diameters. Work by Verhoeven, et al.,⁴ and ourselves has shown that the electrode material used in the arc melt method does not result in contamination of the single crystal rod.

In previous LaB₆ work, a Ta counter electrode was used to establish and maintain the float zone arc. We have found that Ta is unsuitable for PrB₆ work, but that W operates satisfactorily. However, we find that the best counter electrode is a pointed piece of the starting material. That is, a pointed, hot pressed rod of PrB₆ is the best counter electrode for PrB₆ zone refining. This statement also seems to hold for LaB₆ and CeB₆. The improvement resulting from this modification is a more stable and controllable arc and the removal of potential electrode contaminants.

(b) Results Using the Arc Float Zone Refining Technique

The arc float zone refining technique allows for some control of sample stoichiometry by varying the starting material composition and varying the number of zone passes. When starting material of B/La = 6.0 stoichiometry is used, three or more zone passes will result in an observable second phase of metallic gray color (usually located near the end of the pass) and a reduced B/La ratio. We have tried to overcome this problem by the use of starting material with B/La = 6.2 and the use of two zone passes. These experiments have been successful in reducing the macroscopic appearance of second phase material.

We have succeeded in preparing seeded single crystal rods of LaB₆, CeB₆ and PrB₆ by this method. Laue x-ray backscattering analysis of seeded

<100> oriented rods shows that routine orientation to within 2° of the desired orientation is possible for all three compounds. Higher index directions such as the <211> have also been aligned along the rod axis to within 2° . Figure 1 shows a sample of <100> oriented LaB_6 rod prepared by the arc float zone refining technique.

Zone refined RB_6 rods were analyzed by wet chemical methods to determine precise stoichiometries. In addition, the hot pressed starting material (obtained from MRC, listed as $\text{LaB}_{6.2}$) for the LaB_6 samples was analyzed for total impurities by wet chemical techniques. It was found to contain $\sim 8\%$ (by weight) of total impurities, including ~ 5 atomic % Al. Impurities in the zone refined rods were undetectable by wet chemical analysis, but their precise stoichiometries were determined by the following procedure.

Between 100 mg and 1 gram of the rare earth hexaboride was dissolved in 6-20 ml of 1:1 HNO_3 either in an open beaker or, in the case of PrB_6 , in a Parr acid digestion bomb which was heated to $\sim 108^\circ\text{C}$ for 10 minutes. Powdered samples of LaB_6 from Cerac, quoted as being 99.9% pure, were too active for use of the Parr bomb. However, we recommend that the Parr bomb dissolution procedure be used for all RB_6 zone refined samples in future analysis, since this procedure greatly speeds up dissolution of RB_6 and also prevents loss of B by volatilization of H_3BO_3 which has a significant vapor pressure at temperatures near 100°C .

The most widely recommended⁷ technique for precise assay of B is the mannitol-borate titration procedure in which excess acid used for dissolution of RB_6 is neutralized to pH 7, followed by addition of mannitol. This converts H_3BO_3 to a strong acid which can then be titrated with a strong base (NaOH) either with an indicator or, as was the case in this work, with a pH meter in order to detect the end point. Prior to titration the La^{3+} was masked as a possible interfering ion by addition of a slight excess of EDTA.⁸

The rare earth metals were determined by a potentiometric titration against EDTA.⁹ The reference electrode was either Ag/AgCl or $\text{Hg}/\text{Hg}_2\text{Cl}_2$, while the other electrode was a Hg amalgamated gold wire. A few drops of $\text{Hg}^{2+}(\text{EDTA})^{2-}$ was added to the sample solution in order to monitor the

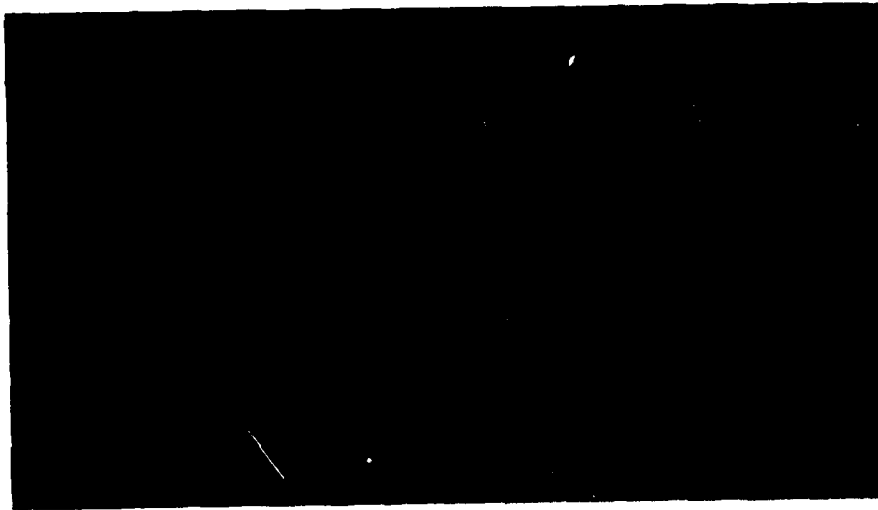


Figure 1. Sample of $\langle 100 \rangle$ oriented LaB_6 rod prepared by the arc float zone refining technique.

concentration of R during the titration. Titration curves similar to those obtained during acid base titrations are obtained with the end point occurring at the inflection point of the titration curve.

The detailed analytical procedure used was as follows: the RB_6 sample was dissolved in 1:1 HNO_3 at the rate of 6 ml of the dilute HNO_3 /100 mg of RB_6 sample. Up to about 200 mg of the hexaboride can be accommodated in a Parr acid digestion bomb which was heated for 10 minutes at $\sim 108^\circ C$. The resultant acidified solution of R^{3+} and H_3BO_3 was diluted with 50 ml of distilled water, neutralized to pH $\sim 3-4$ and diluted in a volumetric flask to ~ 1 gram/liter of RB_6 .

A 25 ml pipetted aliquot of this solution was treated with an excess of EDTA, to which 25 ml of distilled water was added, and then neutralized to pH 7 with 20% KOH and 0.02 M KOH. After the addition of 6-8 grams of mannitol (1 gram/10 ml of solution) the titration was carried out using a pH meter to identify the end point.

The rare earth was determined by taking a 25 ml aliquot of the RB_6 solution, adding 25 ml of distilled water and neutralizing to pH ~ 7 . Next, 50 ml of 0.1 M acetic acid/sodium acetate buffer was added together with 6 drops of $Hg^{2+} EDTA^{2-}$ complex prepared by adding an equivalent amount of EDTA to 25 ml of 0.01 M $Hg(NO_3)_2$ solution. The titration was carried out potentiometrically using a Ag/AgCl reference electrode and an amalgamated gold wire which was periodically cleaned by immersion in dilute nitric acid. Typically 100-200 mV changes in potential occurred during a run with steep drops in potential occurring at the end point.

Various other metal ions, e.g. Al^{3+} , Fe^{3+} will interfere with the La determinations but can however frequently be masked. Aluminum for example^{10,11} may be masked by the addition of sulfosalicylic acid and Fe^{3+} may be removed by reducing it with ascorbic acid.

Stoichiometry values determined for the zone refined RB_6 rods prepared in this study are shown in Table V. Since the amount of material required for each analysis is relatively large, the uncertainty quoted in Table V reflects the estimated cumulative error in the analysis procedure. Actual stoichiometry variation from one zone refining run to another has not been determined.

TABLE V
 STOICHIOMETRIES OF ZONE REFINED RB₆
 MATERIALS PREPARED IN THIS LABORATORY

RB ₆ Compound	Precise Stoichiometry
LaB ₆	LaB _{6.02 ± 0.05}
CeB ₆	CeB _{6.2 ± 0.05}
PrB ₆	PrB _{5.87 ± 0.05}

In order to study the perfection of LaB₆ single crystals, workers in the past have etched cleaved surfaces in HNO₃ solutions to preferentially enlarge defect pits and allow studies to be made by optical microscopy.¹² We routinely use scanning electron microscopy (SEM) for various studies, so we applied this technique to the study of cleaved LaB₆ surfaces. Because SEM can resolve submicron features with ease, we found it unnecessary to etch or otherwise disturb the freshly cleaved surface.

Two distinctly different types of surface features were observed in our SEM studies of cleaved (100) LaB₆. Figure 2 shows a typical region of the surface at a magnification of about 9×10^3 . The square pits observed average about .2 μm on a side and have sharp, square corners. Occasionally, two or three pits run together to form a rectangular feature. The average surface density of these pits for a single pass rod was $\sim 2.5 \times 10^7/\text{cm}^2$. In 2-pass rods the pit density was $< 10^6/\text{cm}^2$. In previous work, using the HNO₃ etching technique, defect densities of $\sim 10^3/\text{cm}^2$ for Al flux grown LaB₆(100)¹ and $1.6 \times 10^6/\text{cm}^2$ for laser zone refined LaB₆(100)¹² cleaved surfaces have been measured. The values reported here are of the same order of magnitude as those observed for the laser zone refined material. It is not clear what causes the larger defect density associated with the arc float refinement technique. Our samples were prepared from B/La = 6.2 starting material, whereas Takagi and Ishii¹² presumably started with material of stoichiometry B/La = 6.0 and made one or two zone passes.



Figure 2. SEM photo (8900 X) of typical surface region of LaB₆ (100) showing defect pits (average size $\approx 1.2 \mu\text{m}$).

The second type of surface feature observed in our SEM studies is shown in Figure 3, at a magnification of $1.5 \cdot 10^4$. Features of this type have linear dimensions approximately 10-20 times larger than those of Figure 2 and are very sparsely distributed over the surface ($\sim 1 \times 10^4/\text{cm}^2$ in LaB_6 and CeB_6). They are difficult to count because their density is extremely low. Each feature of this type is a square or rectangular hole with well-rounded corners, containing apparently randomly crystallized material. We believe this randomly crystallized material represents a second phase which was still molten at the time the LaB_6 zone solidified and crystallized later when the zone cooled to a somewhat lower temperature. The melting point of LaB_6 is 2715 C.¹³

The presence of rounded corners on the surface features of the second type is somewhat curious. These pits have an almost artificial appearance. The rounded corners and smooth sides of the features are apparently related to the local phase equilibrium between solid LaB_6 and molten second phase material during cooling.

Auger electron spectroscopic analysis of the material within the second type of feature can be summarized as follows. SAM maps (Figure 4) of the region in and around a pit show carbon and oxygen enrichment and boron depletion inside compared with the smooth surrounding surface. Lanthanum also appears slightly depleted, but this is probably caused by Auger yield reduction within the pit.

Careful AES point analyses are summarized in Table VI, with typical spectra inside and outside the pit shown in Figures 5 and 6, respectively after sputter removal of approximately 500 Å of material. Based upon these results, some conclusions may be drawn concerning the composition of the inclusion. The $\text{La}(78)/\text{La}(625)$ peak ratio is approximately the same inside and outside the surface feature. However, the $\text{B}/\text{La}(625)$ ratio in the second phase material is $\sim 1/4$ to $1/2$ times that in the surrounding LaB_6 surface. The $\text{O}/\text{La}(625)$ ratio, on the other hand, is 3.5-4.0 times larger in the second phase than in the surrounding chemisorbed CO layer. Additionally, the $\text{La}(625)$ peak (Figure 5) shows significant splitting in the second phase compared with the $\text{La}(625)$ peak of LaB_6 (Figure 6). We have observed such splitting in previous studies of oxygen chemisorption, where boron-oxygen and lanthanum-

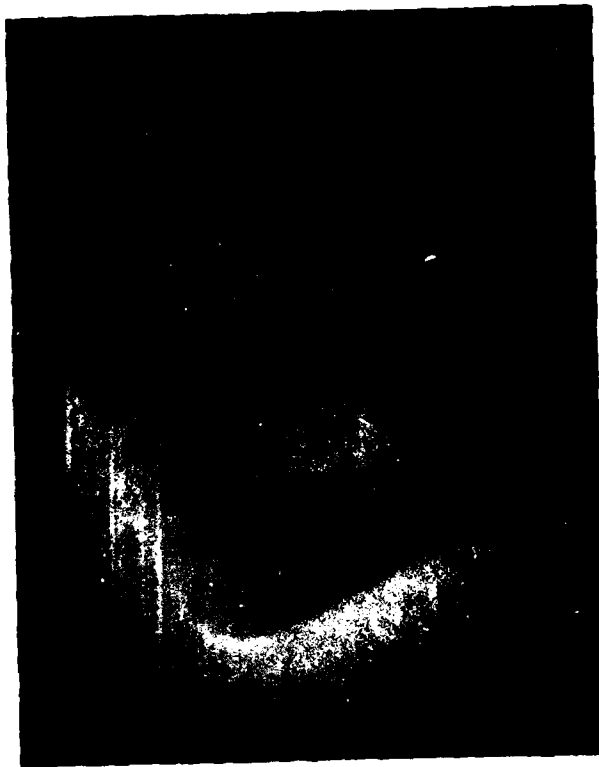
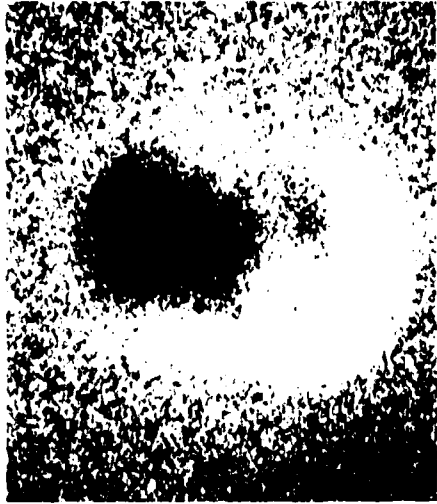


Figure 3. SEM photo (15700 X) of LaB. (100) surface feature with second phase inclusion. The feature is $\approx 4.5 \mu\text{m}$ across.



a. SEM photo



b. La(N00)

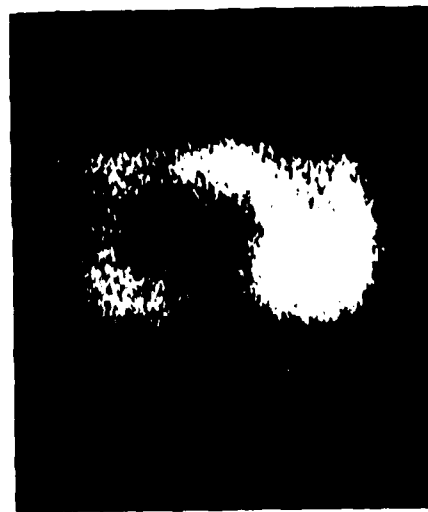
Figure 4. Scanning Auger maps of inclusion in $\text{LaB}_6(100)$ cleaved surface. a, SEM photo; b, La(N00) map; c, La(MNN) map; d, boron map; e, oxygen map; f, carbon map.



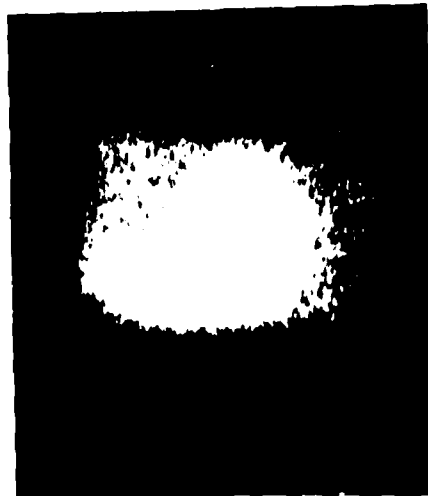
c. La (MNN)



d. B (KLL)



e. O (KLL)



f. C (KLL)

Figure 4. (continued)

TABLE VI

AES Data for Cleaved Surface Inclusion (Pit)

Ar⁺ Sputtered, ~ 500 Å

Analysis [*] Point	Peak-to-Peak Heights				
	La(78)	La(625)	B(179)	C(272)	O(510)
1	4.5	5.1	2.6	12.4	17.4
2	7.9	7.7	15.5	2.2	7.5
3	4.8	4.45	3.6	5.5	17.4
4	5.5	5.25	4.85	5.9	17.4
5	4.7	4.5	4.7	7.2	17.4
6	3.9	4.45	2.7	12.2	17.4

* Point 2 is on smooth surface outside pit. Other points inside pit.
See Figure 4.

	Peak Ratios			
	$\frac{\text{La}(78)}{\text{La}(625)}$	$\frac{\text{B}(179)}{\text{La}(625)}$	$\frac{\text{C}(272)}{\text{La}(625)}$	$\frac{\text{O}(510)}{\text{La}(625)}$
1	0.88	0.51	2.43	3.41
2	1.03	2.01	0.29	0.97
3	1.08	0.81	1.24	3.91
4	1.05	0.92	1.12	3.31
5	1.04	1.04	1.60	3.87
6	0.88	0.61	2.74	3.91

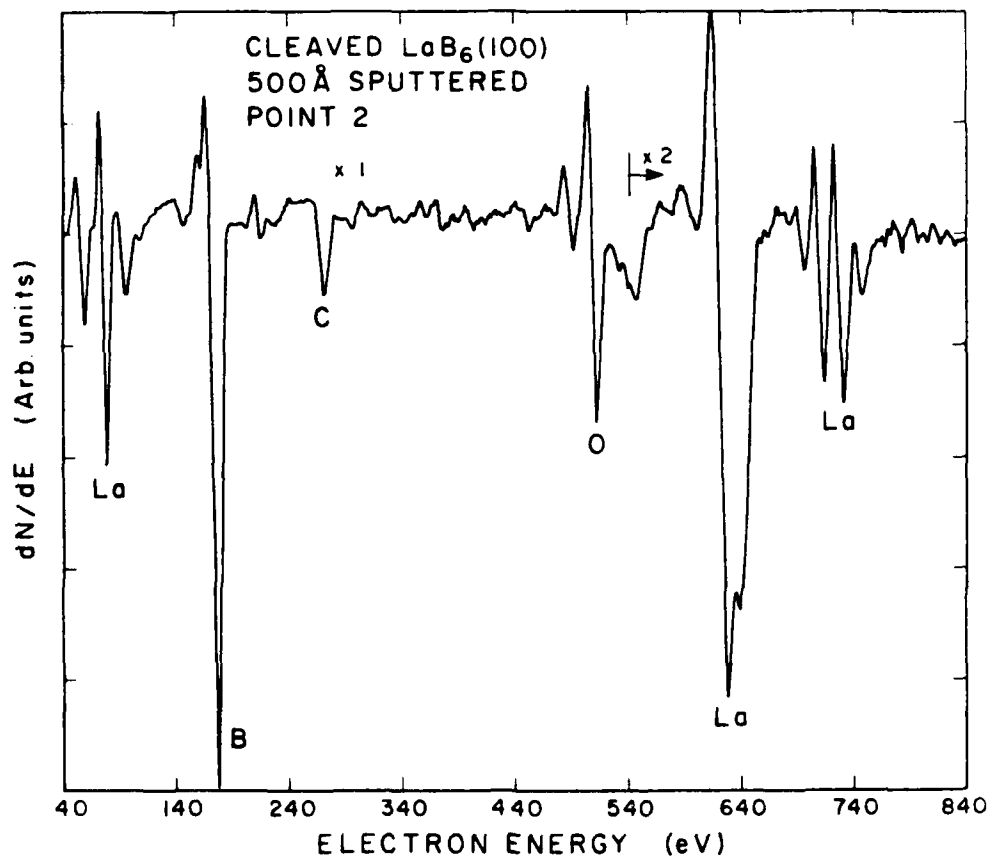


Figure 6. Auger spectrum of smooth $\text{LaB}_6(100)$ fracture surface (sputtered).

oxygen compounds are formed.¹⁴ This splitting is not observed during CO chemisorption.

Taken together, these results strongly suggest that the second phase is a La-B-O ternary compound of approximate stoichiometry La(1), B(1-2) and O(unknown, possibly 2-4) based upon the relative AES signals of B and La in LaB₆ and O in an adsorbed CO layer. The presence of a significant amount of C suggests that it may also be part of the compound. However, the fact that the C concentration varies by a factor of ~ 2.5 from point to point within the inclusion may indicate that a large part of the C was in solution in the molten second phase, probably precipitating as the second phase cooled and crystallized, yield an anisotropic distribution of C as has been observed.

We speculate, that the second phase material is the ternary compound LaBO₃. This compound has excellent thermal stability and should be formed under the preparation conditions of our specimens if oxygen is available. Our arc zone refining step is performed in very low oxygen partial pressure (< 10⁻⁵ torr) in an atmosphere of high purity argon, so that oxidation may be minimized. However, oxygen is present in the hot pressed starting material which we use.

We have recently had LaB₆ samples analyzed for the trace elements carbon and oxygen. These analyses have shown an oxygen concentration of 13,100 ppmw in the starting hot pressed material obtained from MRC and 240 ppmw in single crystal, 2-pass zone refined rods which we have prepared from the starting material. Corresponding carbon concentrations are 2160 ppmw and 40 ppmw, respectively. Table VII identifies the impurity levels of LaB₆ both before and after zone melting.

Table VIII gives the initial carbon and oxygen concentration levels in the various starting materials and zone melted LaB₆. In previous studies of LaB₆ arc zone refined material, Noack and Verhoeven¹⁵ showed that the oxygen concentration was reduced in the first zone pass but not in subsequent zone passes. In that work, oxygen concentrations as low as 370 ppmw in the starting material (obtained from Cerac) and 15-20 ppmw in the zone refined material were observed. Because the oxygen concentrations measured

TABLE VII
 MASS SPECTROMETRY ANALYSIS OF $\text{LaB}_{6.2}$ MATERIAL
 OBTAINED FROM MRC (PPM BY WT.)

Element	As Received	1 Pass Zone Refined	2 Pass Zone Refined
V	< 0.1	< 0.1	< 0.1
Th	0.13	< 0.1	< 0.1
Bi	0.72	< 0.2	< 0.1
Pb	9.1	0.12	0.1
Tl	0.17	< 0.16	< 0.16
Hg	NR	NR	NR
Au	< 0.1	< 0.1	< 0.1
Pt	< 0.1	< 0.1	< 0.1
Ir	< 0.1	< 0.1	< 0.1
Os	< 0.1	< 0.1	< 0.1
Rh	0.1	< 0.1	< 0.1
W	240	5.2	< 0.14
Ta	21	0.16*	1.6*
Hf	75	< 0.15	< 0.15
Lu	< 0.1	< 0.1	< 0.1
Yb	0.33	< 0.24	< 0.33
Tm	< 0.1	< 0.1	< 0.1
Er	0.36	< 0.16	< 0.16
Ho	< 7.1	0.11	0.57
Dy	0.44	0.37	1.1
Tb	< 0.1	< 0.1	< 0.1
Gd	3.1	0.44	1.5
Eu	< 7.2	0.22	0.4
Sm	0.48	0.26	< 0.23
Nd	1.0	5.2	10
Pr	0.69	6.1	16
Ce	3.6	7.8	18
La	Maj.	Maj.	Maj.
Ba	59	< 0.27	< 0.27
Cs	0.23	< 0.1	< 0.1
I	< 0.1	< 0.1	< 0.1
Te	420	< 0.15	< 0.46
Sb	10 ⁴	< 0.1	< 0.49
Sn	110	0.19	< 0.11
In	1100	< 0.1	0.10
Ca	0.23	14	0.27
Ag	2.6	< 0.1	0.78
Pd	< 0.1	< 0.1	< 0.1
Rh	< 0.1	< 0.1	< 0.1

Table VII (cont.)

Element	As Received	1 Pass	2 Pass
		Zone Refined	Zone Refined
Ru	< 0.1	< 0.1	< 0.1
Mo	9.2	0.69	0.13
Nb	3.2	< 0.1	< 0.1
Zr	20	4.0	< 0.1
Y	0.15	< 0.1	0.15
Sr	200	< 0.1	< 0.1
Rb	2.7	< 0.1	< 0.1
Br	0.11	< 0.1	0.22
Se	1.6	< 0.1	0.11
As	86	< 0.1	0.10
Ge	46	0.14	0.14
Ga	41	0.88	< 0.1
Zn	0.16	2.7	0.27
Cu	85	0.16	0.18
Ni	190	3.1	2.6
Co	680	3.4	0.68
Fe	1300	21	0.70
Mn	130	< 0.63	0.19
Ca	1300	0.35	0.71
V	5.8	7	< 0.1
Ti	200	7.6	0.32
Sc	28	0.22	< 0.1
Ca	330	0.24	0.14
K	230	0.20	< 0.1
Cl	53	53	19
S	180	14	7.9
P	150	0.71	0.36
Si	> 10 ⁴	3.0	7.1
Al	> 1900	< 9.3	3.1
Mg	2800	0.28	0.26
Na	79	< 53	< 0.1
F	4.4	0.10	0.10
B	Maj.	Maj.	Maj.
Be	< 0.1	< 0.1	< 0.1
Li	< 0.1	< 0.1	< 0.1

*Source contamination during analysis
 NR - Not Reported

TABLE VIII
 CARBON AND OXYGEN IMPURITY LEVELS IN PPM BY WEIGHT
 IN VARIOUS RB_6 MATERIALS

Material	Carbon	Oxygen
$LaB_{6.2}$ (Sintered Material) *	2,160	13,100
$LaB_{6.2}$ (2-Pass Zone Melt) *	40	240
CeB_6 (Sintered Material) **	950	7,900
PrB_6 (Sintered Material) **	1,410	28,800

* MRC Material

** CERAC Material

TABLE IX
 BULK PROPERTIES OF LaB_6 and $LaBO_3$

<u>Material</u>	<u>Molecular Weight</u>	<u>Theoretical Density</u>	<u>Crystal Structure</u>
LaB_6	203.7 g/mol	4.71 g/cm ³	Cubic
$LaBO_3$	197.7 g/mol	5.31 g/cm ³	Orthorhombic (Aragonite)

in the zone refined samples were so low, they were attributed to surface oxygen.

The samples we have studied exhibit much higher oxygen concentrations, which clearly cannot be attributed to surface adsorption alone. We believe this oxygen is combined in a ternary second phase material in the bulk. Using the values in Table IX and assuming that all the bulk oxygen (240 ppmw) is combined as LaBO_3 , we calculate a bulk density of 0.1 wt % (0.1 mol %) or 0.09 vol % of second phase material in our zone refined samples. If we further assume that all observed defects in fracture surfaces are in fact LaBO_3 , and that the surface concentration observed is uniform throughout the bulk, then we arrive at an actual, measured bulk concentration of 0.02 to 0.09 vol % of the second phase material, in excellent agreement with the value calculated from the bulk oxygen concentration.

The measured defect density observed in LaB_6 single crystals prepared by the aluminum flux method¹ is $\sim 10^3$ times lower than the defect density in zone refined crystals. This observation is consistent with our assumption that an oxygen-rich second phase is associated with the observed defects, since one would expect the highly reactive aluminum flux to efficiently scavenge available oxygen from flux-prepared samples. Thus, a much lower defect density would be anticipated in these samples, as has been observed.

It is clearly undesirable to have inclusions of second phase material in LaB_6 cathodes, since they contribute to surface nonuniformity and may affect electron emission spatial distributions. Thus, careful control of oxygen contamination in the hot pressed starting material appears important. As can be seen from Table VIII, the level of oxygen present in commercially available hot pressed RB_6 materials is generally quite high. It is clear that the allowable oxygen concentration in the hot pressed material is a parameter which must be specified in order to optimize cathode efficiency.

2. Task II: Single Crystal Emitter Structure Fabrication

(a) Field Emitter Structures

In order to obtain field emitter cathode structures a sharp point (radius $\lesssim 0.3 \mu\text{m}$) must be formed on a single crystal blank of the RB_6 material and the blank must be attached to a resistively heatable filament.

The RB_6 materials are very reactive with most refractory elements and compounds except C, Re and TaC. Thus the method of attachment and materials used must be carefully chosen.

A successful mount has been employed using a mechanical press fit of a LaB_6 crystal to Re. Field emitter structures were quickly and conveniently prepared by mounting a rectangular or cylindrical shaped single crystal blank on a flat rhenium ribbon (0.001" x 0.010") and fixed to it by means of a spot-welded rhenium strap of the same thickness and width (see Figure 7). In addition, a binder consisting of an aqueous slurry of TaC was inserted between the emitter and rhenium support strap. Subsequent heating in vacuum at ~ 1800 K allowed the binder to sinter and form a durable mechanical and thermal bond between the emitter crystal and rhenium ribbon. The emitter points were obtained by electrochemical etching in a 50% methanol/NaOCl solution at 1.5 V. The power requirements to resistively heat the emitter shown in Figure 7 to ~ 1800 K are less than 3 watts.

Highly magnified photomicrographs of a LaB_6 emitter are shown in Figure 8 for three rotational orientations of the emitter. The gross diameter of the emitter end form is about 1000 Å.

In this case the emitter blank was a (100) oriented crystal of LaB_6 fabricated by the molten aluminum flux method¹ which yields small single crystal needles of LaB_6 suitable for fabricating field emitters. Similar shaped emitters have been fabricated from the single crystal needles of CeB_6 and SrB_6 .¹⁶

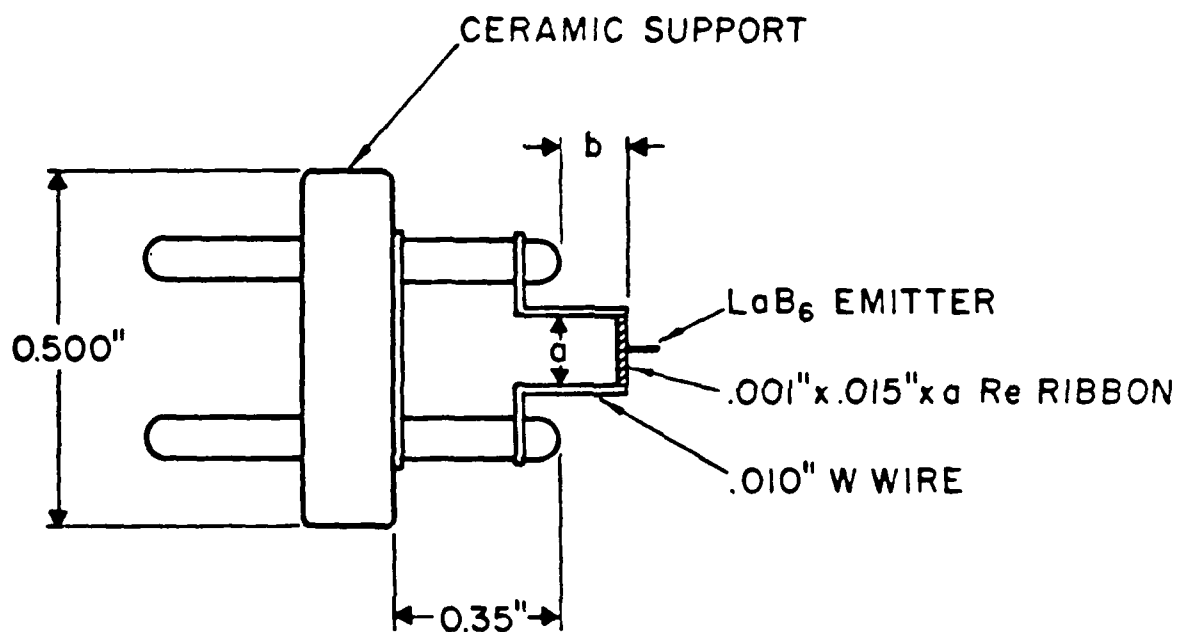
(b) Thermionic Emitter Structures

Larger radius and cone angle emitters suitable for thermionic emission have been constructed by use of mechanical grinding techniques. Typically LaB_6 can be conveniently ground using a 3000 mesh diamond wheel. For a smooth surface finish, a final polish using a 14,000 mesh aluminum oxide diamond material is employed.

The grinding step is very rapid, taking 3-4 minutes to fabricate a pointed end on an initially flat single crystal rod of 1 mm diameter. If a truncated cone is required, that step is performed next using the 3000 mesh diamond wheel. Final polishing takes about 20 minutes.

Both grinding and polishing are carried out on a standard lapidary machine, with motor driven grinding table and motor driven head which can

LaB₆ EMITTER STRUCTURE



DIMENSIONS: a - 0.18'' to 0.25''
b - 0.1'' to 0.5''

Figure 7. Diagram of field emitter and resistively heatable filament support structure used for single crystal material of LaB₆.

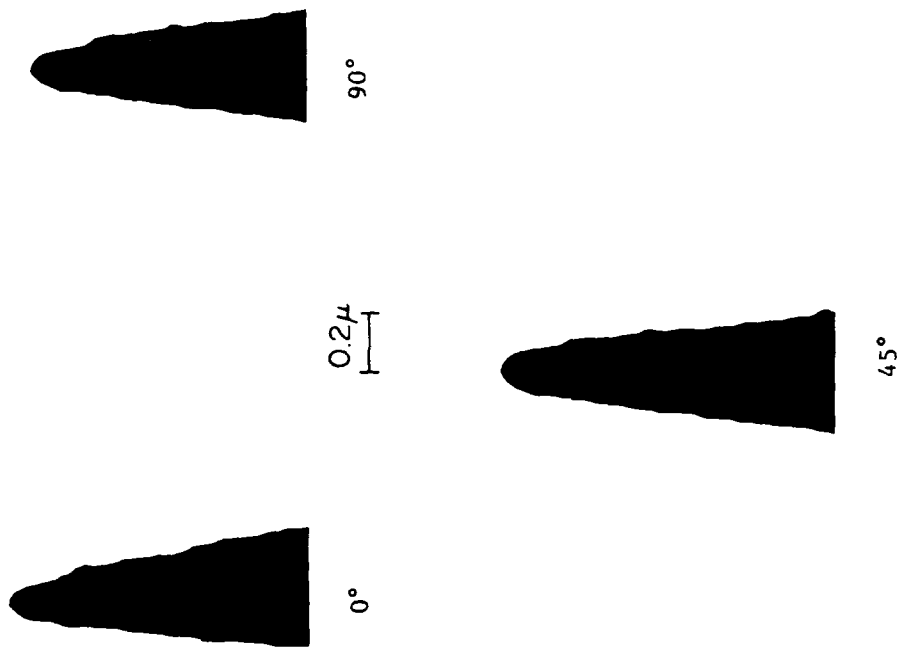


Figure 8. Micrograph profiles of an LaB₆ field emitter which has been operated in a TF mode.

be tilted to any desired angle with respect to the table normal. The sample-holding head assembly has been modified to use high precision bearings in order to obtain very reproducible results.

Typical results are shown in Figure 9 where LaB₆ single crystal emitters of both pointed cone and truncated cone configurations are illustrated. Figure 10(b) shows the overall mounting configuration where the LaB₆ crystal is contained in a rhenium cup which, in turn, is mounted on resistively heatable tungsten filament supports. This structure has operated successfully at 1800 K for several hundred hours. A typical heating characteristic curve for the Figure 10(b) structure is shown in Figure 11. One can achieve an operating temperature of 1800 K with ~ 6 W of electrical power.

A second type of mounting system used successfully for thermionic cathodes is shown in Figure 10(a). In this type of mount, the cathode is clamped between grooved graphite blocks which are in turn held between heavy Mo or W supports.¹⁷ Current passed through the assembly causes ohmic heating of the graphite, which heats the cathode by conduction. The heavy supports are good heat sinks and never become hot enough to lose any material through vaporization. Thus, there is no possibility of foreign material evaporating onto the cathode surface, making the design particularly suited to long lifetime applications, as will be discussed later.

3. Task III: Thermal and Field Emission Characterization

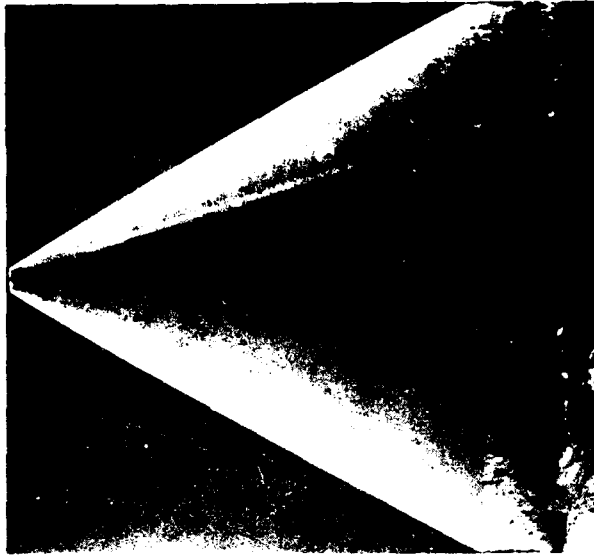
(a) Background

Thermionic measurements were carried out in an ULTEK TBK 250 liter/sec ultra-high vacuum system, which was also used in experiments discussed under Task IV. Ultimate pressure was 2×10^{-10} torr, so that surface contamination could be minimized. Emitted current density was measured using an outgassable, guard plate-collector assembly, with a precisely known collector area. Temperature measurements were made pyrometrically on the LaB₆ crystal using emissivity data of Storms¹⁸ to correct for the non-black body arrangement. Heating was accomplished by resistive heating of the tungsten filament support wires spot welded to the sleeve.

It should be pointed out that due to the smallness of some crystals, thermionic diode measurements could not easily be carried out with a guarded

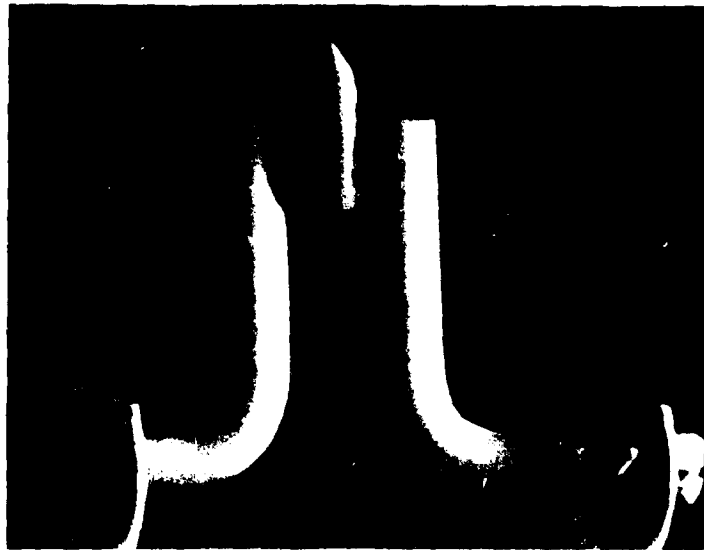


(a) 100 μm

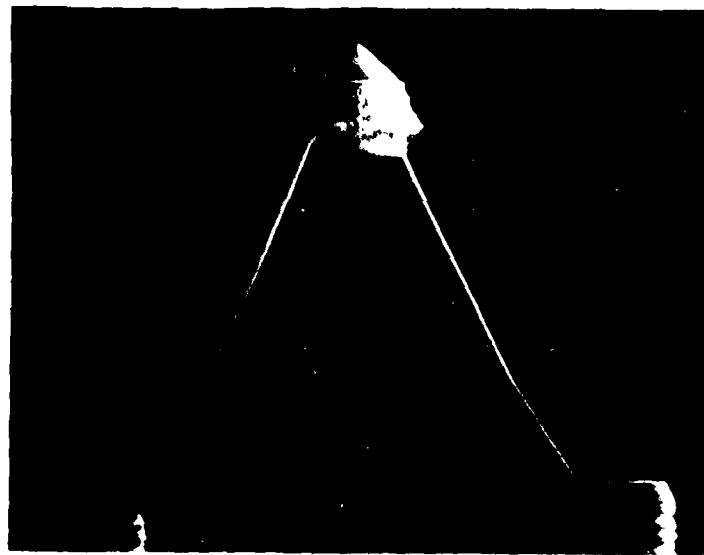


(b) 100 μm

Figure 9. Photos of (a) 90° cone angle pointed LaB₆ emitter and (b) 60° cone angle emitter with a 40 μm flat on end.



(a) 1mm



(b) 1mm

Figure 10. (a) and (b) are micrographs of the output of the electronic emitter. (a) shows the output of the emitter at the first resonance. (b) shows the output of the emitter at the second resonance.

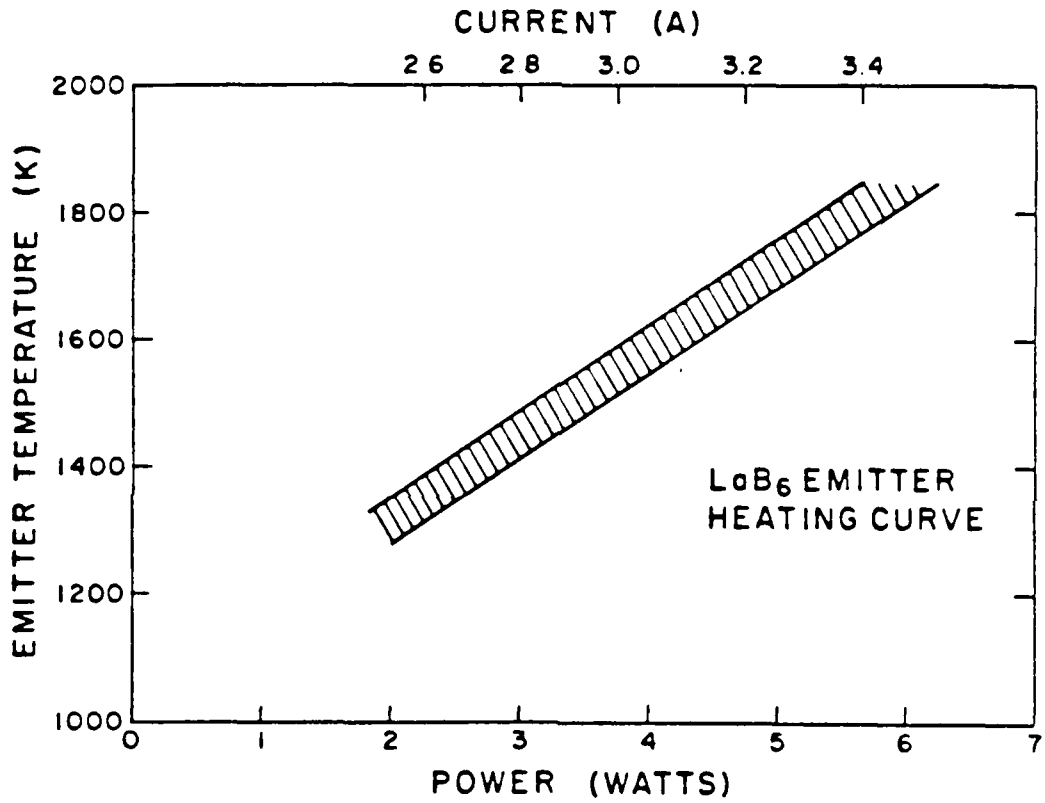


Figure 11. Emitter temperature vs heating current and power is given for an LaB₆ thermionic emitter constructed according to Figure 10(b).

collector structure. Instead, because of the low work function of the crystal in comparison with the substrate support structure and the elimination of edge effects by the crystal geometry and mounting technique, we assumed that the emitting area was given by the geometric area of the exposed crystal face.

Thermionic emission distribution studies and life test measurements were performed in a separate chamber, equipped with a phosphor screen for projection thermionic microscopy. This system allowed measurement of I-V characteristics and direct observation of the emission distribution. Ultimate pressure of the system was less than 1×10^{-9} torr, and life tests and emission measurements were made with $P \leq 5 \times 10^{-9}$ torr.

A third system was used for field emission/field ionization measurements. This chamber was equipped with a sample cooling facility, gas inlet manifold and image intensifier, so that field ionization patterns could be studied at high spatial resolution.

(b) Thermionic Work Functions

The thermionic method of work function measurement involves application of the well known Richardson equation

$$J = (1 - R) 120 T^2 \exp(-\phi/kT) \quad (1)$$

where J is the emitted electron current density in A/cm^2 and R is the reflection coefficient. However, in earlier studies of the RB_6 compounds the Richardson plots are not always linear, indicating either an inadequacy of the free electron model on which Eq.(1) is based or a nonlinear temperature dependent work function.

An example of this problem can be seen in Table X where the existing published values of LaB_6 single crystal thermionic work functions are tabulated. The values of work function for the (100) face, which have been measured most extensively, range from 2.4 to ~ 3.0 eV. Part of the problem is that a range of values of Richardson work functions can be obtained depending upon the temperature interval of the measurements. Surface stoichiometry and bulk impurity levels also have an effect upon emitted current density. This effect is particularly acute for LaB_6 because of the extraordinarily low bulk diffusion rates and the narrow range of stoichiometry over which the LaB_6 phase is stable.¹⁹

TABLE X
 SUMMARY OF EFFECTIVE THERMIONIC WORK FUNCTION
 VALUES OF VARIOUS CRYSTAL PLANES OF LaB₆

Plane	ϕ (eV)	P (torr)*	Ref.
001	2.52 ± .05	5 ± 10 ⁻¹⁰	(This Study)
001	2.47 ± .06	5 ± 10 ⁻¹⁰	17
001	2.4 ± .2	< 2 ± 10 ⁻⁷	18
001	2.8	2 to 7 ± 10 ⁻⁸	19
001	≥ 3	5 ± 10 ⁻⁷	20
011	2.64 ± .05	9 ± 10 ⁻¹⁰	(This Study)
011	2.5	5 ± 10 ⁻⁷	20
011	2.6	2 to 7 ± 10 ⁻⁸	19
011	2.74	< 1 ± 10 ⁻⁹	21
111	2.90 ± .05	5 ± 10 ⁻¹⁰	(This Study)
111	3.4	2 to 7 ± 10 ⁻⁸	19
123	2.3 ± .2	2 ± 10 ⁻⁷	18
346	2.41 ± .05	5 ± 10 ⁻¹⁰	(This Study)

*Base pressure during measurement.

In view of these problems, we treated the data somewhat differently and instead measured an "effective" work function ϕ_e at each temperature according to

$$\phi_e = -kT \ln(J/120 T^2) \quad (2)$$

where we assume $R = 0$. A value of ϕ_e was determined at each of several temperatures, obviating the problem of the temperature dependence of ϕ .

The effective work function values measured according to Eq.(2) at several values of diode voltage were extrapolated to zero field ($V = 0$) by plotting ϕ_e vs $V^{1/2}$. These results are displayed in Figure 12 as a function of temperature for each of the $\text{LaB}_{5.86}$ crystal faces. Most of the crystal faces exhibited an increasing, but not always linear, value of ϕ_e with T . It is these nonlinear ϕ_e vs T relationships which render work function values obtained from Richardson plots ambiguous. Figure 13 displays the zero field $J(T)$ data of Figure 12 plotted according to the Richardson Eq.(1) and clearly shows the ambiguity in work function values depending upon the temperature range over which the slope is measured.

A striking result is the difference in the value and temperature dependence of the two runs obtained from the $\text{LaB}_{5.86}(100)$ crystal (Figure 12(b)). The upper and lower curves of Figure 12(b) correlate respectively with the (100)(a) and (100)(b) AES results discussed under Task IV. A significantly lower ϕ_e value is associated with the surface structure exhibiting the lower B(179)/La(78) ratio. The fact that considerable heating of the LaB_6 single crystals must take place before reproducible work function values can be obtained is an observation made in other similar studies.²⁰ Presumably the surface composition and work function which result after long-term heating at $T \gtrsim 1800$ K represent a surface phase whose stoichiometry has approached a steady state composition near the congruently vaporizing composition.¹⁹ Detailed measurements of surface composition will be discussed under Task IV.

For the low index LaB_6 planes we find that ϕ_e increases in the order (100) < (110) < (111). Interestingly, the latter order is also the order of decreasing La surface atom density for unreconstructed surfaces. The $\log J$ vs $1/T$ plots, given in Figure 13 for the various LaB_6 crystals, clearly

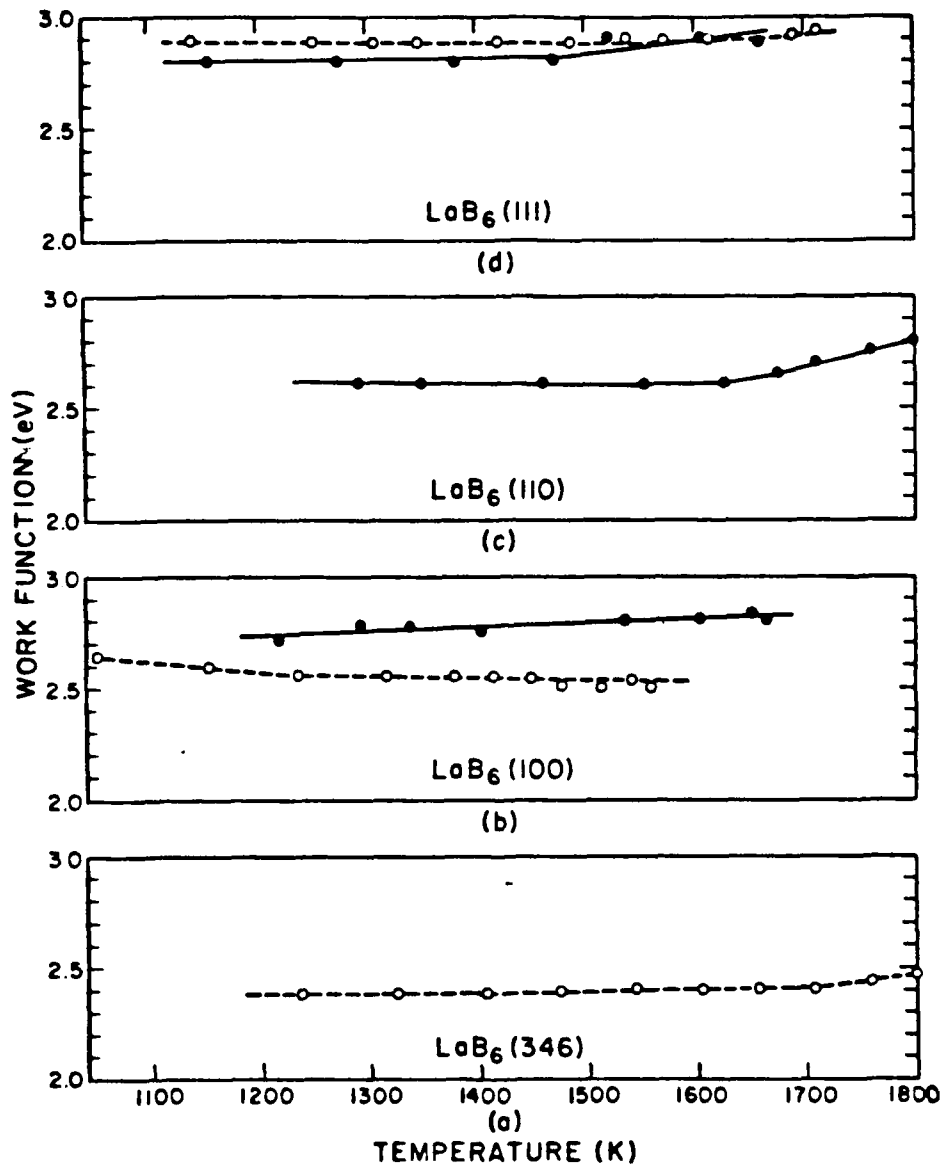


Figure 12. Zero field thermionic work function vs. temperature plots for LaB_6 single crystals; \bullet initial and \circ final curves obtained from the indicated planes.

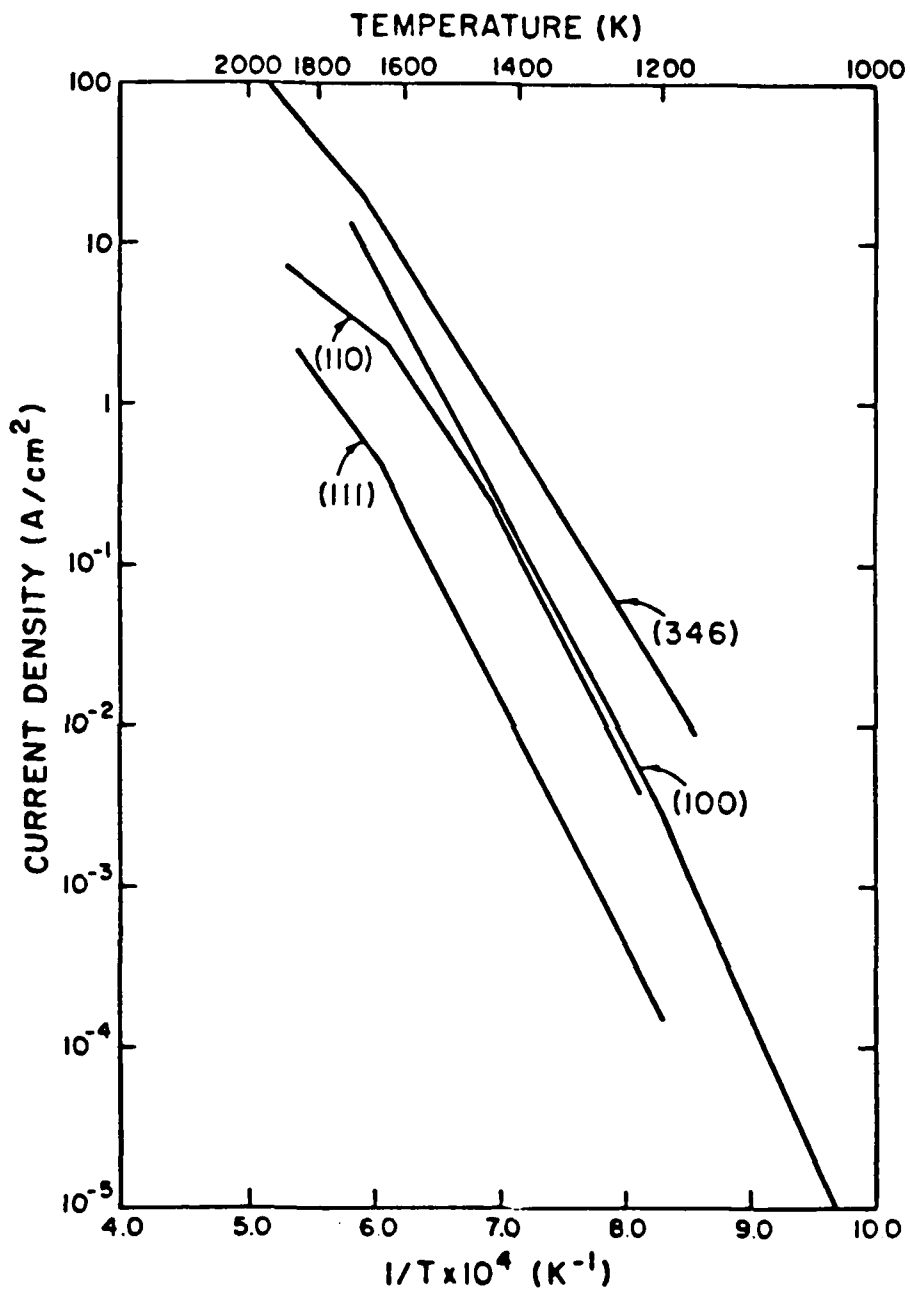


Figure 13. Comparison of emitted current density behavior of various LaB_{5.86} crystal faces.

show the superior emission properties of the (100) and (346) in contrast to the low values of emitted current for the (111) face. Significant departures from the Richardson equation are noted for most crystal faces, underscoring the care that must be exercised in extrapolating low temperature $\log J$ vs $1/T$ data to higher temperatures. Figure 14 shows emission current data for the (100) faces of $\text{PrB}_{5.87}$, $\text{CeB}_{6.2}$ and $\text{LaB}_{6.09}$ and for the (211) face of $\text{LaB}_{6.09}$. Nonlinear behavior is also evident in this figure.

Table XI summarizes the ϕ_e values obtained at 1600-1700 K for all of the RB_6 crystals studied. The results show a general decrease in ϕ_e with decreasing B/R surface stoichiometry for the low index faces. In addition, the ϕ_e measurements for the (110) and (100) faces of the $\text{LaB}_{5.74}$ crystals are consistently larger than for the $\text{LaB}_{5.86}$ crystals. The $\text{LaB}_{6.09}(100)$ shows a work function value approximately equal to that of the $\text{LaB}_{5.74}(100)$ crystal, but higher than that observed for $\text{LaB}_{5.86}(100)$. This result is not unexpected since a work function minimum near the CVC ($\text{B/La} \sim 6.04$ at 1700 K) was anticipated. Thus, the $\text{LaB}_{6.09}$ sample is apparently La poor while the $\text{LaB}_{5.74}$ sample is La rich compared to the stoichiometry yielding minimum work function.

Comparison of the work functions of the different RB_6 compounds shows LaB_6 to be the lowest in every case where the same crystal faces can be compared. Unfortunately, a well-defined range of stoichiometries is available only for LaB_6 , so variations of work function with stoichiometry in the other RB_6 compounds cannot be considered in the comparison.

Since LaB_6 shows a clear work function superiority of the (100) among stable, low index planes, we expect the same should hold true in the other RB_6 compounds. This expectation seems to be upheld for the CeB_6 case, at least when the (100) and (111) faces are compared.

The data for the $\text{LaB}_{6.09}(211)$ surface represent another high index plane. The original intent was to study the (210) face because of a recently reported observation of a photoelectron work function of 2.2 eV for that surface.²¹ The hope was that a correspondingly low ϕ_e would be measured. A "(210)" surface was thus prepared, and initial Laué measurements were interpreted to indicate, indeed, a (210) surface, within 2° or so. However, due to the large incident x-ray beam used the sample could not be tilted enough for the symmetry of nearby major planes, (100) and

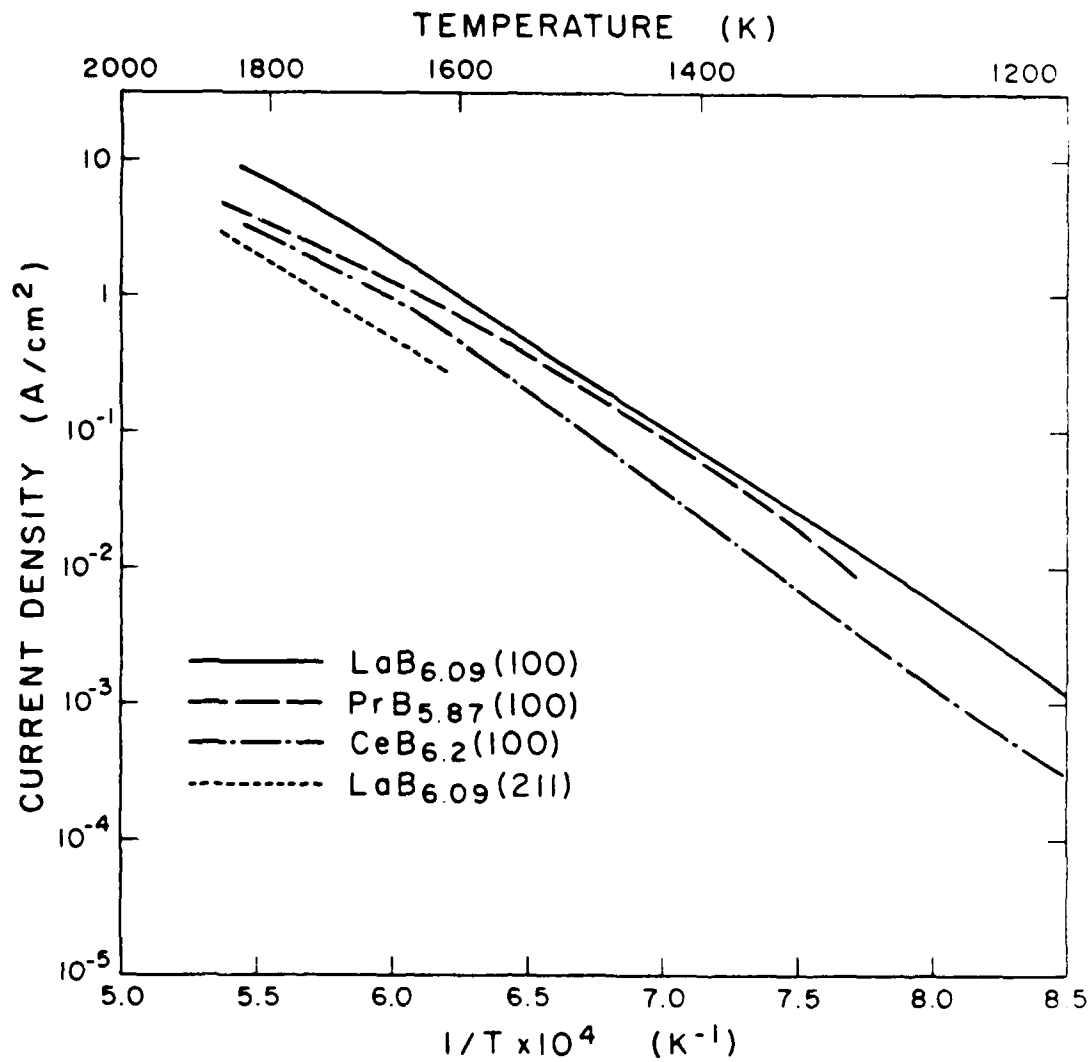


Figure 14. Comparison of emitted current density behavior of (100) planes of RB₆ compounds and the (211) LaB_{6.09} surface.

TABLE XI
 SUMMARY OF EFFECTIVE THERMIONIC WORK FUNCTION
 MEASUREMENTS ON RB_6 SINGLE CRYSTAL SURFACES
 (T = 1600-1700 K)

Material	Precise B/R Ratio	Crystal Face	ϕ_e (eV) [†]
LaB_6	5.86	(100)	2.52 ± 0.05
	5.86	(110)	2.64 ± 0.05
	5.86	(111)	2.90 ± 0.05
	5.86	(346)	2.41 ± 0.05
	5.74	(100)	2.71 ± 0.05
	5.74	(110)	2.75 ± 0.05
	5.74	(321)	2.80 ± 0.05
	6.09	(100) within 2°	2.69 ± 0.05
	6.09	(211) within 2.2°	2.92 ± 0.05
CeB_6	*	(100)	2.90 ± 0.05
	6.2	(100) within 2.2°	2.81 ± 0.05
	*	(111)	3.00 ± 0.05
PrB_6	5.87	(100) within 1.8°	2.74 ± 0.05

*Stoichiometry not Determined

[†]Pulsed Measurement

(110), to be verified. Nevertheless, the surface measurements were performed. In detailed Laué studies, at the very end of the project, a highly collimated x-ray beam was used, allowing tilting of the sample up to 30° without large increases in scattered x-ray background. We found that our "(210)" plane was actually on the (100) - (111) zone line, and was in fact a (211) plane, within 2.2° . Nevertheless, the results are reported here for completeness.

(c) Thermionic Emission Distributions

The tube for analysis of the spatial emission distributions of pointed thermionic cathodes is shown in Figure 15. It consists of the emitter structure, Wehnelt electrode, a ring electrode and a fluorescent screen, all within an ultrahigh vacuum envelope. Typically, the ring electrode and screen were operated at 1 to 2 kV and the Wehnelt electrode was biased both positively and negatively with respect to the grounded emitter. This simple design allows rapid visual characterization of the emitted current variation from the tip and conical sides of the cathode surface. Variation of the emission distribution with operating time, caused by faceting of the cathode surface, may also be studied with this device. Since there is no provision for precise current density measurements from well defined areas of the cathode these studies provide only qualitative emission distribution results. However, quantitative total current measurements may be made.

Electron emission distributions from both pointed cone and truncated cone LaB_6 cathodes have been investigated at various stages of life. Figures 16 and 17 show emission distributions from a 90° cone, $\langle 100 \rangle$ oriented cathode (tip radius initially $\sim 5 \mu\text{m}$) after a few hours operation and after ~ 380 hours operation at 1700-1800 K, respectively. These patterns correspond to points A-F in the I-V plot of Figure 18.

At large positive Wehnelt bias, the patterns consist essentially of a bright ring of emission and weak emission from the central (100) region. As the Wehnelt bias is reduced, the ring of emission from the cone shank of the emitter is brought into the center of the pattern. As the Wehnelt bias is driven negative, the pattern shrinks and becomes brighter as the cone shank emission is compressed (Figure 16, for example) and crosses over (Figure 16(E)). Emission is eventually cut off, first from the cone shank

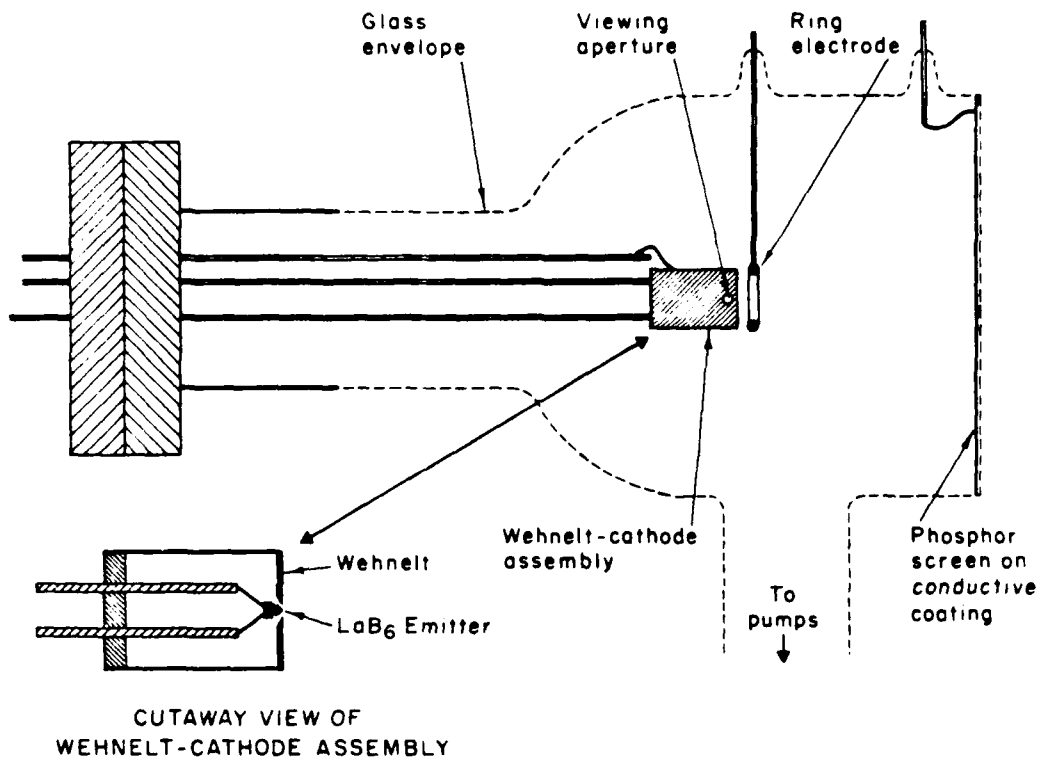
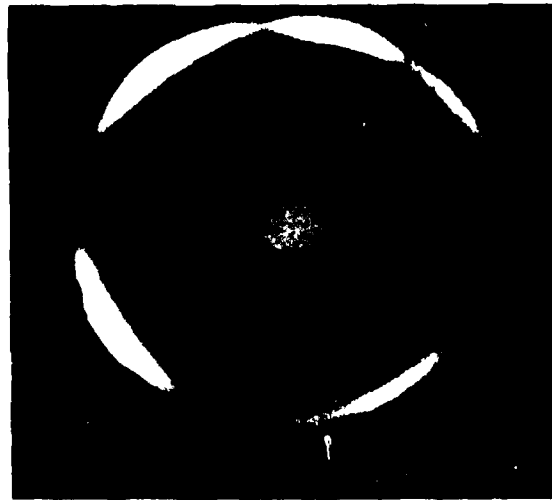


Figure 15. Schematic drawing of display system used for studies of thermionic emission distributions.



(d) $V_w = 100$ volts

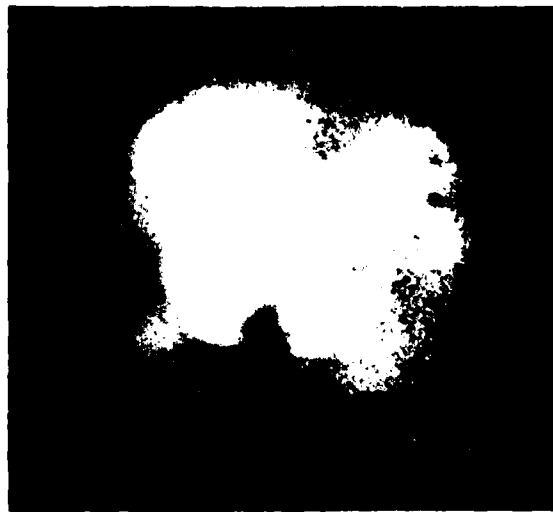


(b) $V_w = 20$ volts

Figure 16. Thermionic emission from a 40° pointed LaB₆ (100) cathode, emitting from a circular illuminated Wehnelt bias voltage V_w .

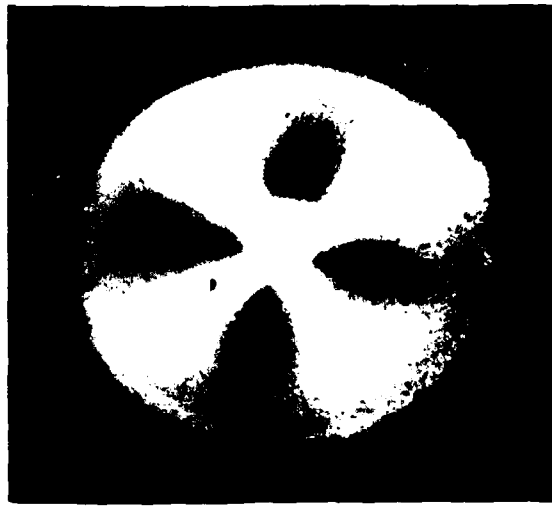


(c) $V_w = 15$ volts

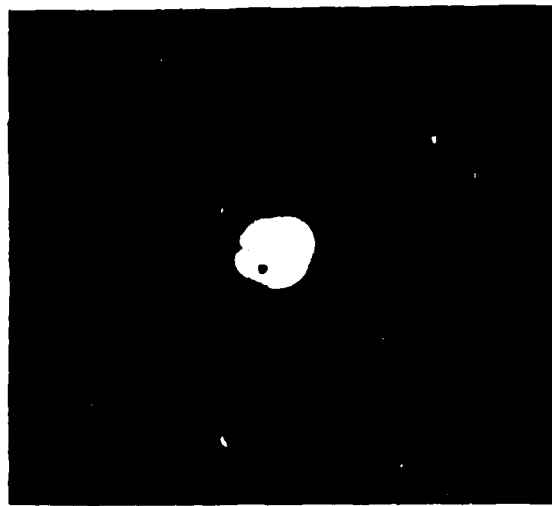


(d) $V_w = 5$ volts

Figure 16. (continued)



(e) $V_w = 1$ volt

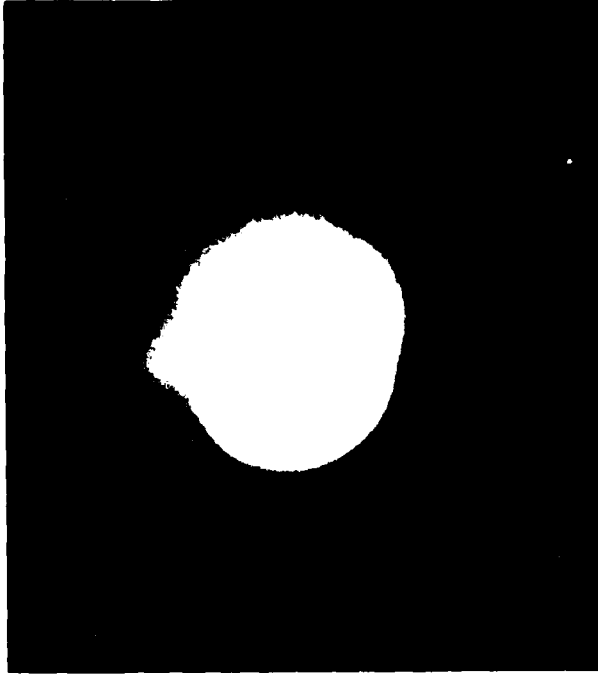


(f) $V_w = -15$ volts

Figure 16. (continued)

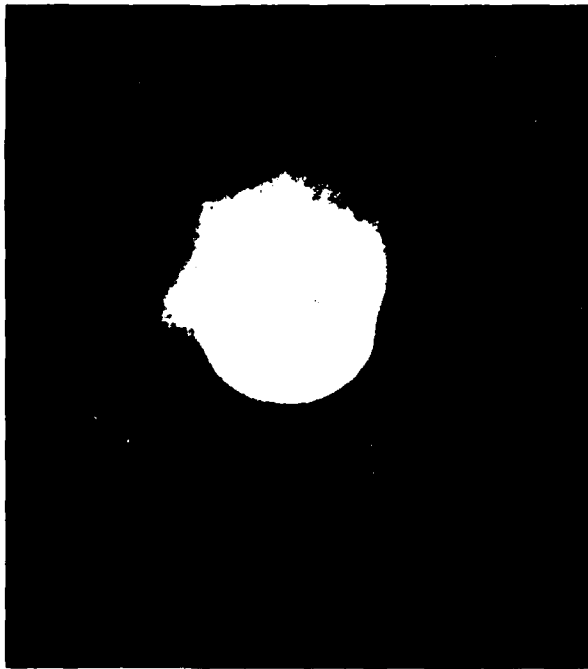


A: $V_W = 95.7 \text{ V}$

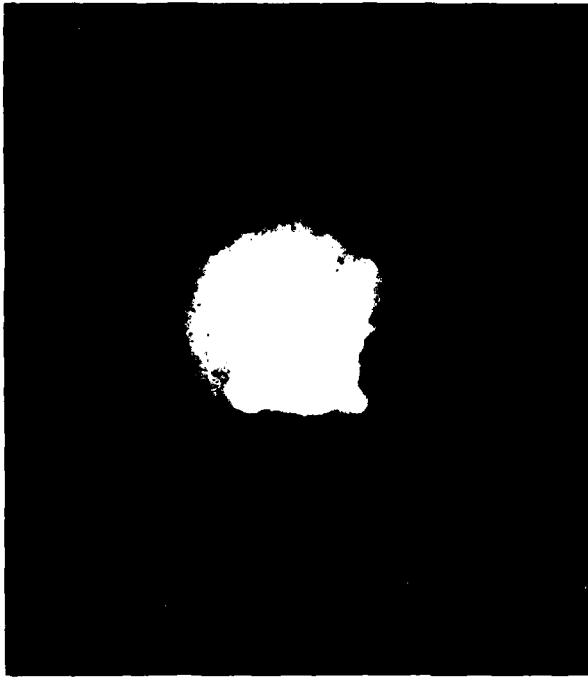


B: $V_W = 18.2 \text{ V}$

Figure 17. Thermionic emission patterns from $\text{LaB}_6(100)$ pointed cathode, 90° cone angle, after 380 hours of life at 1700 K. Patterns were observed at the indicated Wehnelt bias voltages, V_W .

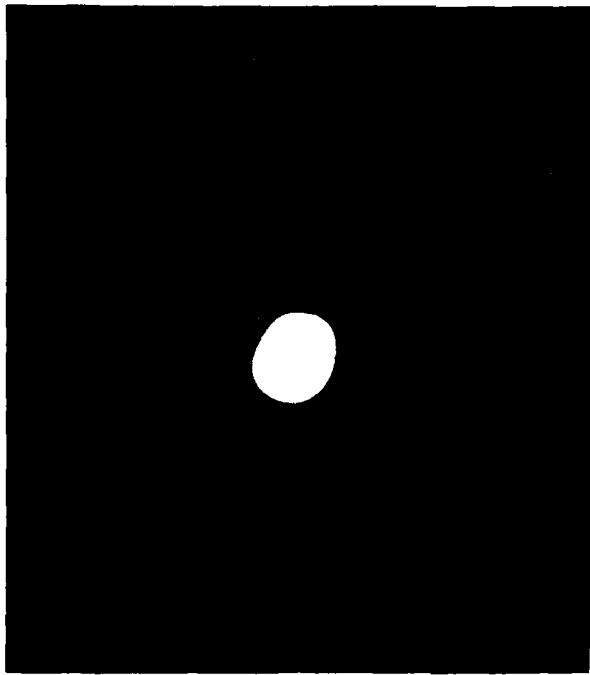


C: $V_W = 14.2 \text{ V}$

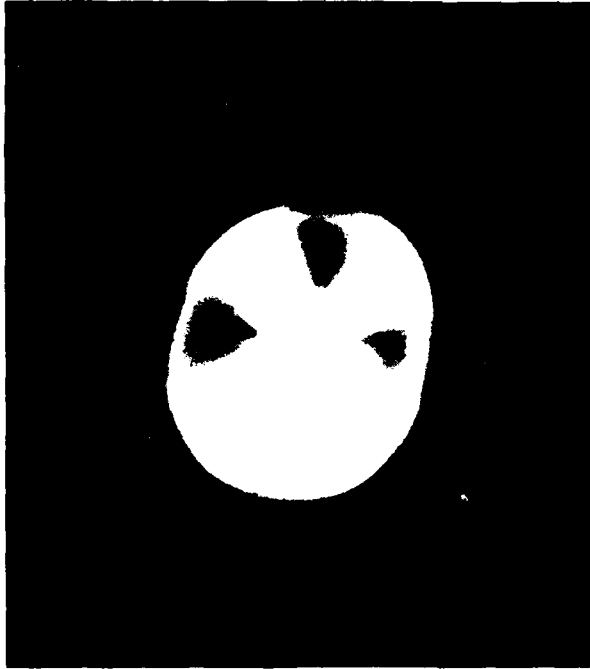


D: $V_W = 5.5 \text{ V}$

Figure 17. (continued)

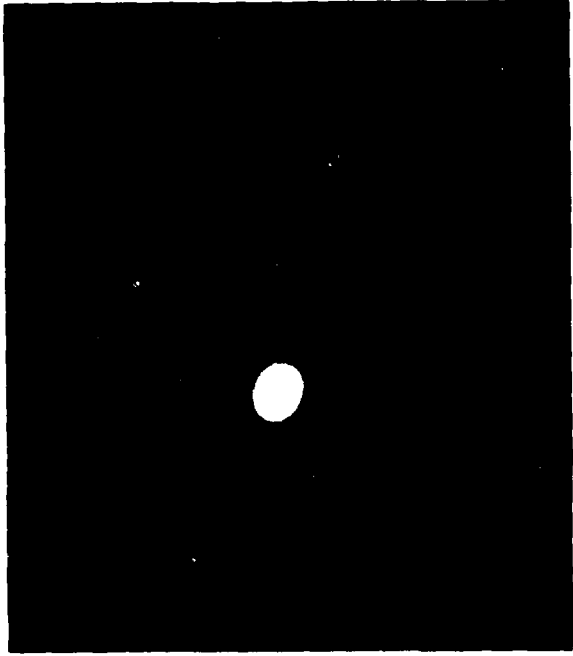


E: $V_W = 0.0 \text{ V}$



F: $V_W = -14.8 \text{ V}$

Figure 17. (continued)



at $V_g = -18.8$ V

Figure 17. (continued)

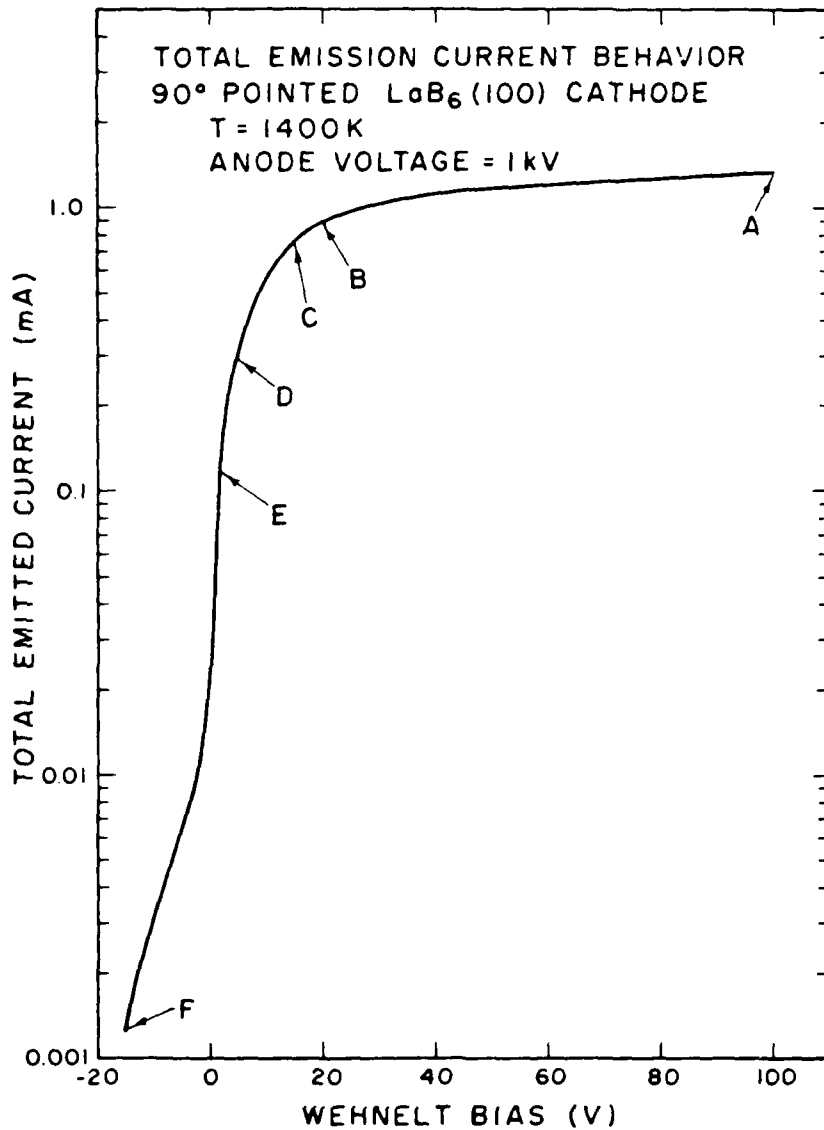


Figure 18. Total emission current I-V characteristic of 90° pointed LaB_6 (100) cathode used in thermionic emission distribution studies. Patterns corresponding to indicated points A-F are shown in Figures 16 and 17.

(Figure 16(F)) and, finally, from the apex itself.

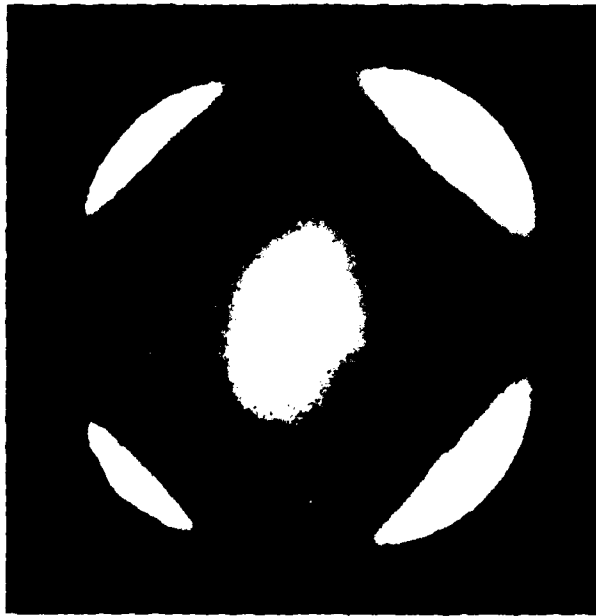
Note the four-fold symmetry characteristics of the (100) orientation of this cathode. Also, note the development of the bright spot at the top center of pattern 16(C). Apparently this random bright spot is caused by emission from a low work function site on the side of the cone, which is ultimately focused into the center of the pattern as the bias is reduced.

Changes which have occurred during the life of the cathode will be discussed under the next section, Task III (d).

Figures 19 and 20 show thermionic emission patterns from a 60° cone, truncated with a 40 μ m diameter, (100) face, after 5 hours and 570 hours of life, respectively, at 1700-1800 K. These patterns also exhibit four-fold symmetry. However, they also show a bright central region (emission from the flat area) near cutoff. This particular property may turn out to be of importance in focused beam applications, and appears to be one of the primary advantages of the truncated cone design.

Figure 21 shows the emitted current collected at the screen, plus a small background current emitted from the side of the cathode through the observation hole in the Wehnelt cap. Thus, this figure represents approximately the current which would be usable in an electron gun assembly. Note the difference between operation near the space-charge regime ($T = 1440$ K). The maximum observed in the 1440 K curve near 0 V bias may be attributable to some peculiar focusing property of the system. Since the field distribution near the truncated cone cathode is not well known, a precise description of this first effect is not yet possible.

Figure 22 shows data taken after 570 hours operation at 1700 K, for four different emitting temperatures. After the life test, off-center emission patterns were observed, so the cathode had to be repositioned in the Wehnelt assembly. The axial position of the cathode was not exactly the same following this procedure, and the end of the cathode protruded slightly, rather than being slightly recessed as in the early-life case. Thus, emission currents in Figure 22 are somewhat higher than would be expected from Figure 21, and the cutoff Wehnelt bias has been shifted to a considerably more negative voltage. We may conclude, however, that the emission characteristics of the truncated cathode are not significantly degraded, and

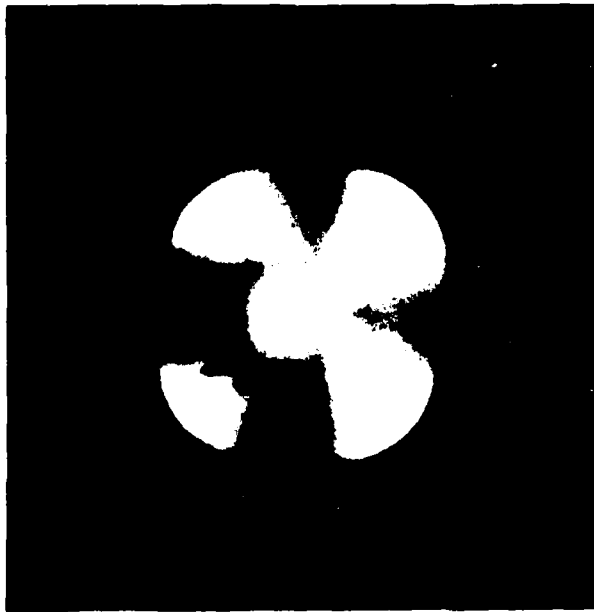


A: $V_W \approx +39.4$ V

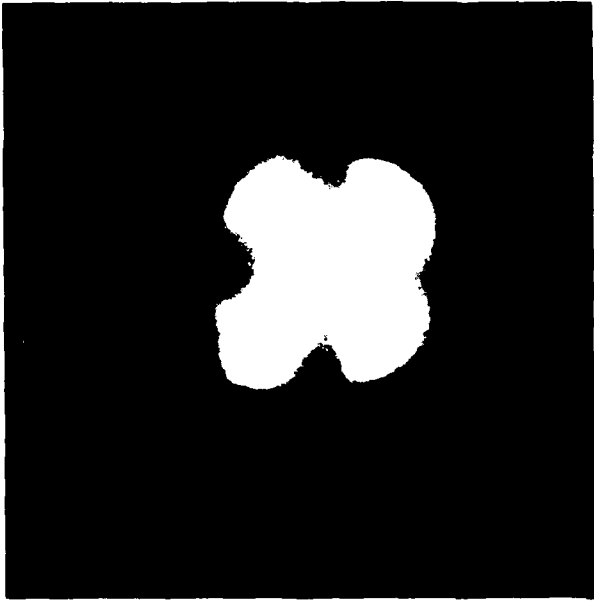


B: $V_W = +25.3$ V

Figure 19. Thermionic emission patterns from $\text{LaB}_6(100)$ truncated cathode, 60° cone angle, after 5 hours of life at 1700 K. Patterns were observed at the indicated Wehnelt bias voltages, V_W .

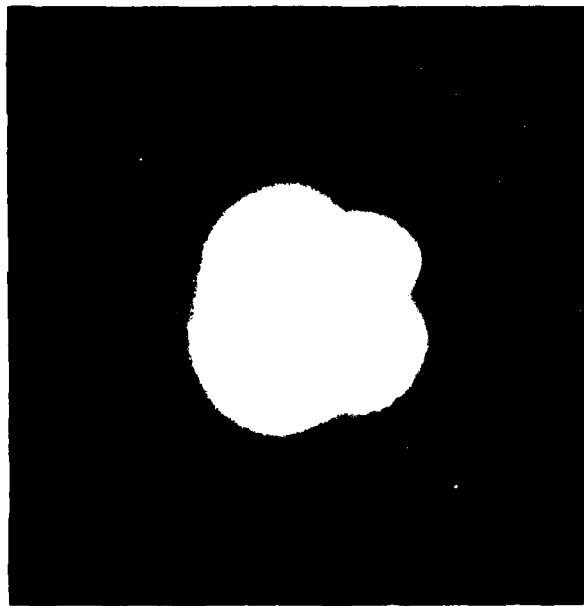


C: $V_W = +15.0$

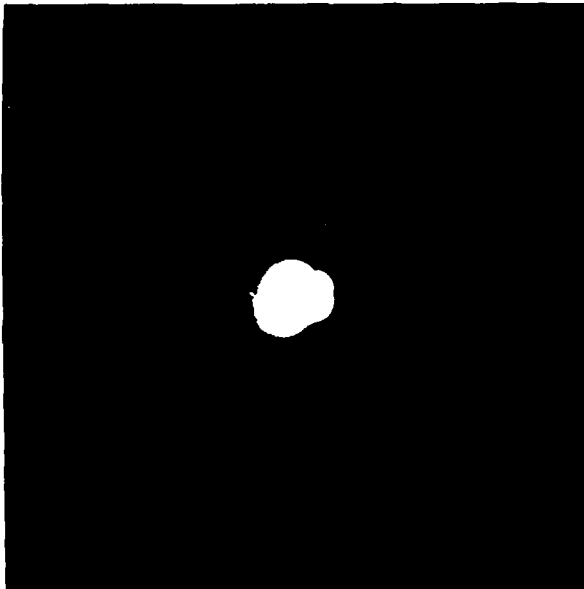


D: $V_W = +6.7$ V

Figure 19. (continued)

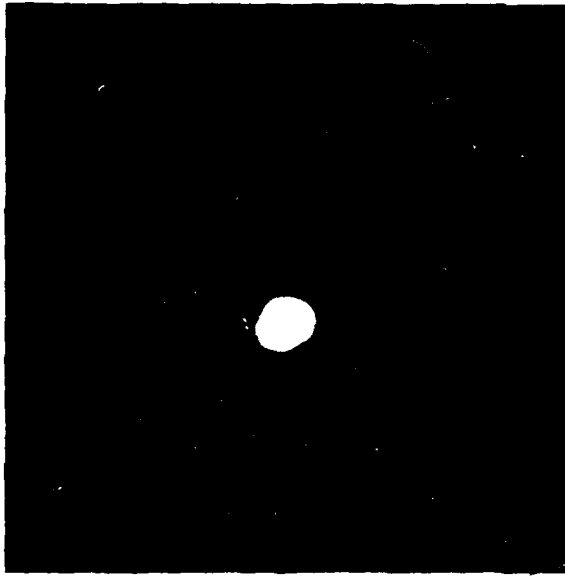


E: $V_W = 0.0 \text{ V}$



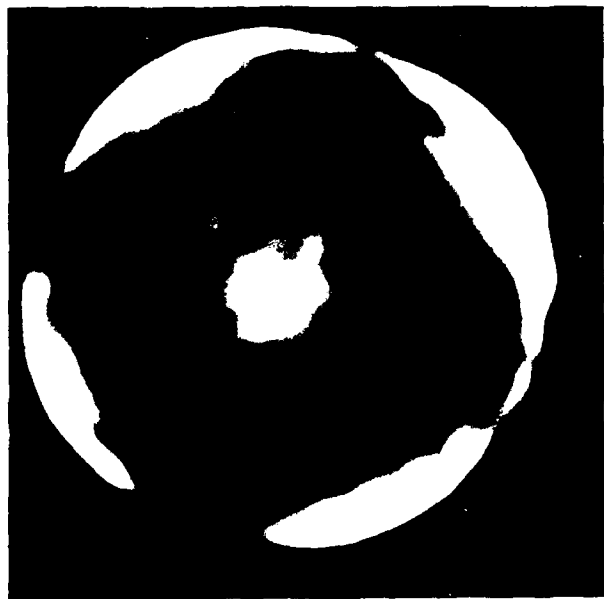
F: $V_W = -15.1 \text{ V}$

Figure 19. (continued)

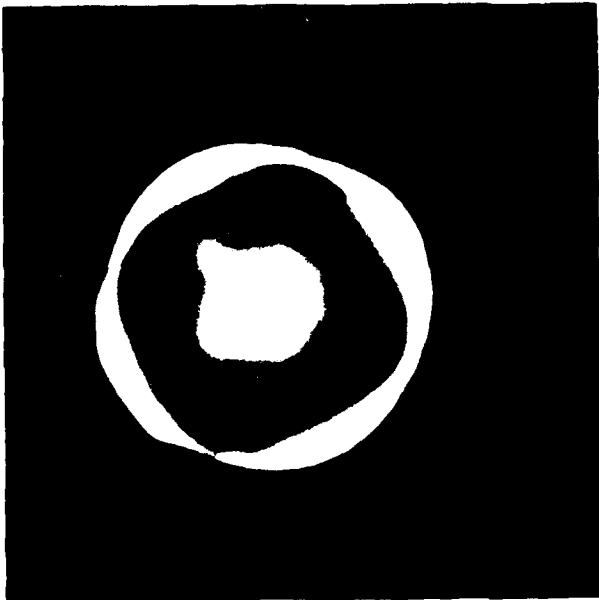


(3) $V_W = -17.6$

Figure 19. (continued)

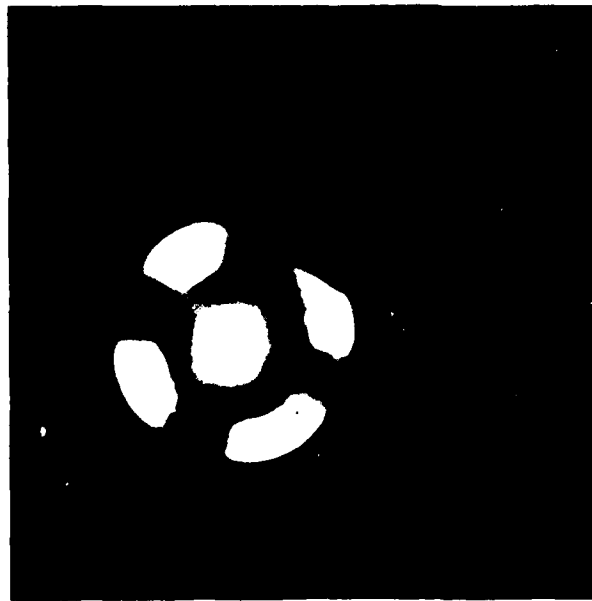


A: $V_W = +130$ V

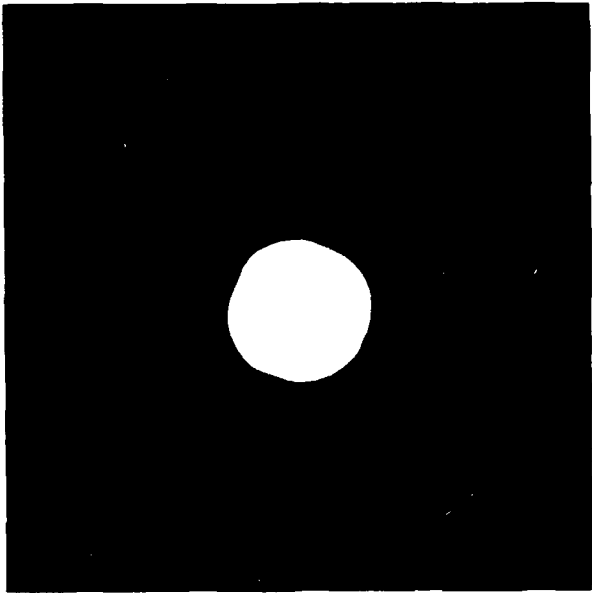


B: $V_W = +56$ V

Figure 20. Thermionic emission patterns from a $\text{LaB}_6(100)$ truncated cathode, 60° cone angle, after ~ 570 hours life at 1700 K. Patterns were observed at the indicated Wehnelt bias voltages, V_W .

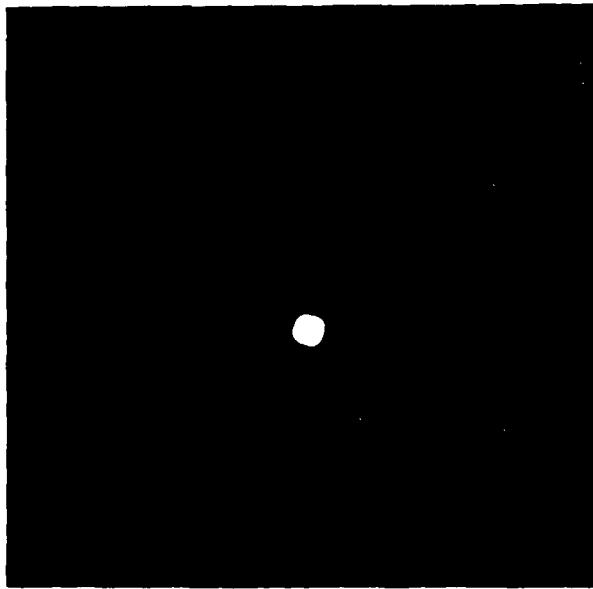


C: $V_W = +19.7 \text{ V}$

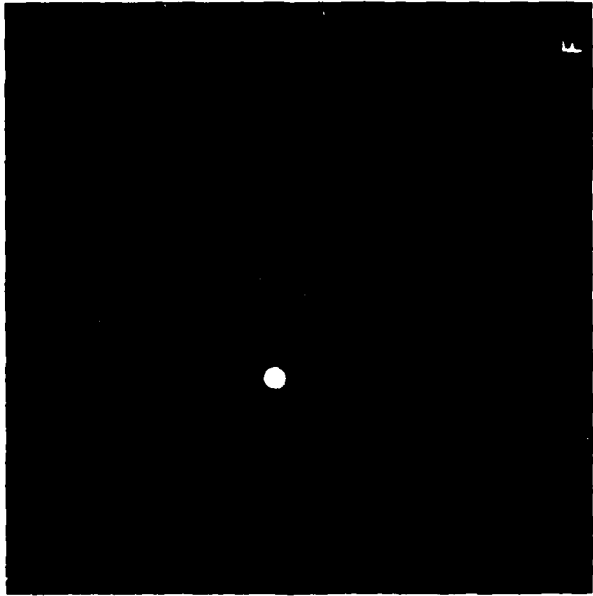


D: $V_W = 0.0$

Figure 20. (continued)



E: $V_W = -23.0$ V



F: $V_W = -26.0$ V

Figure 20. (continued)

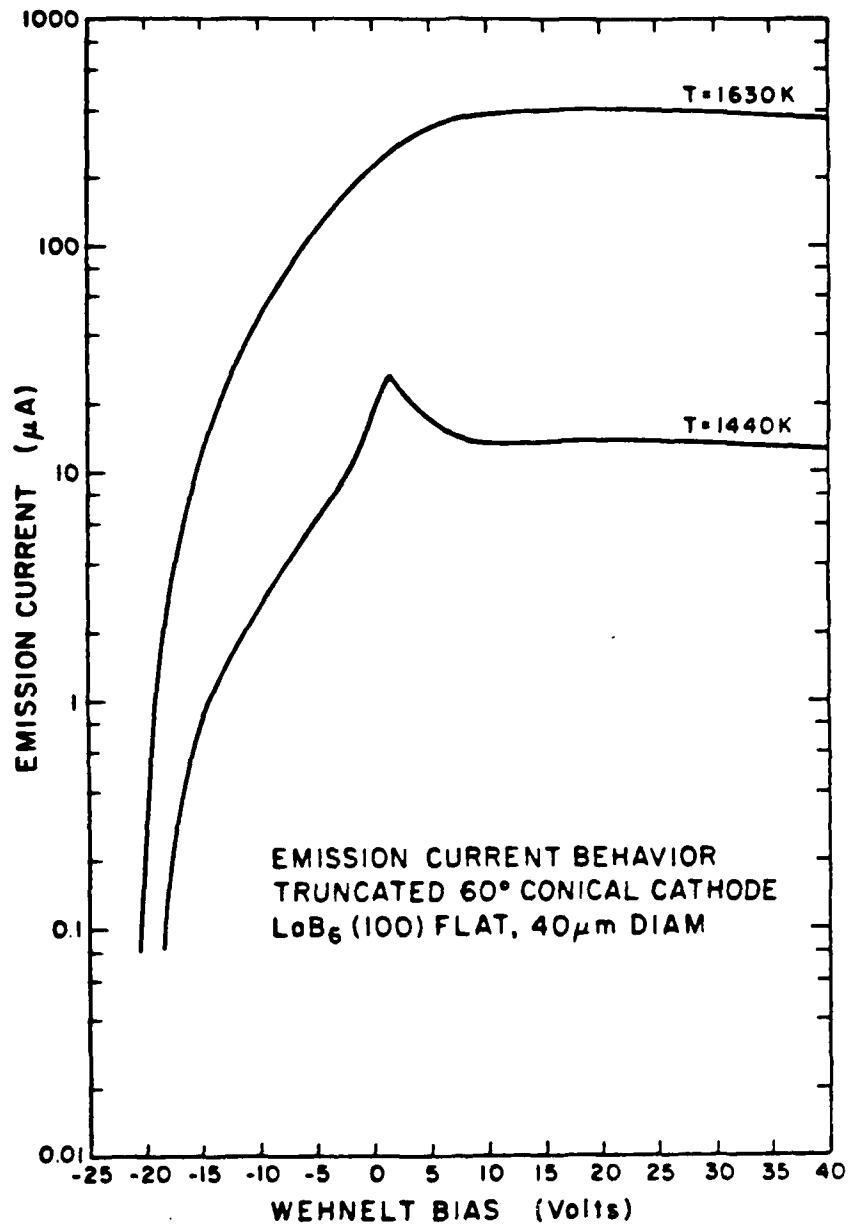


Figure 21. I-V characteristics of LaB₆(100) truncated cathode, 60° cone angle, after 5 hours of life at 1700 K.

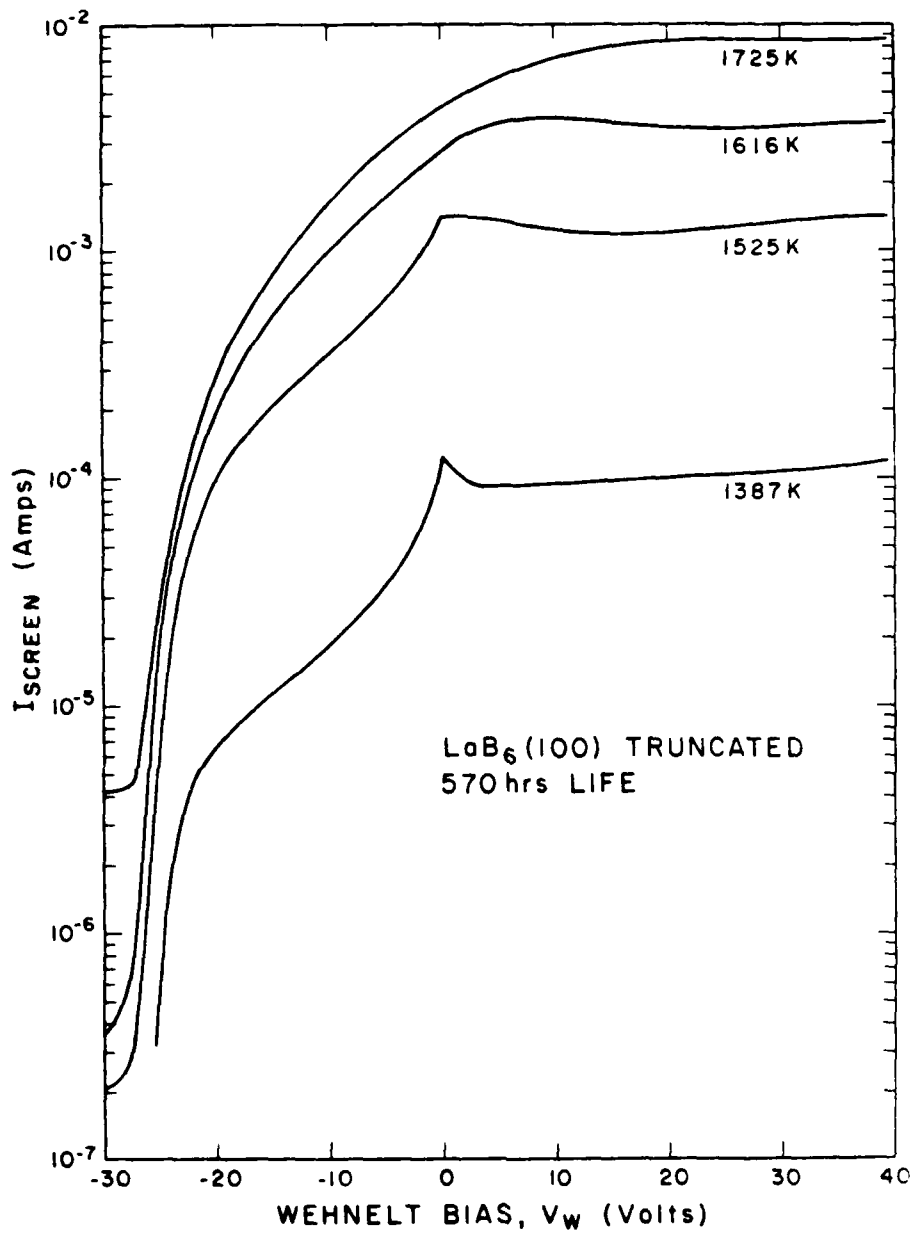


Figure 22. I-V characteristics of a 60° truncated cathode at various temperatures.

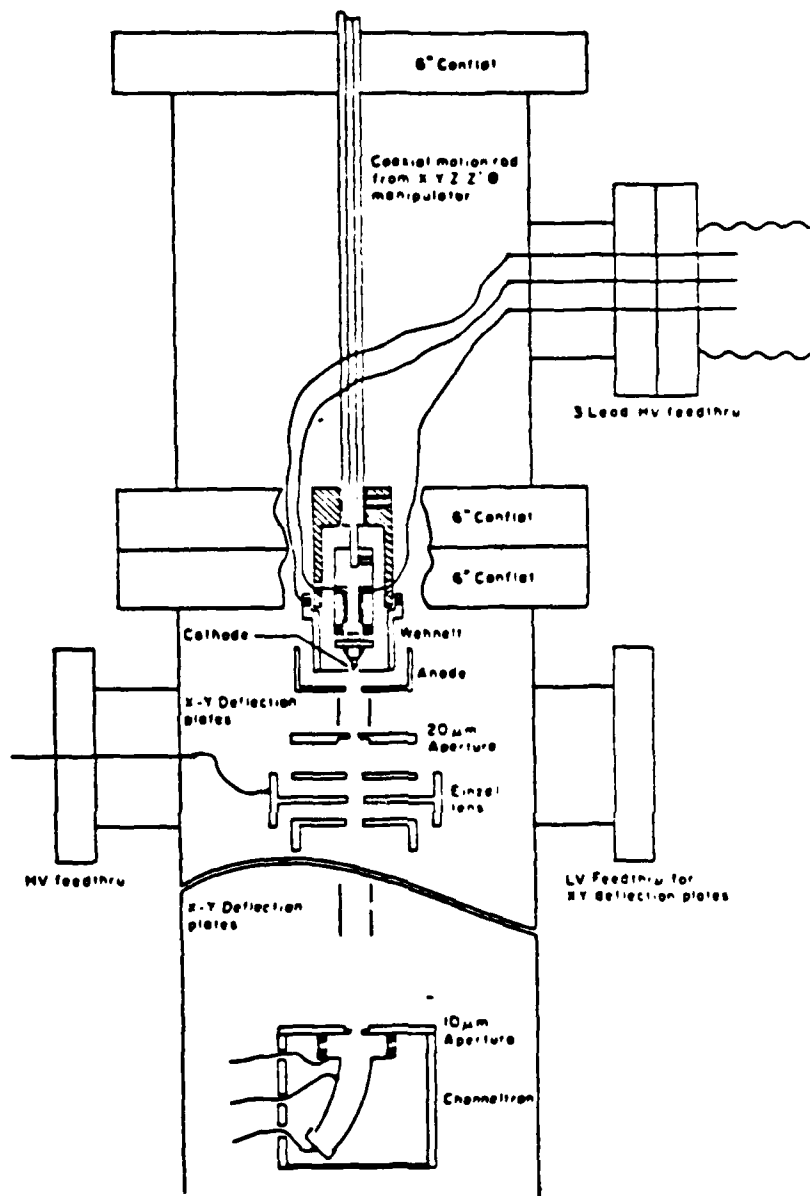


Figure 23. Diagram of optical column designed for emission spatial distribution measurements. The emission pattern is rastered across the 10 μm aperture and displayed on an oscilloscope.

perhaps are even improved, following 570 hours operation at 1700 K.

An optical column for precise studies of emitted current distribution at the cathode and crossover has been designed, constructed and tested. The optical and vacuum system is shown in Figure 23. The LaB_6 cathode is mounted in a Wehnelt structure and is movable along the axis of symmetry with respect to the Wehnelt. The Wehnelt/cathode assembly is movable in the x, y and z directions with respect to the anode-lens system. Deflection plates just below the anode and just below the einzel lens allow different portions of the cathode surface or crossover to be examined.

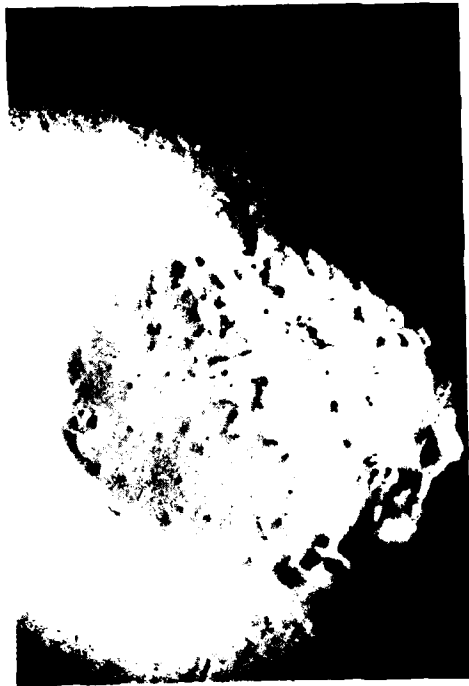
A crossover is produced just above the anode. Its image, magnified approximately 15 x is cast onto the image plane where a 10 μm aperture samples the current. The current passing through the aperture is amplified by a channeltron and the resulting signal used to modulate a CRT. The CRT is rastered with the same signal used to drive the deflection plates, thereby producing a realtime image of the crossover.

Initial qualitative measurements were made which clearly demonstrated that the four-fold symmetric structure of the crossover produced by a $\langle 100 \rangle$ oriented LaB_6 cathode could be resolved. Unfortunately, the einzel lens was mechanically damaged during the first trial runs, which precluded any quantitative data taking after the initial measurements were made. The optical system is being repaired at the present time.

(d) Life Test Results

Life test studies have been performed on a variety of LaB_6 cathodes of different geometries. Both pointed and truncated cone cathodes have been investigated, using both Vogel and sleeve-type (Re cup with TaC binder) mounts. Results of these studies are presented here.

We have successfully operated a truncated, 60° cone $\text{LaB}_6(100)$ cathode in a Vogel mount for over 3000 hrs at $T = 1800$ K. The cathode was in an operating electron gun capable of producing a 2 μm beam spot at 10 keV beam energy. The gun requires excellent mechanical stability and heating reproducibility of the cathode mount. Figures 24 and 25 show the cathode and cathode-Wehnelt alignment before and after life, respectively. Note in particular that the "after" surface is still relatively smooth, shows no



(a)



(b)



(c)

(d)

Figure 24. New truncated $\text{LaB}_6(100)$ cathode used in Vogel mount assembly a, cathode in Wehnelt aperture; b, front view of cathode; c, d, side view of flat region, showing opposite sides. The flat end of the cathode is $40 \mu\text{m}$ across.



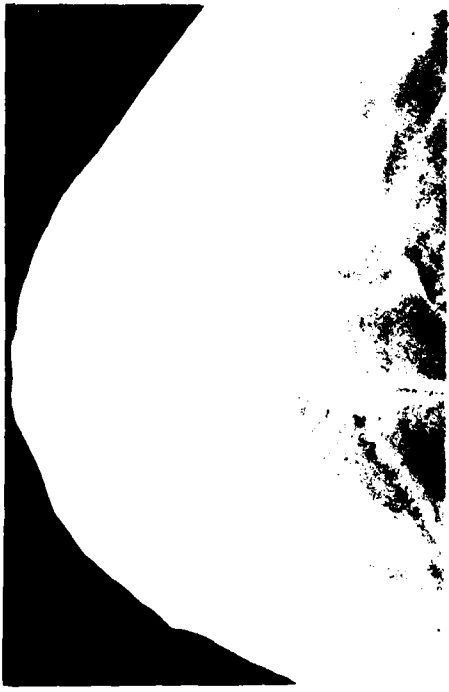
(a)



(b)



(c)



(d)

Figure 25. Truncated $\text{LaBa}_2(100)$ cathode after 3000 hours life at 1800 K. Views of a-d are the same magnification and approximately same orientations as in Figure 24.

inclusions, and still retains a flat region on the end. Also, very little if any material has been deposited on the Wehnelt aperture, which still appears clean and sharp.

End of life for this cathode was defined to be that operating times for which the ratio of beam current to total emission, I_B/I_T , dropped to 10% of its initial value for fixed gun element biases. The mechanism responsible for this drop is evaporation-induced retreat of the cathode emitting surface (truncation) from the plane of the Wehnelt front surface. This change of spacing could presumably be corrected for in a system with adjustable Wehnelt bias, thus extending the useful cathode lifetime. Even in the "end of life" case, the ratio I_B/I_T is greater than for a new 60° pointed ($5 \mu\text{m}$ radius) $\text{LaB}_6(100)$ cathode in this gun, and the lifetime is greater because, for the same evaporation rate, a 60° point will recede four times faster than a flat surface.

Difficulties involved with use of the sleeve type mount (Figure 10b) in long-life applications (i.e., ≥ 500 hrs) primarily involve contamination of the cathode surface. Extensive studies of the effects and likelihood of contamination have been performed. We find that almost any refractory material deposited or vaporized onto a clean LaB_6 surface causes localized disruption of the surface. Table XII summarizes the effects of various contaminant materials we have observed on life-tested cathode surfaces. We have not observed any surface inclusions in life tested cathodes other than those incorporating metallic impurities. None of the second phase La-B-O compound has been positively identified in the life-tested cathodes, even in cases where it was detected before heating.

It should be noted that, in several cases, submicron particles, more or less uniformly distributed, were observed in SEM studies of life-tested cathode surfaces, but particles this small cannot be characterized by the SAM system available to us. In addition, energy dispersive x-ray analysis, performed in the SEM, is not very reliable on such small particles and does not allow elements (B, C, O) to be detected. We therefore are uncertain of the composition of these particles. However, in every case where the small particles were observed, larger particles containing metallic impurities

TABLE XII

EFFECTS OF REFRACTORY CONTAMINANTS ON LaB_6 SURFACES

<u>Contaminant</u>	<u>Source of Contaminant</u>	<u>Effect on Surface</u>
Mo	Vaporization from Mo cup initially used to hold sample	Micron and submicron sized particles protruding from surface--apparently forms Mo-La-B compound
Re	Vaporization from Re cup used to hold sample	Micron and submicron sized particles protruding from surface--apparently forms Re-La-B compound
TaC	Dusted onto surface during mounting procedure, not properly cleaned	Pits form around TaC particles--local faceting to radius of about 5 particle diameters
Mg, Si, O	Probably bulk contaminant not removed during zone refining	Particles several μm in diameter

were also seen, so we assume the smaller particles to be of similar composition.

The consequences of having contaminant particles present on the cathode surfaces are not well understood, but do not seem to be particularly severe as long as the total coverage is not large. Individual particles may cause local increases in volatility and changes in stoichiometry and morphology of the surface, possibly reducing emission from the affected area and reducing overall cathode lifetime. The emission distribution may also be disturbed by the presence of contaminant particles. None of these effects has been investigated quantitatively. Our approach has been to avoid the contamination and thus remove any associated difficulties.

The most successful way to avoid contamination is to use a mount such as the Vogel design which eliminates the possibility of any evaporating material at all, except for the LaB_6 itself. Alternatively, mounts such as

the Re cup structure may be designed to reduce or eliminate the possibility of evaporation directly onto the cathode emitting surface. Finally, in any design, extreme care must be used when mounting cathodes, to avoid depositing foreign material onto the active cathode surface.

(e) Field Emission Characterization

Field electron and field ion microscope patterns of thermally annealed and field evaporated end forms of LaB_6 were obtained. The microscope studies were performed in a standard, low temperature (77 K) field ion microscope (FIM) using a microchannel plate to intensify the hydrogen or helium ion image. Image gas pressures were typically 1×10^{-10} torr. The FIM was mounted on a bakeable, ultra-high vacuum system capable of a base pressure of 5×10^{-11} torr. For the FIM studies needle-like crystals obtained from the molten Al solvent method described by Futamoto, et al.¹ were employed.

The low temperature (77 K) field electron and ion emission patterns for three emitter end forms are shown in Figure 26. Photos (a)-(d) of Figure 26 show patterns obtained after field evaporation in H_2 and He; photos (e) and (f) show the field ion (H_2 image gas) and electron emission patterns of the thermally annealed ($T \sim 1800$ K) end form. Field evaporation in H_2 and He occurred at voltages 20% and 30% above their respective best image voltages (BIV). The He BIV was ~ 1.9 times larger than the H_2 BIV value. A comparison of the H_2 field ion pattern of Figure 26(a), which reflects the local field enhancement distribution, with the corresponding electron pattern in Figure 26(b), which reflects both the work function and field distributions, clearly shows that $\phi_{110} \sim \phi_{100}$ for this end form. In contrast, the end form obtained after field evaporation in He, while exhibiting a similar ion pattern (Figure 26(c)), shows an electron pattern in Figure 26(d) which suggests a work function reversal, i.e., $\phi_{100} \sim \phi_{110}$. A result similar to Figure 26(c) and 26(d) was obtained after field evaporation in vacuum. By adsorbing H_2 on the Fe field evaporated end form it was determined that the electron emission pattern difference between Figure 26(b) and 26(d) was not due to adsorbed H_2 .

The field ion and electron patterns of the thermally equilibrated end forms shown in Figures 26(e) and 26(f) are similar to those observed by Futamoto, et al.^{2,3} However, according to our results the latter authors

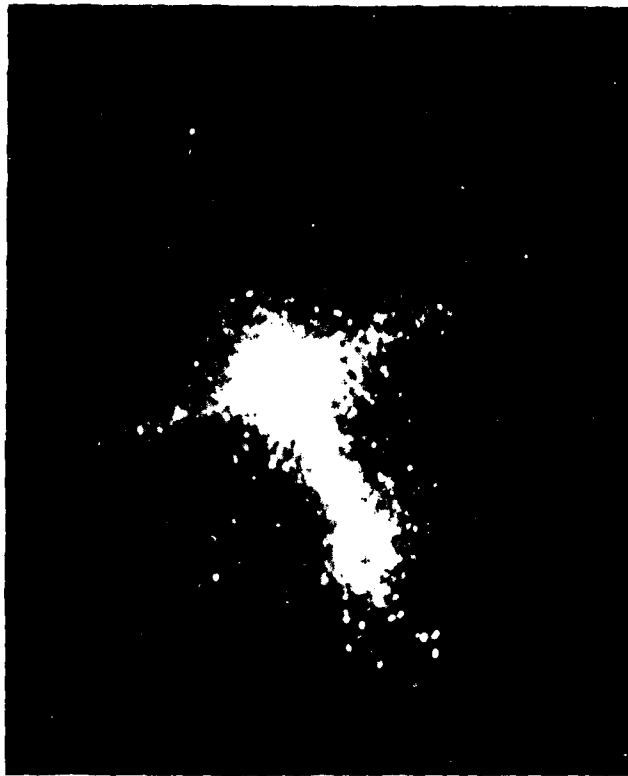


Figure 26(a). Hydrogen field ion image of a (100) oriented LaB_6 emitter after field evaporation in H_2 , BIV = 13 kV.

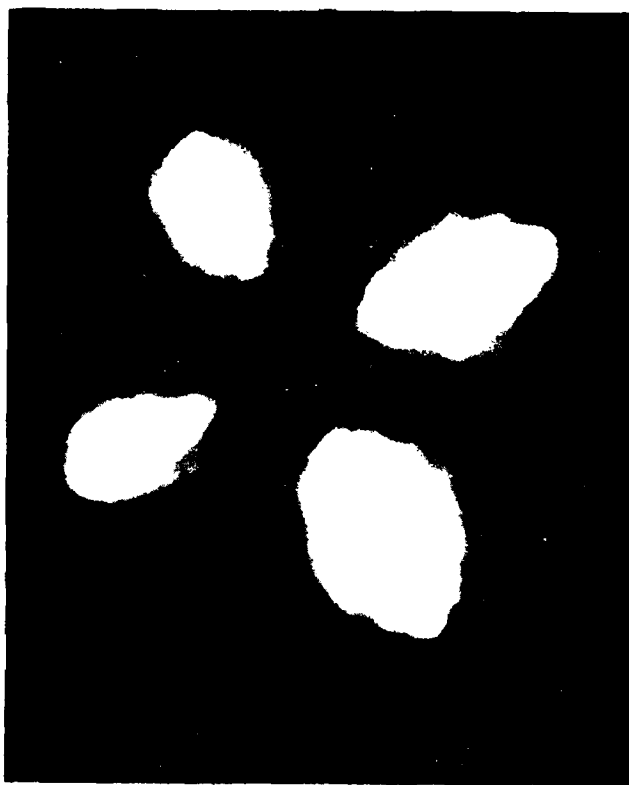


Figure 26(b). Field electron image of H. field evaporated end form.



Figure 26(c). Helium field ion image of a (100) oriented LaB_6 emitter after field evaporation in He, $BIV = 24 \text{ kV}$.

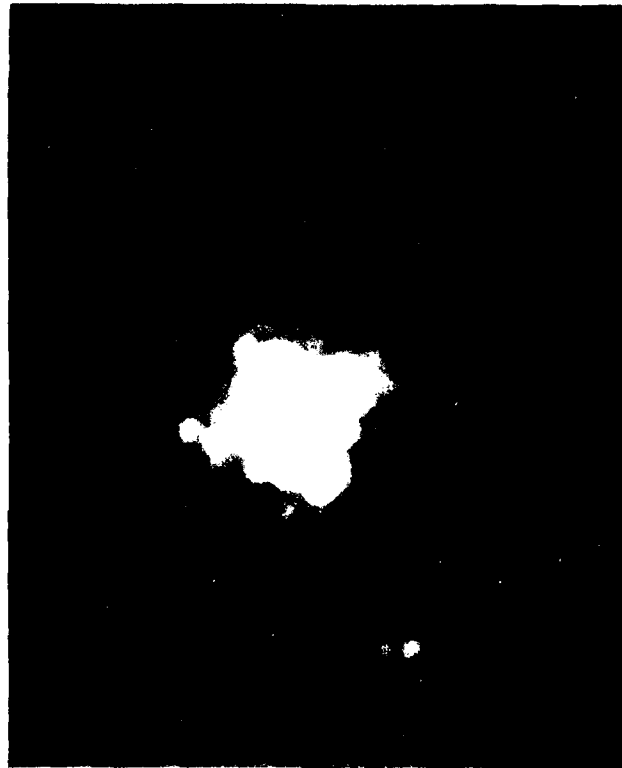


Figure 26(d). Field electron image of the He field evaporated end form.



Figure 26(e). Hydrogen ion image of a (100) oriented LaB_6 emitter after annealing 15 min. at 1800 K.



Figure 26(f). Field electron image of thermally annealed end form.

appear to have inadvertently rotated the field electron pattern 45° relative to their indicated crystallographic designations. Upon thermal equilibration between 1600 and 1800 K the low index planes increase in size in the order (111) > (110) > (100). In addition, the (210-310) regions become slightly faceted. Also in agreement with Futamoto, et al.,²² we found that long term heating at $T \approx 1800$ K led to irreversible formation of field enhanced micro-crystallites randomly distributed over the surface.

These results clearly show that the work function difference between the (110) and (100) planes of the LaB_6 can be radically changed by the conditions of field evaporation.

Table XIII shows the best image voltages (BIV) and corresponding slopes m of the electron $I(V)$ characteristics of the various emitter end forms plotted according to the Fowler-Nordheim equation (i.e., $\log(1/V^2)$ vs. $1/V$). In this case

$$m = 2.8 \cdot 10^7 \phi^{3/2}/F \text{ (volts)} \quad (3)$$

and

$$F = F/V \quad (4)$$

where the work function ϕ and field factor F are in units of eV and $\text{cm}^{-1/2}$ respectively and F is the electric field. An important finding was the nearly 68% decrease in m when the field evaporated end forms were thermally equilibrated. According to Eq.(3) a reduction in m implies either a decrease in ϕ or increase in ϕ . Since the H_2 BIV values (and hence F values) for the field evaporated and thermally equilibrated end forms are nearly identical, we conclude that the average ϕ for the latter end form is 32% lower than the H_2 or He field evaporated end forms.

Atom probe studies of the LaB_6 surface in He imaging gas show field evaporation occurring as $\text{B/La} \approx 6$, thus leaving a near stoichiometric surface.²³ However, upon heating to $T \approx 1800$ K the atom probe results showed predominantly La in the surface layer. In view of the atom probe results we conclude that thermal equilibration leads to a restructuring of the surface causing the "quenched in" 77 K surface to exhibit a simultaneous reduction in ϕ and formation of a La rich surface layer. From the Figure 26(f) photo we further conclude that low work function regions of the

TABLE XIII
SUMMARY OF BEST IMAGE VOLTAGES (BIV) AND FN SLOPES FOR THE
INDICATED IMAGE GAS AND END FORM OF THE LaB₆ EMITTER

End Form	Image Gas	BIV (kV)	FN Slope (volts)	Low Work Function Plane
Field Evap. in H ₂	H ₂	13	4.4×10^4	(110)
Field Evap. in He	He	25	4.4×10^4	(100)
Thermally Equil. (~ 1800 K)	H ₂	13	1.4×10^4	(112)

thermally equilibrated end form occur at the higher index (112) planes. However, from the obvious faceting of the (210-310) region (see Figure 26 (e)) an equally low work function for these higher index planes cannot be ruled out.

From the Table XIII results and Figure 26 patterns of the field evaporated end forms, it can be concluded that, although the work function distribution is dramatically changed depending on whether field evaporation occurs in H₂ or He, the average work function is virtually unchanged. The reason for the reversal in the minimum work function between the (110) and (100) planes is believed to be due to an anisotropy in the surface B/La ratio brought about by field evaporation in H₂. According to atom probe results,²³ La is preferentially removed from the surface when field evaporated in H₂. If this is specific to the (100) plane, this may lead to an anisotropy in the surface B/La stoichiometry and hence the change in the work function distribution noted in Figures 26(b) and 26(d).

Experiments have also been performed using FIM and FEM to study systematically the LaB₆ surfaces which result from heating in vacuum ($p \leq 5 \times 10^{-9}$ torr). The purpose of the investigation was to elucidate the mechanisms which lead to a reduction in the Fowler-Nordheim (FN) slope of the annealed endform as compared with the field evaporated surface and to determine the thermally stable crystal planes.

The BIV for an H₂ FIM image at 77 K was constant over the range of emitter annealing temperatures measured, so changes in the FN slope are interpreted as caused by changes in the average work function. Anneals of two minute duration were used in approximately 100 K intervals over a range of 300-1800 K after first forming a field evaporated end form. At each point on the temperature scale a field electron pattern was obtained with a Fowler-Nordheim plot and a corresponding field ion pattern using hydrogen as an imaging gas. Figure 27 shows the FN slope as a function of temperature. The error bars correspond to the variation in values obtained from two runs of the above mentioned experiment. The FIM and FEM patterns were reproducible within a range of approximately 100 K. This uncertainty presumably could be reduced by extending the anneal time to allow the

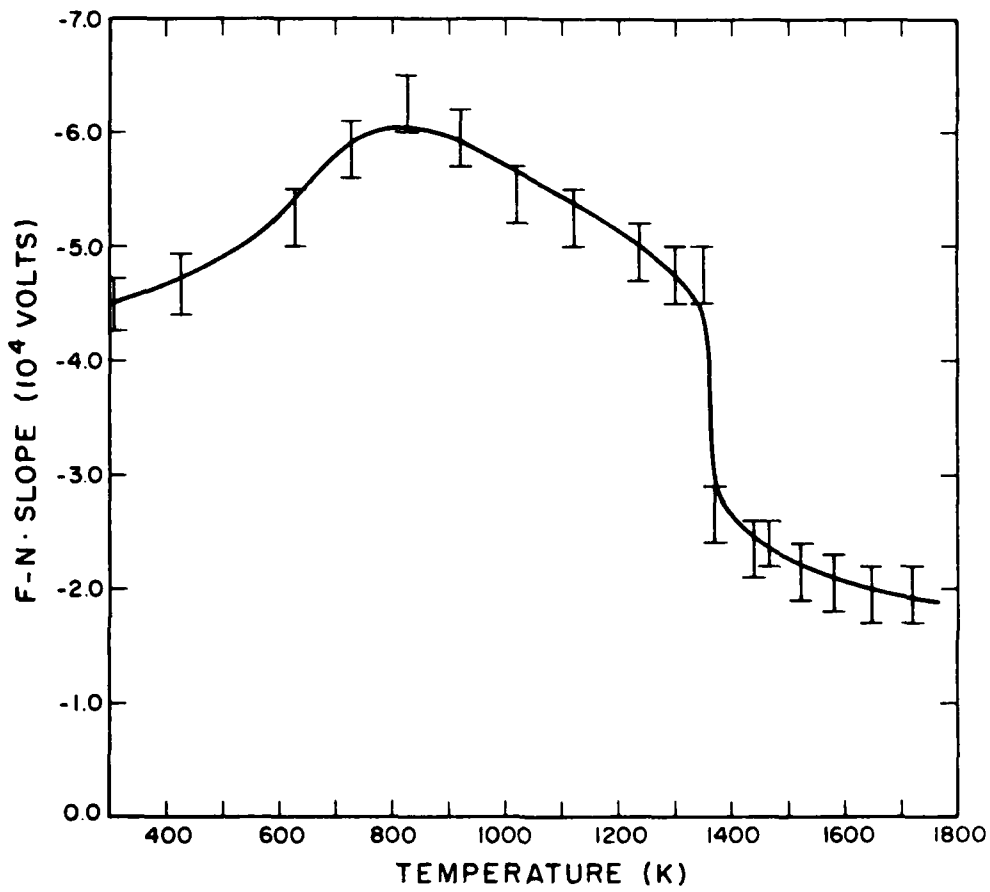


Figure 27. Plot shows the variation of FN slope of a LaB₆ emitter (after initially field evaporating in H₂ at 77 K) with heating at the indicated temperature for 2 minutes.

surface to approach equilibrium even more closely. Figures 28-32 are typical of FEM (primed) and H₂ FIM patterns (unprimed) after the indicated annealing temperatures.

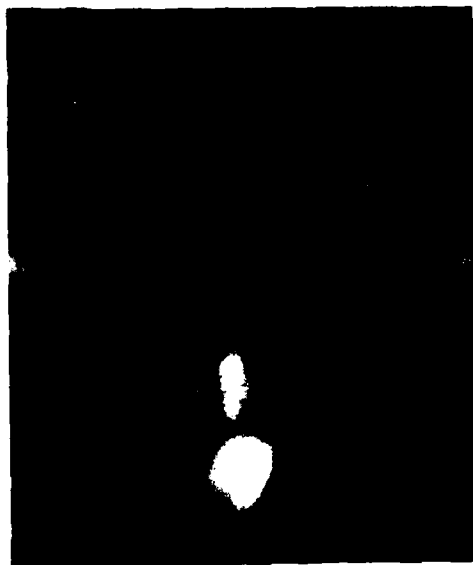
Figures 28(a) and (a') show the typical FIM and FEM patterns observed from an end form obtained by field evaporating in hydrogen. The field electron image shows the (110) and (210) planes to be the highly emitting regions. For this end form, we have determined that $\phi_{110} < \phi_{100}$.

Figure 28(b') shows the (111) to be bright and indicates that surface reconstruction of the evaporated surface is already taking place at 725 K. Since the field evaporated end form surface is believed to be boron-rich, this reconstruction may result from La atoms being displaced outward on the (111) planes, thus creating a reduced work function barrier due to the more electropositive nature of the La atom.

Since the FN slope has not changed drastically, only relative changes in work function have occurred. It is interesting that a relatively low temperature has been able to activate this process. The field ion image shows no change, thus supporting the view that only local atomic rearrangement has occurred.

Figure 29(a) shows the effect that annealing for two minutes at 910 K has on field electron emission. Note the brightest electron emission regions have returned to the (110) plane with the next brightest areas being the (111). Again the FIM image (Figure 29(a)) shows no change. Note that the FN slope also increases in this temperature range above the evaporated endform value, thereby indicating an overall increase in work function.

Upon annealing at 1120 K (Figures 29(b), 29(b')) the field ion image shows an increased concentration of random spots over the entire surface. The field electron image indicates a relative lowering of the (100) work function along with the formation of a ring on emission intersecting the (111) and (110) planes. Continued annealing between 1220 and 1295 K (see Figure 30) shows continued formation of random spots in the FIM patterns and high electron emission in the normally high work function (111) region. It is likely that gross surface migration of La atoms from the emitter shank (i.e., where field evaporation cannot occur) may be occurring in this temperature range, thereby filling La surface vacancies in the planes located near



(a) H₂ Field Evaporated, 77 K (a')



(b) 725 K (b')

Figure 28. TEM (unprimed) and FEM (primed) patterns. The BEV = 13 kV for the hydrogen ion image. The patterns correspond to the indicated temperatures on the Figure 27 curve.



(a)

910 K



(c)



(b)

1170 K



(d)

Figure 29. TEM images (a) and (b) were taken after 100 s at 910 K and 1170 K, respectively, for the $Al_{20}Ga_{80}$ nanodroplets. (c) and (d) were taken after 100 s at the indicated temperatures of the $Al_{20}Ga_{80}$ nanodroplets.



(a)

1220 K



(a')



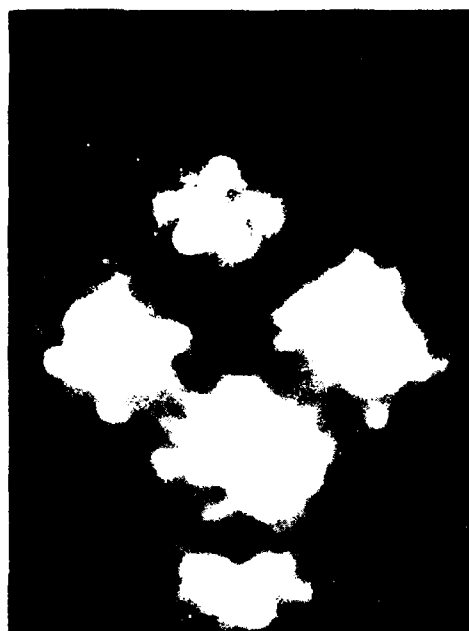
(b)

1295 K



(b')

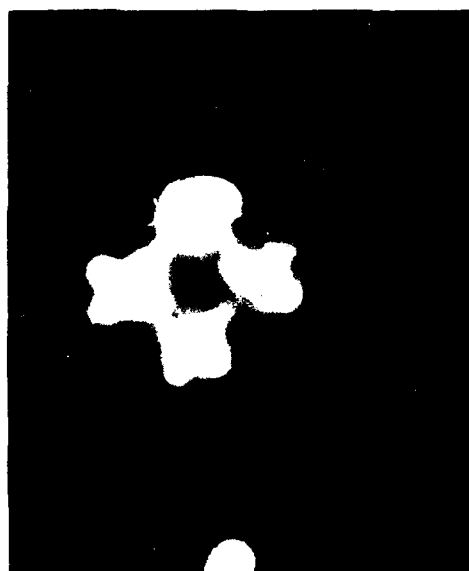
Figure 30. FIM (unprimed) and FEM (primed) patterns. The FIV = 13 kV for the hydrogen ion images. The patterns at each temperature correspond to a point on Figure 27.



130

130 S

130



130

130 S

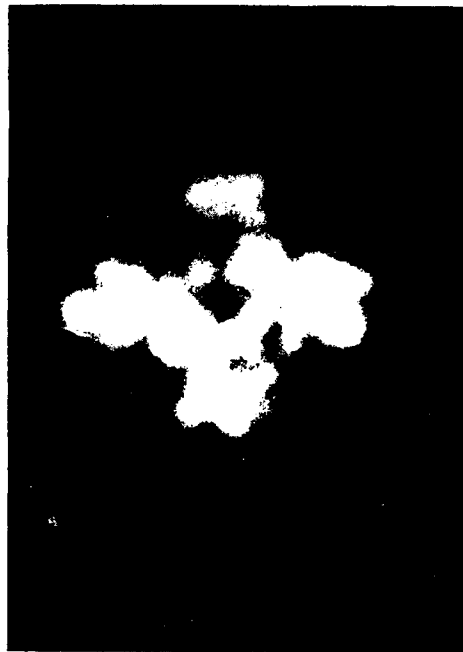
130

Figure 1. Comparison of the results of the two different methods of image processing.



(a)

1715 K



(a')



(b)

1770 K



(b')

Figure 1. (a) and (b) are D and ^{137}Cs maps for a cluster of particles at 1715 K and 1770 K, respectively. (a') and (b') are the corresponding SEM images.

AD-A113 807

OREGON GRADUATE CENTER BEAVERTON

F/G 20/2

RARE EARTH BORIDE ELECTRON EMITTER MATERIALS FABRICATION AND EV--ETC(U)

MAR 82 L W SWANSON, P R DAVIS, M A GESLEY

F19628-80-C-0117

UNCLASSIFIED

RADC-TR-82-12

NL

2 of 2

AD-A
113807



END
DATE
FILMED
05-82
DTIC

the periphery of the pattern, i.e., the (110) and (111) planes and vicinals.

Annealing at 1335 K leads not only to a dramatic change in FEM pattern, but also to a sharp reduction in work function. The (210-310) planes and surrounding higher index crystallographic regions remain as the highly emitting regions with continued increase in annealing temperature. The FEM patterns in Figures 31 and 32 show significant faceting of the (100), (110) and (112) planes. The (111) plane appears to be faceting as well. It can be concluded that gross surface migration is occurring in this temperature range, and that the faceted planes are those of lowest surface free energy (i.e., most thermally stable). With this end form little can be concluded regarding the relative work function distribution on the surface except that it possesses a lower average work function than the field evaporated end form by about a factor of 0.6.

4. Task IV: Surface and Bulk Properties Characterization

(a) Background

The measurements described here, like portions of those discussed under Task III, were carried out in an ULTEK TBK 250 liter/sec ultra-high vacuum system. The system had a rotatable specimen manipulator so that several sequential measurements could be performed. In addition to a guarded thermionic collector, the following surface analysis probes were simultaneously available: (1) line of sight EAI Model 300 quadrupole mass spectrometer; (2) Physical Electronics CMA Model 10-155 Auger Electron Spectrometer (AES); (3) ion bombardment gun; (4) Varian Model 981-0127 low energy electron diffraction (LEED) optics; (5) field emission retarding potential (FERP) gun for work function measurements of the crystal. A schematic diagram of the analysis system is shown in Figure 33.

The AES measurements were performed with a 5 to 10 μ A primary beam current at 3 and 5 kV beam energy. Quantitative analysis of the AES data was achieved by measuring the peak-to-peak heights of the derivative of the $N(E)$ curve obtained using 1 V modulation. In addition, SAM measurements could be performed in a separate system, so the spatial distribution of surface species across the analyzed sample could be determined. The SAM used

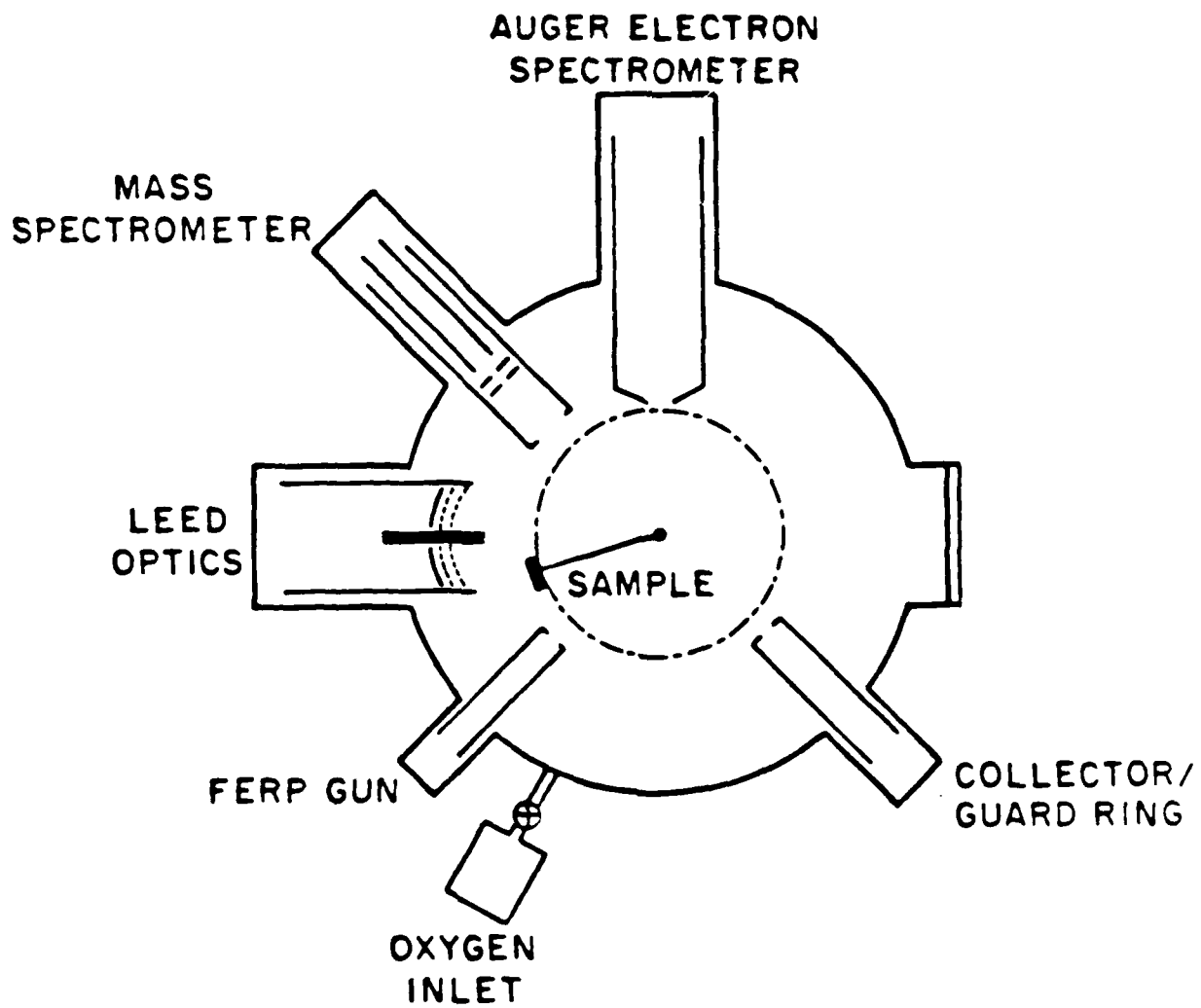


Figure 33. Diagram of surface analysis probes available on the ultra-high vacuum chamber.

was a Physical Electronics-Perkin Elmer Model 590, capable of 2000 Å spatial resolution, normally used with beam current and energy of ~ 1 nA and 5-10 keV, respectively.

Vaporization rates of the various RB_6 crystals were measured by monitoring B and R mass peaks using the quadrupole mass spectrometer. In this study, absolute calibrations of the mass loss rates for B and R were not performed, but relative comparisons could be made.

The FERP method of work function measurement, described in detail elsewhere,²⁴ involves a retarding potential $I(V)$ measurement using a field electron source. The unique aspect of this technique is that the $I(V)$ threshold measures the absolute collector work function directly. In addition, it is possible to measure the reflection coefficient of the elastic and/or inelastic scattered electrons near the threshold voltage as a function of the primary beam energy.

(b) Surface Composition and Geometry

The AES results were used to determine the procedures required to clean the surfaces and to establish the surface B/R ratios. The latter along with LEED results were expected to help determine the geometric structure of the various crystal faces and, hopefully, their role in the crystallographic variation of work function. Auger transitions utilized in these studies were La(NOO, 78 eV) La(MNN, 625 eV), Ce(NOO, 82 eV), Ce(MNN, 661 eV), Pr(NOO, 87 eV), Pr(MNN, 699 eV) and B(KLL, 179 eV).

It was determined by AES that oxygen and carbon were the only surface contaminants requiring a high temperature ($T > 1700$ K) to remove. Although oxygen could be desorbed from each crystal by heating alone, this was not always the case for removal of carbon. In cases of heavy carbon contamination it was necessary to heat the crystal to ~ 1400 K in an oxygen pressure of $\sim 10^{-6}$ torr in order to remove surface carbon as CO.

The AES results from various crystal faces of RB_6 compounds given in Table XIV show the effect of crystal plane and temperature on the B/R Auger peak ratios. Results for several crystals are reported after initial thermal cleaning (a) and after several hours of heating (b) at 1700-1800 K. As shown in Table XIV a very large temperature dependence of the B(179)/La(78) and La(78)/La(625) Auger peak ratios was generally observed for LaB_6 (a) crystals.

TABLE XIV
 RATIO OF AES PEAK HEIGHTS FOR VARIOUS CRYSTAL FACES OF RB₄ COMPOUNDS
 (Primary beam energy: 5 kV)

Bulk B:B Ratio	Crystal Face	T = 300 K			T = 1600 K			% Change During Heating of R(B)/ R(SNN)	
		B(KLL)* R(NOO)	B(KLL) R(SNN)	R(NOO) R(SNN)	B(KLL) R(NOO)	B(KLL) R(SNN)	R(NOO) R(SNN)		
LaB ₄	(100)a	9.3	2.0	0.22	2.3	4.0	1.7	67	
	(100)b	1.0	4.6	4.6	1.0	4.1	4.1	-22	
	(110)a	2.3	5.9	2.6	1.3	5.6	4.3	65	
	(110)b	1.1	5.8	5.3	1.1	5.4	4.9	-8	
	(111)b	1.3	6.1	4.7	1.3	5.9	4.5	-2	
	(346)b	1.2	5.0	4.2	1.2	4.6	3.8	-1	
	(100)a	1.7	3.3	1.5	1.5	3.8	2.5	67	
	(100)b	1.1	4.9	4.6	1.2	4.3	3.6	-21	
	(110)a	2.0	2.6	1.3	1.3	4.4	3.4	162	
	(110)b	1.1	5.2	4.7	1.2	4.7	3.9	-17	
	(321)b	1.1	4.9	4.3	1.3	4.0	3.0	-30	
	CeB ₄	(100)a	1.1	4.7	4.4	1.3	3.9	3.0	-31
		(100)b	1.1	4.4	4.0	1.3	5.0	3.9	-3
		(211)a	1.2	4.8	4.4	1.5	4.0	2.7	-38
(211)b		1.2	5.1	4.1	1.5	3.7	2.4	-42	
c		(100)	0.9	6.0	6.3	1.1	5.2	4.6	-27
c		(111)	1.2	6.4	5.4	1.3	5.3	4.1	-14
PrB ₄	(100)a	1.0	5.7	6.0	1.2	4.5	3.8	-37	
	(100)b	1.0	6.0	6.0	1.3	4.7	3.7	-38	
	(100)a	1.1	7.0	6.4	1.2	5.6	4.6	-28	
	(100)b	1.1	7.3	7.0	1.2	6.0	4.8	-32	

*Letters in parentheses indicate Auger transition: B(KLL) = 179 eV; La(NOO) = 76 eV; La(SNN) = 625 eV; Ce(NOO) = 82 eV; Ce(SNN) = 661 eV; Pr(NOO) = 87 eV; Pr(SNN) = 699 eV.

a = After initial thermal cleaning.
 b = After prolonged heating at 1800 K.
 c = Precise bulk stoichiometry unknown.

High temperature measurements made at 1700 K.

This temperature dependence subsequently decreased, changed sign and became reproducible for the (b) crystals. The small difference in the interior B/La ratios of $\text{LaB}_{5.86}$ and $\text{LaB}_{5.74}$ crystals is reflected in the La(78)/La(625) ratios for the (100) and (110) (b) surfaces.

Analysis of the data showed that the La(78) and B(179) Auger peak heights varied with temperature while the La(625) was mostly unchanged, thereby suggesting that only the outer surface layer participated in the reversible, temperature dependent compositional change. The larger values of B(179)/La(78) for the (a) in comparison with the (b) surfaces suggest that the former surface structures are La deficient. The (a) behavior can easily be missed if long-term, high temperature heating is carried out during the initial thermal cleaning. Reproducibility of the AES ratios at a specific temperature was difficult to obtain within $\pm 5\%$.

A comparison of the various high and low temperature AES B/La ratios for the major planes of the (b) crystals indicates a general increase of the B/La ratio in the order (100) < (110) < (111). It will be shown later that the (111) plane, with the highest surface B/La ratio, also exhibits the highest value of work function of the low index LaB_6 crystal faces.

Table XIV also shows that the a-b type transition has not been observed in CeB_6 or PrB_6 crystals. This result suggests that CeB_6 and PrB_6 surface layers attain an equilibrium B/R ratio very rapidly, a reasonable conclusion since diffusion in CeB_6 and PrB_6 is expected to be faster than in LaB_6 .

We have also made AES measurements on $\text{LaB}_6(100)$ surfaces prepared by fracturing in vacuum and by sputter cleaning. Table XV shows the Auger peak height ratios for the various surface end forms. The conclusion is that the fractured surface ratio represents a stoichiometry of $\text{B/La} \sim 6$, while heating causes the surface to be greatly enriched in lanthanum. Sputtering tends to remove boron preferentially, resulting also in a La-rich surface.

It is clear that the composition of the LaB_6 surface is strongly affected by heating and other methods of cleaning. It is also influenced by interaction with contaminant gases, such as oxygen. Investigation of residual gas effects upon the surface composition was not a specific part

TABLE XV
 AUGER PEAK HEIGHT RATIOS FOR IN SITU FRACTURED
 AND Ar⁺ SPUTTERED LaB₆(100) SURFACES
 PRIMARY BEAM ENERGY, 5.0 keV
 T = 300 K

	$\frac{B(KLL)^+}{La(NOO)}$	$\frac{B(KLL)}{La(MNN)}$	$\frac{La(NOO)}{La(MNN)}$
In-Situ Fractured	3.7	5.2	1.4
Ar ⁺ Sputtered (~ 100 Å removed)	1.4	2.4	1.7
Annealed (1700 K) LaB _{5.86} (100)*	1.0	4.6	4.6

⁺B(KLL) = 179 eV; La(NOO) = 78 eV; La(MNN) = 625 eV

*Data from Table XIV, included for comparison

of the research effort supported under this contract. However, we studied some of these effects in earlier work¹⁴ and those results may be applicable to cases where LaB_6 cathodes are operated in relatively high residual gas pressures (e.g., $> 10^{-8}$ torr active gases).

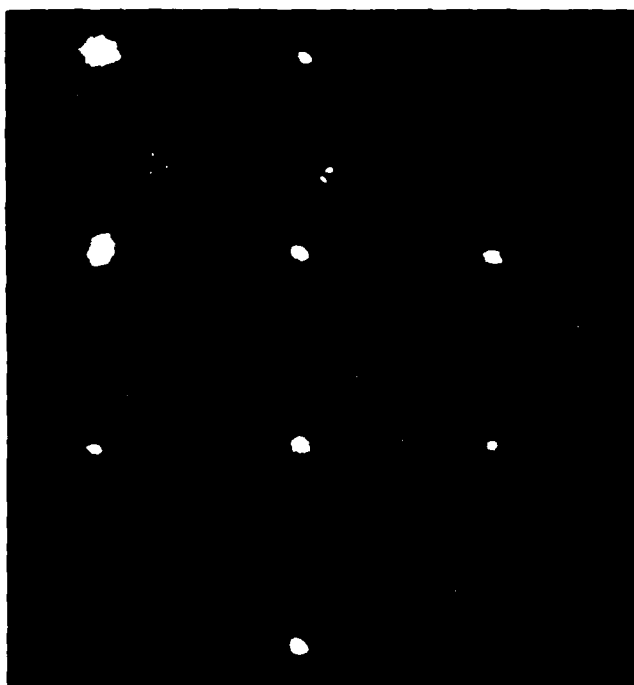
In addition to AES studies, room temperature LEED measurements were performed on some samples. Shown in Figure 34 are LEED patterns of the thermally annealed surfaces of (111), (110) and (100) LaB_6 . These patterns show an array of sharp spots in symmetry with the underlying bulk structure in each case. From this we conclude that no surface layer reconstruction occurs at room temperature for the (100), (110) and (111) crystal faces. At lower primary electron beam voltages the (110) plane has been reported²⁵ to exhibit a $c(2 \times 2)$ structure which transforms to 1×1 at $T > 1120$ K.²⁶

(c) Volatility

A direct comparison of the vaporization rates of identically prepared (100) surfaces of LaB_6 , CeB_6 and PrB_6 has been made. Vaporization energies of the rare earth element and boron have been calculated from the slopes of $\ln(IT)$ vs $1/T$ plots, where I is the spectrometer current corresponding to the desired element and T is the absolute temperature. These results are shown in Table XVI. Also included is a summary of relative evaporation rates (B from LaB_6 arbitrarily chosen to be 1.0) of the rare earth elements and boron determined at 1800 K.

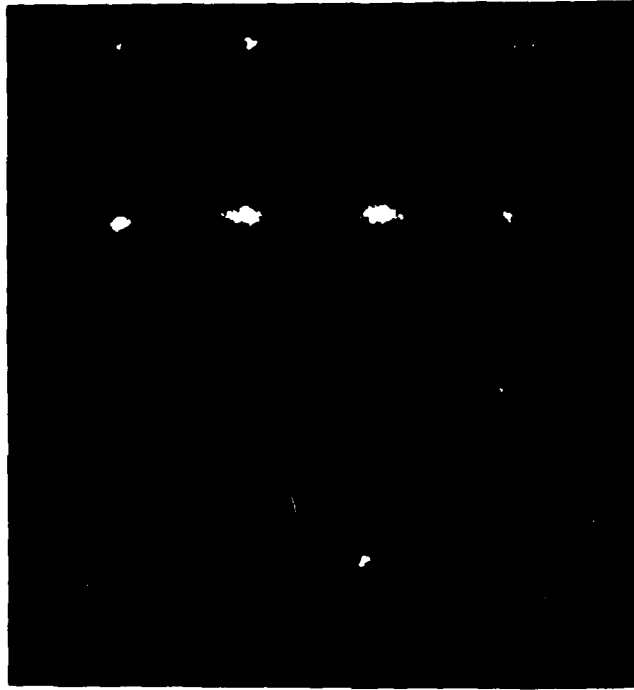
TABLE XVI
VAPORIZATION ENERGIES OF THE RARE EARTH ELEMENT (E_R) AND BORON (E_B)
FROM (100) SURFACES OF RB_6 COMPOUNDS

Compound	E_R (eV)	E_B (eV)	Relative Evaporation Rate at 1800 K	
			R	B
$\text{LaB}_{6.09}$ (100)	5.7	7.3	24.0	1.0
$\text{CeB}_{6.2}$ (100)	5.3	6.3	14.3	2.1
$\text{PrB}_{5.97}$ (100)	4.9	6.5	35.5	1.8



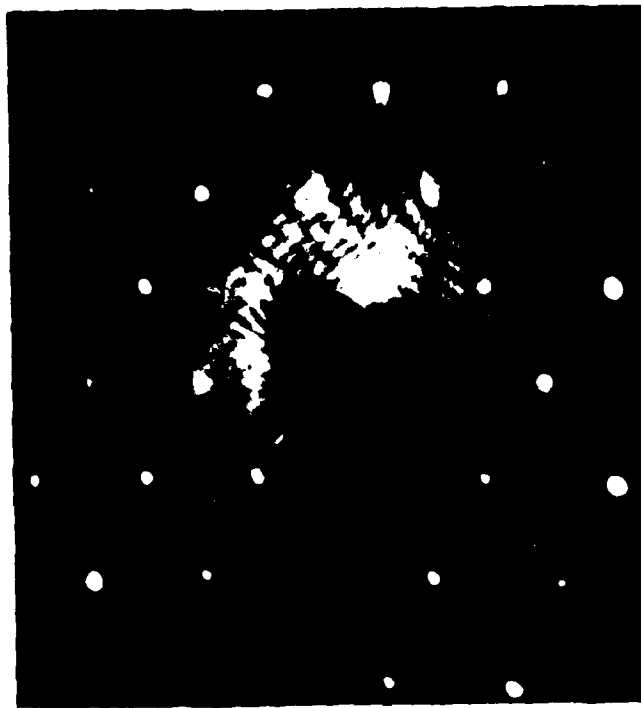
LaB₆(001) LEED Pattern

Figure 34. LEED patterns taken at $V_p = 100$ V of selected LaB₆ crystals used in this study: (a) (100); (b) (110); (c) (111).



LaB₆(110) LEED Pattern

Figure 34(b)



LaB₆(111) LEED Pattern

Figure 34(c)

The relative evaporation rates are calculated from ion currents measured with the quadrupole mass spectrometer. Corrections are made for the QMS mass sensitivity, based upon calibrations with rare gases, and for relative ionization probabilities of the rare earth elements and boron. It is assumed that La, Ce and Pr have identical ionization probabilities. We may thus attribute a total relative evaporation rate to each sample, which is the sum of the B and R rates. On this basis, at 1800 K CeB₆ has the lowest and PrB₆ the highest vaporization rates of the RB₆ materials examined.

The evaporation rate R is given by an equation of the form

$$R = A e^{-E/kT} \quad (5)$$

where A is a pre-exponential factor and k is Boltzmann's constant. There is evidence²⁷ to suggest that the transition from bound to free states may involve considerably different internal energy rearrangement when comparing one rare earth element to another. These effects, caused by different f-electron configurations, could be expected to appear in the pre-exponential factor A. Table XVII shows relative pre-exponential factors, A_R (rare earth) and A_B (boron) for the three surfaces at 1800 K, calculated from Eq. 5 using the energies given in Table XVI. Since the absolute rate R is unknown, only relative values of the pre-exponential factors can be calculated. In Table XVII we have arbitrarily chosen A_B = 1.0 for LaB₆(100).

TABLE XVII
RELATIVE VALUES OF PRE-EXPONENTIAL TERMS IN EQ. 5

	A _R	A _B
LaB ₆ (100)	7.8 · 10 ⁻⁷	1.0
CeB ₆ (100)	3.4 · 10 ⁻⁷	3.5 · 10 ⁻⁷
PrB ₆ (100)	6.6 · 10 ⁻⁷	1.0 · 10 ⁻⁷

The data of Table XVII show dramatic differences in relative pre-exponential factors for $\text{LaB}_6(100)$, $\text{CeB}_6(100)$ and $\text{PrB}_6(100)$. It is possible that this effect may be explained by differences in f-shell filling (La has no f electrons, Ce has 2 and Pr has 3).

The effect of stoichiometry upon the vaporization energy has not yet been considered in this discussion. We have studied this phenomenon by comparison of vaporization energies of LaB_6 samples of slightly varying stoichiometries. Table XVIII is a summary of vaporization energies measured on various LaB_6 samples.

TABLE XVIII
VAPORIZATION DATA FOR LaB_6 SAMPLES
(VARIATION WITH STOICHIOMETRY)

Stoichiometry	Crystal Face							
	(100)		(110)		(346)		(211)	
	E_B^*	E_{La}	E_B	E_{La}	E_B	E_{La}	E_B	E_{La}
$\text{LaB}_{5.74}$	7.3	4.4	6.4	4.4	-	-	-	-
$\text{LaB}_{5.86}$	-	-	5.8	5.3	6.3	5.4	-	-
$\text{LaB}_{6.09}$	7.3	5.7	-	-	-	-	6.0	4.4

* Binding energies in eV

Table XVIII shows, for the (100), (110) and (346) planes, an apparent correlation between stoichiometry and La vaporization energy. The correlation does not seem to hold for the (211) surface, however. A possible explanation may be that the correlation holds true only for a given plane, and that the (100) and (110) plane E_{La} values are similar by coincidence. The (346) surface, which readily facets, presumably producing stable (100) faces, may be expected to behave like a macroscopic (100) plane. The (211) surface, on the other hand, is relatively resistant to faceting and should not necessarily have an E_{La} value like the (100). Support of this explanation could come from vaporization studies of (211) faces of crystals of varying stoichiometry. Such studies were not made during this project, because of the poor overall

performance (high volatility, low electron emission) of the $\text{LaB}_6(211)$ crystal examined.

(d) Retarding Work Functions

Figure 35 shows typical FERP $I(V)$ characteristics for various LaB_6 crystal faces and compares with the theoretical characteristics if all electrons were collected. For purposes of clarity the ideal $I(V)$ curve is given only once instead of shifting the curve horizontally to match with each threshold voltage. Figure 36 compares similar data for various RB_6 crystal surfaces. The crystallographic dependent deviation of the experimental $I(V)$ characteristics from the theoretical curve is due to the energy dependent reflection coefficient R_e . The significance of the structure in the retarding $I(V)$ characteristics has been discussed elsewhere.²⁴

The primary interest in FERP measurements is the value of the collector work function which can be obtained directly from the derivative of the $I(V)$ curve at threshold as shown in Figure 37 for the various crystals. A simple relation exists between the peak of the dI/dV curves and the collector work function.²⁴ However, in the rare instance of a sharply varying reflection coefficient at threshold the latter relationship cannot be as well defined. This problem happens to occur for the $\text{LaB}_6(111)$ results shown in Figure 37 where the slope of the normally steep leading edge of the dI/dV curve is greatly reduced and the peak shifted to the right because of a very rapid change in R_e with primary beam energy near the top of the work function barrier.

Table XIX summarizes the values of the FERP work functions ϕ_f obtained for all the RB_6 samples studied here. With the exception of the (346) and (321) planes, the values of ϕ_f are in reasonable agreement with the thermionic ϕ_e values (Table XI). This agreement is partly fortuitous, since a range of ϕ_e values can be obtained in some cases due to its temperature dependence. However, the good agreement between the high temperature ϕ_e and room temperature ϕ_f values is an indication that little variation in the work function occurs between 300 and 1600 K.

A particularly noteworthy result is the consistent difference between the ϕ_e and ϕ_f values for the high index (346) and (321) crystal faces. In each case the retarding work function is substantially larger than the thermionic value.

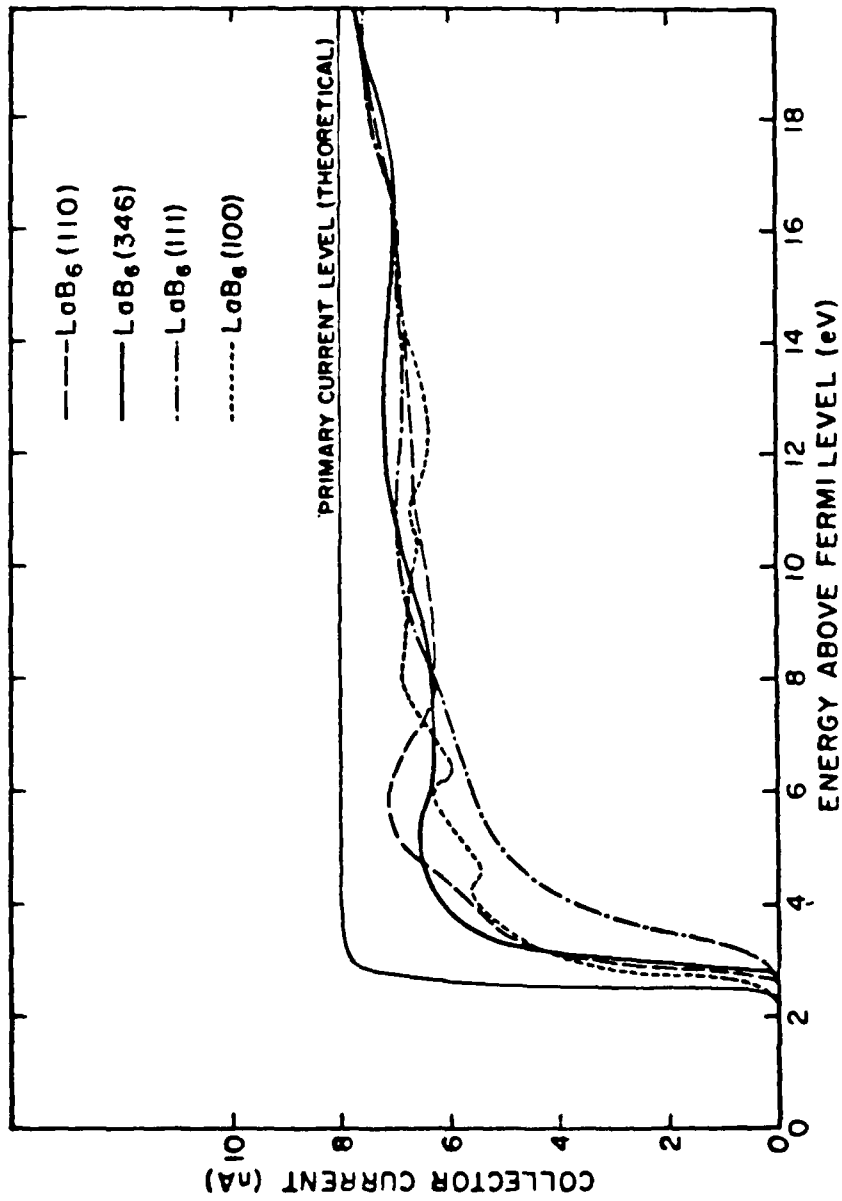


Figure 35. FERP I(V) data for various $\text{LaB}_{6,86}$ crystal faces. The theoretical curve, drawn once for clarity purposes, represents the I(V) curve if all electrons were collected.

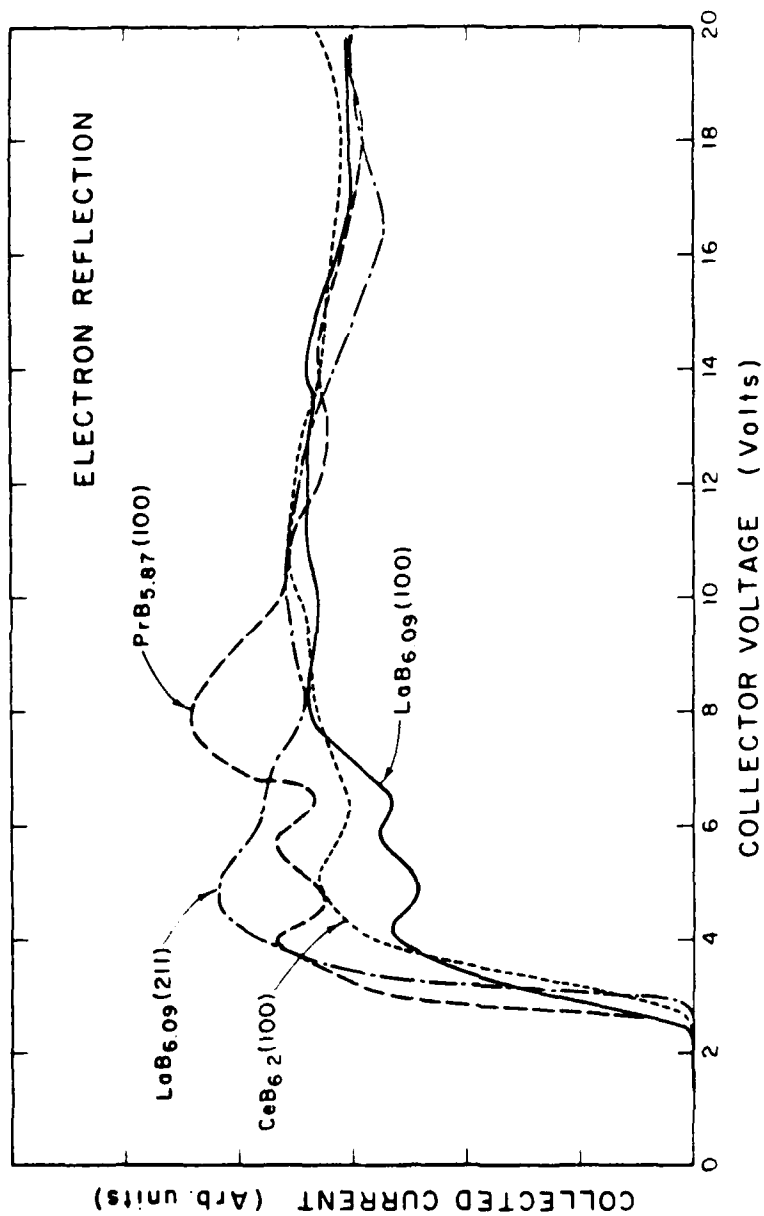


Figure 36. FERP I(V) data for various RB_6 crystal faces.

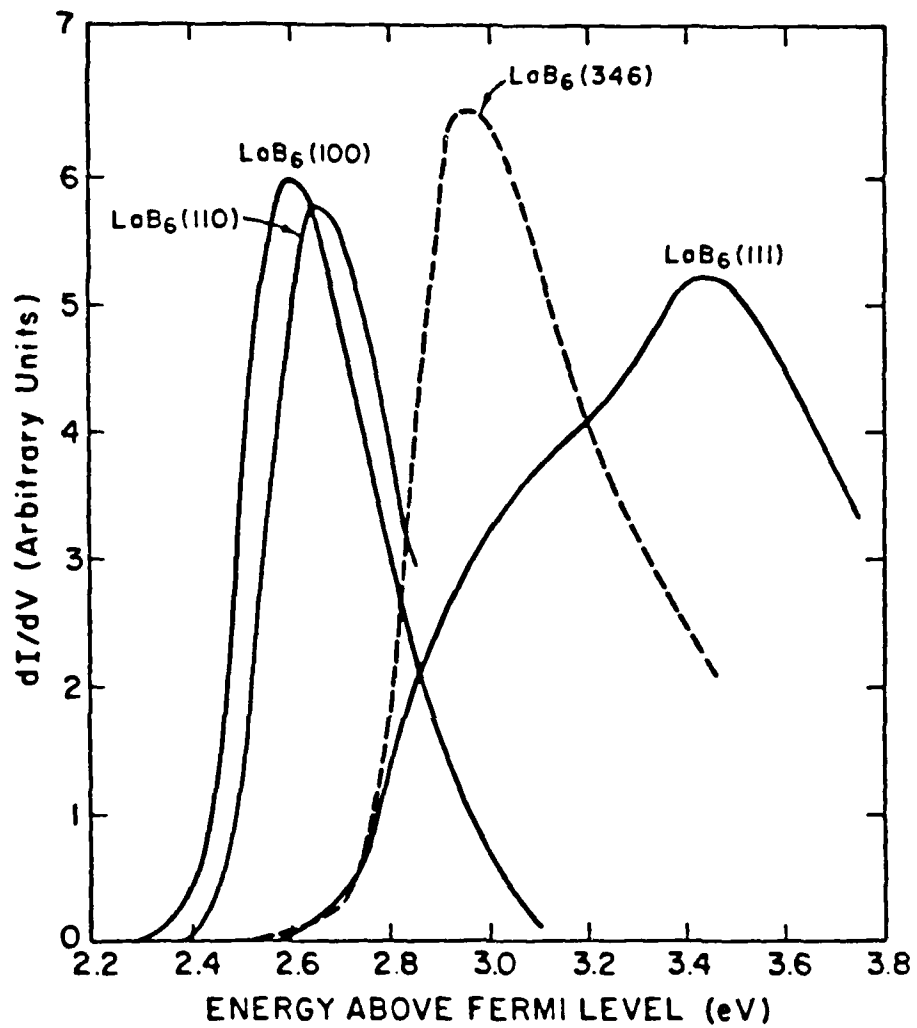


Figure 37. Derivative curves of the Figure 35 curves obtained from FERP analysis of the indicated single crystal planes.

TABLE XIX

FERP WORK FUNCTIONS OF RB_6 SINGLE CRYSTAL SURFACES

Sample	ϕ_{FERP} (eV)
$\text{LaB}_{5.74}(100)$	$2.68 \pm .05$
$\text{LaB}_{5.74}(110)$	$2.84 \pm .05$
$\text{LaB}_{5.74}(321)$	$3.02 \pm .05$
$\text{LaB}_{5.86}(100)$	$2.60 \pm .05$
$\text{LaB}_{5.86}(110)$	$2.65 \pm .05$
$\text{LaB}_{5.86}(111)$	$2.8 \pm .1$
$\text{LaB}_{5.86}(346)$	$2.90 \pm .05$
$\text{LaB}_{6.09}(100)$	$2.57 \pm .05$
$\text{LaB}_{6.09}(211)$	$3.05 \pm .05$
$\text{CeB}_6(100)^*$	$2.73 \pm .05$
$\text{CeB}_6(111)^*$	$3.44 \pm .05$
$\text{CeB}_{6.2}(100)$	$2.75 \pm .05$
$\text{PrB}_{5.87}(100)$	$2.73 \pm .05$

*Precise stoichiometry not determined.

Several interesting observations may be made from the data of Table XIX. In the bulk stoichiometry range below the CVC, we note that for $\text{LaB}_6(100)$, increasing La richness increases the work function slightly. It has also been noted that above the CVC (i.e., $B/\text{La} > 6.03$) the work function increases with increasing B richness.²⁸ Therefore, a minimum work function at or near the CVC was predicted for the $\text{LaB}_6(100)$ surface. The result shown in Table XIX for $\text{LaB}_{6.09}(100)$ may support this prediction. It is also clear from Table XIX that, of the surfaces studied to date, $\text{LaB}_6(100)$ exhibits the lowest FERP work function. The $\text{PrB}_6(100)$ and $\text{CeB}_6(100)$ work functions are approximately equal but higher than that of $\text{LaB}_6(100)$. The effect of stoichiometry on PrB_6 and CeB_6 work functions has not been investigated, so optimum values may be lower than those shown in Table XIX. It is unlikely, however that these compounds, even with optimum stoichiometries, will exhibit work functions lower than LaB_6 .

(e) Theoretical Model of Work Function Behavior

In the quest for developing compounds which exhibit low work functions it would be helpful if some theoretical or empirical model could be developed to determine the important physical parameters necessary to an understanding of the nature of the work function barrier and its variation with crystallographic orientation. In this section we extend the semiempirical model of Steiner and Gyftopoulos²⁹ (S-G), developed for computing the crystallographic dependence of work function of monatomic metals, to RB_6 binary compounds. A theoretical evaluation of the work function can proceed from calculations based on an inhomogeneous-electron-gas model with small pseudopotential corrections to predict orientation effects for simple metals (Li, Na, K, Rb, Cs, Al, Pb, and Mg).³⁰ There are several reasons why this approach cannot be followed for binary compounds of various metals. The theory begins to break down with the noble metals, which have filled d-orbitals near the Fermi level whose interaction is not well described by a small pseudopotential correction. Transition metals are considered outside the framework of this theory. Hence for the case of lanthanum and the other rare earths which have d and/or f orbitals near the Fermi level the theory cannot be applied in its present form. The inhomogeneous-electron-gas

model implies that the lowest work function is associated with the least densely packed face and for high density metals faces have lower surface energies. These conclusions are contrary to what is found for LaB_6 . Thus, another approach has been taken in calculating the work function and its variation with orientation for the binary compound LaB_6 . This is the method of S-G and is based on a semiempirical method that associates the work function with the electronegativity of a localized valence orbital of a surface atom. Successful predictions of the work function dependence on orientation for transition and noble metals have previously been made using this model.

Pauling³¹ defined electronegativity χ as the power of an atom in a molecule to attract electrons. As χ is not a measurable quantity, Mullikan³² proposed defining χ in terms of the ionization potential I and electron affinity A which are observable as

$$\chi = \frac{1}{2} (I + A) \quad (6)$$

The parameters I and A are also functions of the valence state of the atom. Hinze, et al.,³³ further refined the definition of χ in Eq.(6) as the energy per valence electron when the atom (or molecule) is maintained in the neutral state. Gordy³⁴ made the definition more precise by defining the neutral electronegativity χ as the potential energy $\phi(r)$ of a valence electron of an atom in a stable molecule,

$$\chi = \phi(r) = \frac{Z_{\text{eff}} e}{r} \quad (7)$$

where Z_{eff} is the shielded nuclear charge, r is the single bond covalent radius and $\phi(r)$ is the potential energy. With the assumption that each of the core electrons completely screens out unit of nuclear charge and the other valence electrons screen 1/2 of a charge Gordy found

$$\chi = 0.98 \left(\frac{\nu + 1}{r} \right) + 1.57 \text{ (eV)} \quad (8)$$

where ν is the valence of the atom under consideration. Hinze et al.³³ showed it was reasonable to consider

$$\chi = \chi(q) = d E(q)/dq \quad (9)$$

where q is the fractional charge in a molecular orbital and $E(q)$ is the energy of that molecular orbital. This allowed a wider class of molecules to be assigned an electronegativity by providing an analysis which incorporated fractional charge into the model for evaluating χ . Therefore the Gordy Eq.(8) might be applied using nonintegral values for the charge number.

S-G proposed that the process of electron emission be interpreted as originating from a localized valence orbital of a surface atom rather than from the Fermi level of the electron-gas model. The state of the surface atom involved in the emission process is determined by the collective interactions of all the other atoms on the one under consideration. A primary assumption made is that the energy of a surface valence orbital remain constant throughout the emission process. The use of χ in their model otherwise would have no meaning since χ is defined in terms of a neutral molecule. Hence the analysis is essentially restricted to solids that have conduction electrons which can act as a charge supply preventing the surface atom from changing its energy as is the case when an isolated atom is ionized. In this way Gordy's definition of χ is extended to include a valence orbital of a surface atom. Since the work function ϕ is considered to be the amount of energy required to remove an electron from a valence orbital of a surface atom they propose equating it with χ itself, as this is now considered the potential energy of an electron in a valence orbital of a surface atom. Thus Eq.(8) becomes

$$\phi = 0.98 \left(\frac{v_s + 1}{r} \right) + 1.57 \text{ eV} \quad (10)$$

where v_s is defined as the valence of a surface atom (or surface valence).

S-G determined the surface valence in the following manner: Pauling³¹ found empirically that fractional bond numbers n_1 and n_2 associated with interatomic separations R_1 and R_2 are related by

$$R_2 - R_1 = 0.26 \ln(n_1/n_2) \quad (11)$$

The valence of an atom in the interior v_m is related to fractional bond numbers n_1 and n_2 by

$$v_m = M_1 n_1 + M_2 n_2 = n_2 \left[M_2 + M_1 \exp \left(\frac{R_2 - R_1}{0.26} \right) \right] \quad (12)$$

where M_1 and M_2 are the number of nearest and next nearest neighbors respectively. S-G further assumed the fractional bond number is the same for both a bulk and surface atom. Hence given a geometry for the solid and the value of v_m from Eq.(12), the surface valence v_s is found as follows:

$$v_s = N_1 n_1 + N_2 n_2 = n_2 \left[N_2 + N_1 \exp \frac{R_2 - R_1}{0.26} \right] \quad (13)$$

where N_1 and N_2 are the number of nearest and next nearest neighbors of the surface atom. Once v_s is determined, ϕ is found via Eq.(10).

Several assumptions are made in extending this model to a binary compound such as RB_6 . First, the B_6 -octahedral complex is considered as a single entity. Second, no attempt is made at determining a weighted fractional bond number dependent on the difference in the amount of charge between an R-R bond and an R- B_6 bond at the same atomic separation.

Less than 1% of the charge is calculated as being involved in bonding with R atoms further than next nearest neighbors hence these are not included in the calculations.³⁵ The S-G analysis of the work function is applied with respect to the valence orbitals of the surface R atoms only. The bulk valence v_m of R is assumed equal to two based on band structure calculations³⁵ and an ESCA study³⁶ indicating two electrons from the lanthanum atom are involved in bonding with the boron octahedra for LaB_6 .

Table XX gives a listing of the number of nearest neighbors (B_6 -octahedra) and the next nearest neighbors (R-atoms) for a surface R atom as a function of orientation.

At this point independent data must be used to decide which configuration (R or B_6 outermost) is most probable. Experiments using angular resolved XPS and LEED³⁷ indicate the $LaB_6(100)$ surface is terminated by lanthanum atoms, while the $LaB_6(111)$ surface has been observed to terminate with the boron atoms.²⁶ Thus, of the major crystal faces only the (111) surface is assumed to have a configuration with the boron octahedra outermost.

TABLE XX

VALUES OF N_1 AND N_2 FOR EQ.(13) BASED ON RB_6

Orientation	(100)	(110)	(111)
nearest # neighbors, N_1	4 (8)	6	4 (7)
next nearest # neighbors, N_2	5 (5)	4	3 (4)

Numbers in () indicate the case in which the B_6 -octahedra terminate the surface.

Table XXI compares the results of Eq.(10) for predicting the work function and its variation with orientation along with experimental data. The prediction of the order of increasing work function as

$$\phi(100) < \phi(110) < \phi(111)$$

is consistent with the experimental data. The higher index planes are more complex, especially if faceting occurs, and have not been analyzed according to the theory. Another attempt³⁸ at using the S-G model resulted in a different ordering and lower absolute values. There are several reasons for this. First, a bulk valence of one was used, overemphasizing the importance of La-La bonding. Second, the radius of the lanthanum-atom was taken as half the lattice constant of LaB_6 rather than the metallic radius of lanthanum. Finally it is unclear whether consideration was taken of the possibility of terminating the (100) and (111) surfaces with boron as opposed to lanthanum.

TABLE XXI

WORK FUNCTION OF LaB₆

Orientation	Theory		Experimental	
	Present Study	Berrada et al. ³⁸	Thermionic LaB _{5.85} /LaB _{5.74}	Retarding Potential LaB _{5.85} /LaB _{5.74}
100	2.65	2.43	2.52	2.60
110	2.87	2.36	2.62	2.65
111	3.00	2.27	2.90	2.90

A La-metal atom radius or $r = 1.87 \text{ \AA}$ used.³⁹

B atom assumed outermost

26
UPS

The rare earths have isostructural RB_6 compounds. This model may lend further insight into their emission properties. A deviation in the predicted order of the work function with orientation for the other RB_6 compounds would indicate that other planes besides the (111) have a reduced concentration of metal atoms terminating the surface. This could be used as a guide to distinguish anomalous orientation-dependent evaporation and/or diffusion phenomena.

Table XXII illustrates the range of work function values for $RB_6(100)$ surfaces predicted by the model for a (100) plane terminated by either R or B atoms. There are two possible explanations for the low values predicted for EuB_6 and SmB_6 . The first is that both those compounds terminate with a low concentration of surface R atoms, as has been observed for SmB_6 .⁴⁰ Assuming the concentration of surface metal atoms in RB_6 compounds is proportional to the heat of sublimation of the metal itself it is reasonable to expect an even lower concentration of Eu-atoms on the surface of EuB_6 than Sm-atoms on SmB_6 . The second possibility is that the assumption that mobile conduction electrons exist in EuB_6 and SmB_6 is erroneous since EuB_6 is known to be divalent. A similar case is divalent BaB_6 where the work function value for the (100) surface terminated by boron is calculated to be 2.92 eV, whereas the experimental value of 3.4 eV¹⁶ is considerably higher.

Table XXII shows that the experimentally measured increase in work function with increasing atomic number of R is also predicted by the S-C model except for EuB_6 . The range of predicted work functions assuming all $RB_6(100)$ compounds terminate with the R-atom is smaller than that which was measured. This may imply that the actual concentration of R-atoms terminating the surface is more important in determining the work function than geometrical variations due to a variation in the lattice constant or the metal atom ratio. This conclusion agrees with a thermodynamic investigation which found that the surface composition is a major factor in determining the emission properties of LaB_6 .²⁸

TABLE XXII

COMPARISON OF CALCULATED AND MEASURED WORK FUNCTIONS

RB ₆ (100)	Predicted Work Function ϕ (eV)		Experimentally Determined ϕ			
	Terminated by: R-atoms	B-atoms	Ref. 41	Ref. 38	Ref. 16	This Study
LaB ₆	2.65	3.13	2.86	2.74	2.70	2.57
CeB ₆	2.68	3.17	3.02	3.03	2.62	2.75
PrB ₆	2.68	3.18	3.16			2.73
NdB ₆	2.68	3.18	3.19	3.10		
SmB ₆	2.69	3.19	4.24		3.92	
EuB ₆	2.59	3.04	4.32			

C. Discussion and Conclusions

The results of this study support and expand our earlier understanding of the nature of RB_6 surfaces, and allow us to evaluate the utility of various RB_6 compounds in thermionic cathode applications. Primary criteria for these applications are low surface work function and high thermal stability, corresponding to high emitted electron current density and low evaporation at operating temperature.

Several materials parameters have been shown to affect emission and vaporization strongly. These parameters include crystal surface orientation, bulk and surface stoichiometry, and the type of rare earth element in the RB_6 compound. Each of these variables will be discussed separately.

1. Effect of Rare Earth Compound

Table XXIII is a summary of thermionic (ϕ_e) and retarding potential (V_f) work function data for (100) faces of various RB_6 compounds (plus BaB_6) determined in this study and in an earlier study.¹⁶ The data have been chosen to minimize the effect of varying stoichiometry ($B/R \approx 6.0$ in every case) so that the effect of the compound itself may be highlighted. The superiority of LaB_6 and CeB_6 over the other compounds is evident, all other factors being equal.

The comparison of Table XXIII does not take into consideration the thermal stability of the various compounds. However, the most important figure of merit for a cathode is not the work function or emitted current density alone, but rather the ratio of electron emission to material vaporization rate. Thus, emission and vaporization data of Tables XI, XVI and XVII for (100) faces of LaB_6 , CeB_6 and PrB_6 are recast in the form of ratios, as shown in Table XXIV. (Comparable vaporization data for BaB_6 and SmB_6 are unavailable.) Eqs.(2) and (5) have been used to allow comparison of emission and vaporization at the same temperature. The result of the figure of merit calculation is a two-to-one superiority of $LaB_{6.09}(100)$ over $CeB_{6.2}(100)$ and a four-to-one superiority of $LaB_{6.09}(100)$ over $PrB_{5.87}(100)$.

2. Effect of Bulk Stoichiometry

The effect of bulk stoichiometry upon work function of a given RB_6 single crystal face has been studied systematically in greatest detail for $LaB_6(100)$. Table XXV shows the relevant data, covering a bulk stoichiometry

TABLE XXIII
 WORK FUNCTION SUMMARY FOR (100) FACES

	ϕ_e (1600 K) (eV)	ϕ_f (300 K) (eV)
BaB _{6.0} *	3.40 ± .05	3.40 ± .05
LaB _{6.09}	2.69 ± .05	2.57 ± .05
CeB _{6.0} *	2.62 ± .05	2.50 ± .05
PrB _{5.87}	2.74 ± .05	2.73 ± .05
SmB _{6.0} *	3.92 ± .05	4.30 ± .05

* Molten Al flux grown. Data from Ref. 16.

TABLE XXIV
 FIGURE OF MERIT OF (100) FACES OF RB₆ COMPOUNDS

	Emitted Current Density J(A/cm ²) @ 1600 K	Relative J/R _m * @ 1600 K
LaB _{6.09}	1.02	1.00
CeB _{6.2}	0.42	.52
PrB _{5.87}	0.71	.24

* R_m = relative total mass loss rate

J/R_m = figure of merit

range of $5.74 \leq B/La \leq 6.09$. At 1600 K, a clear minimum in ϕ_e is evident around $B/La = 5.86$, while the minimum (if it exists) appears shifted toward the higher B/La bulk ratios at 300 K, based upon retarding potential ϕ_f data. As has been demonstrated previously (Table XIV), the surface stoichiometry of a given crystal face changes slightly with temperature, so a shift in the minimum work function with temperature should be expected. Thus, the ϕ_e and ϕ_f data of Table XXV are not necessarily inconsistent.

TABLE XXV
LaB₆(100) WORK FUNCTION SUMMARY

B/La	ϕ_e (1600 K) (eV)	ϕ_f (300 K) (eV)
5.74	$2.71 \pm .05$	$2.68 \pm .05$
5.86	$2.52 \pm .05$	$2.60 \pm .05$
6.0*	$2.70 \pm .05$	$2.60 \pm .05$
6.09	$2.69 \pm .05$	$2.57 \pm .05$

* Molten Al flux grown. Data from Ref. 16.

We may again recast the data in terms of relative figures of merit. We make one assumption, that the pre-exponential factor in Eq.(5) is constant for all the LaB₆ crystal faces studied. Then

$$\frac{J}{R_m} = \frac{A_R T^2 e^{-\phi_e/kT}}{\left(M_{La} A_{La} e^{-E_{La}/kT} + M_B A_B e^{-E_B/kT} \right)} \quad (14)$$

where J = current density, R_m = mass loss rate, A_R = Richardson's constant = $120 \text{ A}/(\text{cm}^2 - \text{K}^2)$, M_{La} and M_B are the masses of La and B atoms, respectively, and the A's and E's are the corresponding pre-exponential factors and activation energies for La and B vaporization. In practice, we find that the B

rate and the B mass are each approximately ten times smaller than the corresponding La values. Thus, the B contribution is of the order of 1% of the total and can be neglected, yielding

$$\frac{J}{R_m} = \frac{A_R T^2}{M_{La} A_{La}} e^{\frac{(E_{La} - \phi_e)}{kT}} \quad (15)$$

For constant temperature, the pre-exponential factor is constant and may be neglected since we intend to normalize the resulting figures of merit to 1.0 for the best case. Table XXVI summarizes the LaB₆ data expressed in this fashion, with the results normalized so the highest figure of merit is 1.0.

The clear superiority of near-CVC composition is apparent in Table XXVI. Consider, for example, the (100) planes of the three different bulk compositions. Primarily because of the large change in La vaporization energy from B/La = 5.74 to B/La = 6.09 (an increase of nearly 2.5 eV) the figure of merit improves by a factor of about 14000. Even the intermediate B/La = 5.86 composition, which shows a significantly lower work function, has a figure of merit five times poorer than the B/La = 6.09 composition due to the dramatic variation in vaporization rate with stoichiometry.

The LaB_{6.09} single crystal samples were prepared from zone refined rod made with LaB_{6.2} starting material. The LaB_{5.74} and LaB_{5.86} samples were cut from rods zone refined from approximately LaB_{6.0} material. Thus, it appears relatively simple to control crystal stoichiometry over the range of interest, that is, the composition range yielding maximum figure of merit.

TABLE XXVI
RELATIVE FIGURES OF MERIT* OF LaB₆ SURFACES AT 1600 K

<u>Bulk B/La</u>	<u>Crystal Face</u>	<u>Figure of Merit (Normalized)</u>
5.74	(100)	6.9×10^{-5}
	(110)	5.2×10^{-5}
5.86	(100) [†]	0.19
	(110)	7.9×10^{-2}
	(111) [†]	2.5×10^{-2}
	(346)	0.87
6.09	(100)	1.00
	(211)	1.5×10^{-5}

* Ratio of electron current density to total mass loss rate, assuming pre-exponential term in vaporization equation is the same for all crystal faces.

[†] E_{La} assumed the same as (110) face.

3. Effect of Crystal Face

The effect of crystal face upon volatility seems to be much weaker than the effect of stoichiometry (see Table XVIII). However, the work function does vary considerably from face to face, for fixed bulk stoichiometry, as was previously summarized in Tables XI and XIX for effective thermionic and retarding potential work functions, respectively.

From these results we may conclude that the (100) face generally has the lowest work function of the faces studied, for a given bulk stoichiometry, but there are exceptions. The $\text{LaB}_{5.86}$ (346) surface, for example, gave the lowest ϕ_e (2.41 eV) that we have observed, but LEED results indicate that this face facets to planes of higher symmetry during heating. FERP measurements at room temperature showed a high retarding potential work function for this face. It appears to be generally true that high index planes exhibit higher work function and less stability, either through faceting or mass loss, than do the low index planes. Of the low index (100), (110) and (111) planes, the (100) is clearly the best for thermionic emission applications. The obvious geometric differences between these faces suggest why this should be so, as has already been discussed in detail under Task IV, section (3).

4. Surface Stoichiometry

Surface stoichiometry is not an independent parameter, since it is a function of both bulk stoichiometry and crystal face. However, surface stoichiometry also depends upon surface treatment and its variation with such treatment is easily measured by AES. In Table XXVII, the effects of sputtering and heating a surface are compared with stoichiometry measurements on an in situ cleaved $\text{LaB}_{6.09}$ (100) surface.

Since the peak intensities of the various Auger transitions differ, the ratios have been arbitrarily normalized to the independently measured bulk stoichiometry value ($B/La = 6.09$) for the cleaved surface. The ratio of the two La peaks has been normalized to 1.0 for the fractured surface. Thus, the ratios given in Table XXVII represent the actual "surface" stoichiometry, bearing in mind, however, that the Auger electrons have differing escape depths and thus probe different numbers of surface layers. This difference in escape depths accounts, for example, for the change in

La(NOO)/La(MNN) with surface treatment, and also explains why the B(KLL)/La(NOO) and B(KLL)/La(MNN) columns are not the same.

TABLE XXVII

NORMALIZED AUGER PEAK HEIGHT RATIOS FOR IN SITU FRACTURED,

Ar⁺ SPUTTERED AND HEATED LaB_{6.09}(100) SURFACES

PRIMARY BEAM ENERGY, 5.0 keV

T = 300 K

	$\frac{B(KLL)}{La(NOO)}$	$\frac{B(KLL)^*}{La(MNN)}$	$\frac{La(NOO)^{**}}{La(MNN)}$
In Situ Fractured	6.09	6.09	1.0
Ar ⁺ Sputtered (~ 100 Å removed)	2.3	2.8	1.2
Annealed (1700 K) LaB _{6.09} (100)	1.8	5.2	2.9

[†]B(KLL) = 179 eV; La(NOO) = 78 eV; La(MNN) = 625 eV

* Normalized to 6.09 for fractured surface

** Normalized to unity for fractured surface

5. Future Work

The results we have obtained for LaB₆, CeB₆ and PrB₆ single crystals suggest that at least LaB₆(100) and CeB₆(100) should be studied further. In particular, the effect of stoichiometry should be investigated in greater detail, since it so strongly affects the volatility and, thus, the figure of merit. In addition, the (210) faces of these materials should be examined. Finally, the second phase material should be investigated.

There is evidence to suggest good thermal stability and very low work function for this compound, properties desirable in cathode materials.

Even with the present understanding, however, these materials are very promising. Using data of Storms and Mueller¹⁹ to obtain an approximate absolute LaB_6 mass loss rate, we have compared the figure of merit of $\text{LaB}_{6.09}(100)$ with that for an M-type dispenser cathode, using available work function⁴² and mass loss⁴³ data. The result of this comparison is that, at 3 A/cm^2 , $\text{LaB}_{6.09}(100)$ comes within a factor of 2 of the best M-type cathode performance. When the essentially unlimited lifetime of the LaB_6 cathode is considered (in practice consisting only of dimensional changes with fixed emission properties), and account is taken of the possibility of long term LaB_6 operation at $10\text{-}30 \text{ A/cm}^2$ where dispenser cathode lifetimes are very short, then the $\text{LaB}_{6.09}(100)$ cathode appears to be extremely competitive. In the future we may well see LaB_6 (or CeB_6) cathodes performing as reliably in high current density, large area applications as LaB_6 cathodes do today in small spot size, high brightness applications.

References

1. M. Futamoto, T. Aida and U. Kawabe, *Jap. J. Appl. Phys.* 14 (1975) 1263.
2. T. Tanaka, E. Bannai and S. Kawai, *J. Cryst. Growth* 30 (1975) 193.
3. T. Takagi and M. Ishii, *J. Cryst. Growth* 40 (1977) 1.
4. J. Verhoeven, E. D. Gibson, M. A. Noack and R. J. Conzemius, *J. Cryst. Growth* 36 (1976) 115.
5. S. Motojima, Y. Takahashi and K. Sugiyama, *J. Cryst. Growth* 44 (1978) 106.
6. I. Zubeck, R. Feigelson, R. Huggins and P. Petitt, *J. Cryst. Growth* 34 (1976) 85.
7. *Treatise on Analytical Chemistry*, Ed. I. M. Kolthoff and P. J. Elving, Part II, Vol. 20, p 55. J. Wiley & Sons, N.Y. 1978.
8. *Determination of Boron Nitride and Other Borides*, J. W. Tereshko, *Anal. Chem.* 35 (1963) 157.
9. *Chelometric Titrations of Metal Ions with Potentiometric End Point Detection*, C. N. Reilleg, R. W. Schmid and D. W. Lamson, *Anal. Chem.* 30 (1958) 953.
10. *Complexometric Titrations*, G. Schwarzenbach and H. Flashka, translated by HMNH Irving, p. 194, Methuen & Co., London 1969.
11. *Chelometric Titrations Using an Azoarsenic Acid Indicator*, J. S. Frik, R. T. Oliver and D. J. Pietrzyk, *Anal. Chem.* 30 (1958) 1111.
12. K. Takagi and M. Ishii, *J. Cryst. Growth* 40 (1977) 1.
13. K. E. Spear in Phase Diagrams. Materials Science and Technology IV, A. M. Alper, ed. (Academic Press, New York, 1976).
14. P. R. Davis and S. A. Chambers, *Appl. Surf. Sci.* 8 (1981), in press.
15. M. A. Noack and J. D. Verhoeven, *J. Cryst. Growth* 49 (1980) 595.
16. L. Swanson and D. McNeely, *Surf. Sci.* 83 (1979) 11.
17. S. F. Vogel, *Rev. Sci. Inst.* 41 (1970) 585.
18. E. K. Storms, *J. Appl. Phys.* 50 (1979) 4450.
19. E. Storms and B. Mueller, *J. Phys. Chem.* 82 (1978) 51.
20. C. Oshima, E. Bannai, T. Tanaka and S. Kawai, *J. Appl. Phys.* 48 (1977) 3925.
21. C. Oshima, M. Aono, T. Tanaka, R. Nishitani and S. Kawai, *J. Appl. Phys.* 51 (1980) 997.

22. M. Futamoto, S. Hosoki, H. Okano and U. Kawabe, *J. Appl. Phys.* 48 (1977) 3541.
23. T. Sakurai, G. Robertson and Y. Kuk, *Proc. of the Electrochemical Society* 80-1 (1980) 608.
24. R. Strayer, W. Mackie and L. Swanson, *Surf. Sci.* 34 (1973) 225.
25. E. B. Bas, P. Hafner and S. Klauser, *Proc. Intern. Vac. Congress and 3rd Intern. Conf. Solid Surfaces* (Edited by Dobrozemsky, Rüdener, Vlehböck and Breth), Vienna, 1977, p. 881.
26. R. Nishitani, M. Aono, T. Tanaka, C. Oshima, S. Kawai, H. Iwasaki and S. Nakamura, *Surf. Sci.* 93 (1980) 535.
27. E. D. Cater, *J. Chem. Educ.* 55 (1978) 697.
28. E. Storms and B. Mueller, *J. Appl. Phys.* 50 (1979) 3691.
29. D. Steiner, E. Gyftopoulos, *Proc. of the 7th Annual Conf. on Physical Electronics*, MIT, Cambridge, Mass. 1967, unpublished.
30. N. Lang, W. Kohn, *Phys. Rev. B* 3 (1971) 1215.
31. L. Pauling, *The Nature of the Chemical Bond*, Cornell University Press, Ithaca, NY, pp. 393-448 (1939).
32. R. Mullikan, *J. Chem. Phys.* 2 (1934) 782.
33. J. Hinze, M. Whithead, and H. Jaffé, *J. Am. Chem. Soc.* 85 (1963) 148.
34. W. Gordy, *Phys. Rev.* 69 (1946) 604.
35. A. Hasegawa and A. Yanase, *J. Phys. F: Metal Phys.* 7 (1977) 1245.
36. M. Aono, S. Kawai, S. Kono, M. Okusawa, T. Sagawa, Y. Takehana, *J. Phys. Chem. Solids* 37 (1976) 215.
37. M. Aono, C. Oshima, T. Tanaka, E. Bannai, S. Kawai, *J. Appl. Phys.* 49 (1978) 2761.
38. A. Berrada, J. Mercurio, J. Etourneau, P. Hagenmuller, *J. Less Common Metals* 59 (1978) 7.
39. S. Dickinson, *Ionic, Covalent, and Metallic Radii of the Chemical Elements*, Distributed by the National Technical Information Service AD 722 436, 1 December 1970.
40. M. Aono, R. Nishitani, C. Oshima, T. Tanaka, E. Bannai, S. Kawai, *Surf. Sci.* 86 (1979) 631.
41. M. Futamoto, M. Nakazawa and U. Kawabe, *Surf. Sci.* 100 (1980) 470.

42. D. Jones, D. McNeely and L. W. Swanson, Appl. Surf. Sci. 2 (1979) 232.
43. R. A. Tuck, Appl. Surf. Sci. 2 (1979) 128.



MISSION
of
Rome Air Development Center

RADC plans and executes research, development, test and selected acquisition programs in support of Command, Control Communications and Intelligence (C³I) activities. Technical and engineering support within areas of technical competence is provided to ESD Program Offices (POs) and other ESD elements. The principal technical mission areas are communications, electromagnetic guidance and control, surveillance of ground and aerospace objects, intelligence data collection and handling, information system technology, ionospheric propagation, solid state sciences, microwave physics and electronic reliability, maintainability and compatibility.

Printed by
United States Air Force
Hanscom AFB, Mass. 01731

LMED

-8